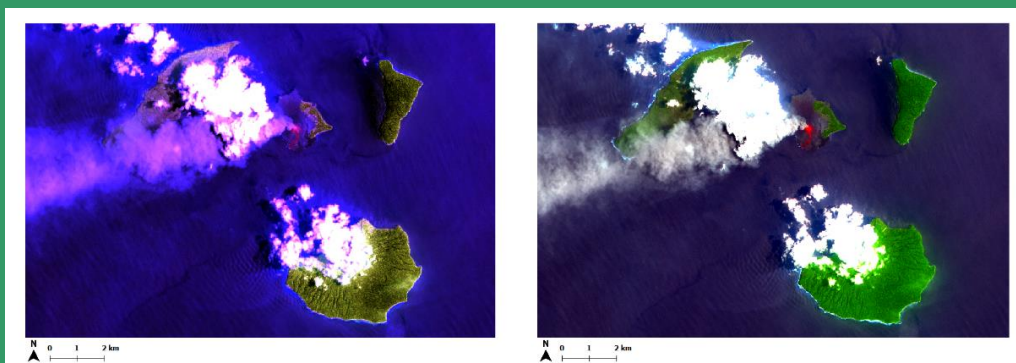
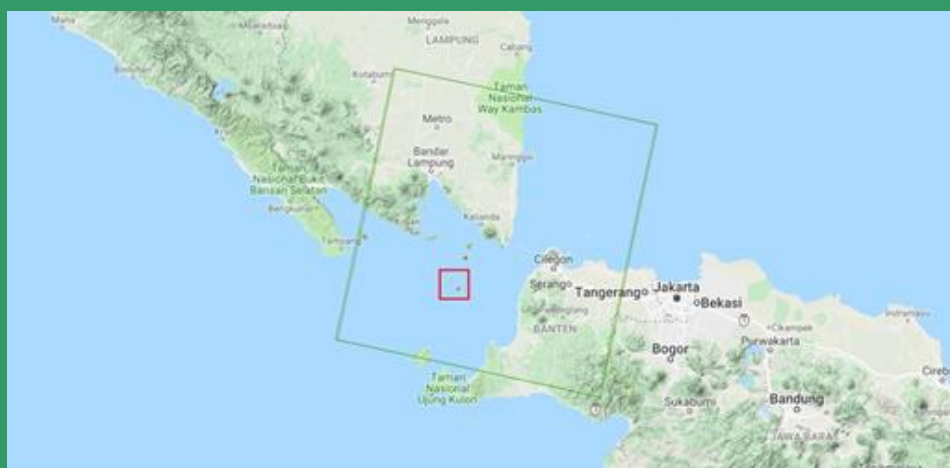




# International Journal of Remote Sensing and Earth Sciences



Vol. 15 No. 2 December 2018

P-ISSN 0216-6739; E-ISSN 2549-516X  
Accreditation No. 30/E/KPT/2018

International Journal of  
Remote  
Sensing and  
Earth Sciences

Published by  
Indonesian National Institute of Aeronautics and Space  
(LAPAN)

## Editorial Committee Preface

Dear IJReSES Readers,

There is no special day except today. Today, we deliver this journal volume to you all readers. We are sorry for a bit late on publishing this volume due to a very tight discussion on selection, review, and accept the papers. In total, we received 23 papers for publication. Four papers were rejected, 9 papers are accepted and published, and 10 papers are under review for the next publication.

From 9 papers published in this volume, we can divide into two categories of research. The first is remote sensing technology research. Those are Analysis of Antenna Specification for Very High Resolution Satellite Data Acquisition through Direct Receiving System (DRS) and Geometric Aspects Evaluation of GNSS Control Network for Deformation Monitoring in the Jatigede Dam Region. The second is the remote sensing application. Those are Accuracy Evaluation of Structure From Motion Thermal Mosaicing in The Center of Tokyo, Observing The Inundated Area Using Landsat-8 Multitemporal Images and Determination Of Flood-Prone Area in Bandung Basin, Mangrove Forest Change in Nusa Penida Marine Protected Area, Bali - Indonesia using Landsat Satellite Imagery, Detecting The Lava Flow Deposits From 2018 Anak Krakatau Eruption using Data Fusion Landsat-8 Optic And Sentinel-1 SAR, Preliminary Study of Horizontal and Vertical Wind Profile Of Quasi-Linear Convective Utilizing Weather Radar Over Western Java Region, Indonesia, Preliminary Detection of Geothermal Manifestation Potential using Microwave Satellite Remote Sensing, and The Utilization of Remote Sensing Data To Support Green Open Space Mapping In Jakarta, Indonesia.

Finally, enjoy your reading of the IJRESES Vol. 15 No. 2 December 2018, and please refer this journal content for your next research and publication. For editorial team members and the journal secretariat, thank you very much for all big supports for this volume publication.

Editor-in-Chief,

**Dr M. Rokhis Khomarudin**

**Editorial Committee Members**  
**INTERNATIONAL JOURNAL OF**  
**REMOTE SENSING AND EARTH SCIENCES**  
**Vol. 15 No. 2 December 2018**  
**P-ISSN 0216-6739; E-ISSN 2549-516X**

Director : **Dr. Orbita Roswintiarti, M.Sc.**  
Editor-in-Chief : **Dr. M. Rokhis Khomarudin**  
Co Editor-in-Chief : **Inggit Lolita Sari, S.T., M.GIS**  
Peer Reviewers : **Prof. Dr. Ir. I Nengah Surati Jaya, M.Agr.**  
**Prof. Dr. Ir. Dewayany Sutrisno, M.AppSc.**  
**Dr. Ir. Katmoko Sambodo, M.Eng.**  
**Dr. Takahiro Osawa**  
**Dr. Ing. Widodo Setyo Pranowo**  
**Dr. Baba Barus**  
**Dr. Indah Prasasti**  
**Ir. Suhermanto M.T.**  
Secretariat : **Mr. Jasyanto**  
**Mr. Suwarsono**  
**Ms. Sayidah Sulma**  
**Mr. Zylshal**  
**Mr. Dwi Haryanto**  
**Mr. Aulia Pradipta**

Contribution Paper to:

**IJReSES Secretariat**  
**Indonesian National Institute of Aeronautics and Space (LAPAN)**  
Jl. Kalisari No. 8, Pekayon, Pasar Rebo, Jakarta 13710, INDONESIA  
Telp. (021) 8710065, Fax. (021) 8722733  
[www.jurnal.lapan.go.id](http://www.jurnal.lapan.go.id)



Published by:  
**Indonesian National Institute of Aeronautics and Space**  
**(LAPAN)**



**INTERNATIONAL JOURNAL OF  
REMOTE SENSING AND EARTH SCIENCES  
Vol. 15 No. 2 December 2018  
P-ISSN 0216-6739; E- ISSN 2549-516X  
Accreditation No. 30/E/KPT/2018**

**Contents**

Editorial Committee Preface .....	ii
Editorial Committee Members .....	iii
<b>ACCURACY EVALUATION OF STRUCTURE FROM MOTION THERMAL MOSAICING IN THE CENTER OF TOKYO</b>	
Atik Nurwanda, Tsuyoshi Honjo, Nobumitsu Tsunematsu, Hitoshi Yokoyama.....	103
<b>ANALYSIS OF ANTENNA SPECIFICATION FOR VERY HIGH RESOLUTION SATELLITE DATA ACQUISITION THROUGH DIRECT RECEIVING SYSTEM (DRS)</b>	
Muchammad Soleh, Ali Syahputra Nasution, Arif Hidayat, Hidayat Gunawan, Ayom Widipaminto.....	113
<b>OBSERVING THE INUNDATED AREA USING LANDSAT-8 MULTITEMPORAL IMAGES AND DETERMINATION OF FLOOD-PRONE AREA IN BANDUNG BASIN</b>	
Fajar Yulianto, Suwarsono, Sayidah Sulma, Muhammad Rokhis Khomarudin .....	131
<b>MANGROVE FOREST CHANGE IN NUSA PENIDA MARINE PROTECTED AREA, BALI - INDONESIA USING LANDSAT SATELLITE IMAGERY</b>	
August Daulat, Widodo Setiyo Pranowo, Syahrial Nur Amri .....	141
<b>DETECTING THE LAVA FLOW DEPOSITS FROM 2018 ANAK KRAKATAU ERUPTION USING DATA FUSION LANDSAT-8 OPTIC AND SENTINEL-1 SAR</b>	
Suwarsono, Indah Prasasti, Jalu Tejo Nugroho, Jansen Sitorus, Djoko Triyono .....	157
<b>GEOMETRIC ASPECTS EVALUATION OF GNSS CONTROL NETWORK FOR DEFORMATION MONITORING IN THE JATIGEDE DAM REGION</b>	
Made Ditha Ary Sanjaya, T. Aris Sunantyo, Nurrohmat Widjajanti .....	167
<b>PRELIMINARY STUDY OF HORIZONTAL AND VERTICAL WIND PROFILE OF QUASI- LINEAR CONVECTIVE UTILIZING WEATHER RADAR OVER WESTERN JAVA REGION, INDONESIA</b>	
Abdullah Ali, Riris Adrianto, Miming Saepudin .....	177
<b>PRELIMINARY DETECTION OF GEOTHERMAL MANIFESTATION POTENTIAL USING MICROWAVE SATELLITE REMOTE SENSING</b>	
Atriyon Julzarika, Udhi Catur Nugroho .....	187
<b>THE UTILIZATION OF REMOTE SENSING DATA TO SUPPORT GREEN OPEN SPACE MAPPING IN JAKARTA, INDONESIA</b>	
Hana Listi Fitriana, Sayidah Sulma, Nur Febrianti, Jalu Tejo Nugroho, Nanik Suryo Haryani ..	199
Instruction for Authors .....	
Index.....	

Published by:

**Indonesian National Institute of Aeronautics and Space (LAPAN)**

**International Journal of  
Remote Sensing and Earth Sciences**

P-ISSN 0216 – 6739; E- ISSN 2549-516X  
Accreditation No. 30/E/KPT/2018

Vol. 15 No. 1 June 2018

The abstract may be copied without permission or charge

ABSTRACT

**MAPPING APATITE-ILMENITE RARE EARTH ELEMENT MINERALIZED ZONE USING FUZZY LOGIC METHOD IN SIJUK DISTRICT, BELITUNG/ Muhamad Iqbal Januadi Putra, Sobirin IJRESES, 15 (1) 2018 : 1-14**

District of Sijuk located in Belitung Island is rich with non-lead mineral content. As the part of Southeast Asia's Lead Belt, the presence of Apatite-ilmenite Rare Earth Element formed by the region's geological condition is very likely. However, there has not been any activity to map and identify the apatite-ilmenite distribution in this region. Therefore, the objective of this study was to map the mineralized apatite-ilmenite in Sijuk District. Using remote sensing technology, Landsat 8 OLI were utilized to map the distribution of mineralized apatite-ilmenite rare earth element. Alteration mineral carrier, geological structure, and lithology data were all used as variables. Landsat-8 was pre-processed using band ratio and Directed Principal Component Analysis (DPCA) method for gaining alteration variable. The fuzzy logic method was then deployed for integrating all data. The result of this research showed the potential distribution of mineralized apatite-ilmenite with a total area of 1,617 ha. The most prioritized areas for apatite-ilmenite mineral exploitation are located in Air Seruk Village's IUP (Izin Usaha Pertambangan/Mining Business License), Sijuk Village's IUP, and Batu Itam Village's IUP. This study also illustrates the orientation of the metal utilization of apatite-ilmenite in district Sijuk.

**Keywords:** *Apatite-ilmenite; fuzzy logic; Landsat 8; Rare earth elements*

**SPECTRAL ANALYSIS OF THE HIMAWARI-8 DATA FOR HOTSPOT DETECTION FROM LAND/FOREST FIRES IN SUMATRA/ Hana Listi Fitriana, Sayidah Sulma, suwarsono, Any Zubaidah, Indah Prasasti IJRESES, 15 (1) 2018 : 15-24**

Himawari-8 is the last generation of the low spatial resolution satellite imagery that has capability to detect the thermal variation on the earth of every 10 minute. This must be very potential to be used for detecting land/forest fire. This paper has explored the spectral prospective of the Himawari-8 for detecting land/forest fire hotspot. The main objective for this study is to identify the potential use of Himawari-8 for detecting of land forest fire hotspot. The study area was performed in Ogan Komering Ilir, South of Sumatra, which on 2015 occur great forest/land fire event. The main process included in this study are image projection, training sample collection and spectral statistical analysis measured by calculate statistic, they are average values, standard deviation values from reflectance visible band value and brightness temperature value, beside that validation of data obtained from medium resolution data of Landsat 8 with the similar acquisition time. The study found that the Himawari-8 has good capacity to identify land/forest fire hotspot as expressed for high accuracy assessment using band 3 and band 7.

**Keywords:** *Himawari-8; hotspot; spectral*

**International Journal of  
Remote Sensing and Earth Sciences**

P-ISSN 0216 – 6739; E- ISSN 2549-516X

Vol. 15 No. 1 June 2018

Accreditation No. 30/E/KPT/2018

The abstract may be copied without permission or charge

ABSTRACT

**THREE-WAY ERROR ANALYSIS OF SEA SURFACE TEMPERATURE (SST) BETWEEN HIMAWARI-8, BUOY, AND MUR SST IN SAVU SEA/ Bambang Sukresno, Rizki Hanintyo, Denny Wijaya Kusuma, Dinarika Jatisworo, Ari Murdimanto, Rizki Hanintyo, Denny Wijaya Kusuma, Dinarika, Jatisworo, Ari Murdimanto IJRESES, 15 (1) 2018 : 25-36**

Variance errors of Himawari-8, buoy, and Multi-scale Ultra-high Resolution (MUR) SST in Savu Sea have been investigated. This research used level 3 Himawari-8 hourly SST, in situ measurement of buoy, and daily MUR SST in the period of December 2016 to July 2017. The data were separated into day time data and night time. Skin temperature of Himawari-8 and subskin temperature of MUR SST were corrected with the value of  $15 \hat{\Delta} T_{\text{dept}}$  before compared with buoy data. Hourly SST of Himawari-8 and buoy data were converted to daily format by averaging process before collocated with MUR SST data. The number of 2,264 matchup data are obtained. Differences average between Himawari-8, buoy and MUR SST were calculated to get the value of variance ( $V_{ij}$ ). Using three-way error analysis, variance errors of each observation type can be known. From the analysis results can be seen that the variance error of Himawari-8, buoy and MUR SST are 2.5 oC, 0.28oC and 1.21oC respectively. The accuracy of buoy data was better than the other. With a small variance errors, thus buoy data can be used as a reference data for validation of SST from different observation type.

**Keywords:** *Sea surface temperature (SST); Himawari-8; Buoy data; MUR SST; Validation*

**BIOMASS ESTIMATION MODEL FOR MANGROVE FOREST USING MEDIUM-RESOLUTION IMAGERIES IN BSN CO LTD CONCESSION AREA, WEST KALIMANTAN/ Sendi Yusandi, I Nengah Surati Jaya, Fairus Mulia IJRESES, 15 (1) 2018: 37-50**

Mangrove forest is one of the forest ecosystem types that have the highest carbon stock in the tropics. Mangrove forests have a good assimilation capability with their environmental elements as well as on carbon sequestration. However, the availability of data and information on carbon storage, especially on tree biomass content of mangrove is still limited. Conventionally, an accurate estimation of biomass could be obtained from terrestrial measurements, but those methods are very costly and time-consuming. This study offered an alternative solution to overcome these limitations by using remote sensing technology, i.e. by using Landsat 8 and SPOT 5. The objective of this study is to formulate the biomass estimation model using medium resolution satellite imagery, as well as to develop a biomass distribution map based on the selected model. The study found that the NDVI of Landsat 8 and SPOT 5 have considerably high correlation coefficients with the standing biomass with a value of higher than 0.7071. On the basis of the values of aggregation deviation, mean deviation, bias, RMSE,  $\chi^2$ ,  $R^2$ , and  $s$ , the best model for estimating the mangrove stand biomass for Landsat 8 is  $B=0.00023404 e(20 \text{ NDVI})$  with the  $R^2$  value of 77.1% and  $B=0.36+25.5 \text{ NDVI}^2$  with the  $R^2$  value of 49.9% for SPOT 5. In general, the concession area of Bina Silva Nusa (BSN) Group (PT Kandelia Alam and PT Bina Ovivipari Semesta) have the potential of biomass ranging from 45 to 100 ton per ha.

**Keywords:** *mangrove forests; biomass; model; score; NDVI*

**International Journal of  
Remote Sensing and Earth Sciences**

P-ISSN 0216 – 6739; E- ISSN 2549-516X

Vol. 15 No. 1 June 2018

Accreditation No. 30/E/KPT/2018

The abstract may be copied without permission or charge

ABSTRACT

**STUDY ON POTENTIAL FISHING ZONES (PFZ) INFORMATION BASED ON S-NPP VIIRS AND HIMAWARI-8 SATELLITES DATA/ Sartono Marpaung, Teguh Prayogo, Kuncoro Teguh Setiawan, Orbita Roswintiarti**  
**IJRESES, 15 (1) 2018: 51-62**

Sea surface temperature (SST) data from S-NPP VIIRS satellite has different spatial resolution with SST data from Himawari-8 satellite. In this study comparative analysis of potential fishing zones information from both satellites has been conducted. The analysis was conducted on three project areas (PA 7, PA 13, PA 19) as a representation Indonesian territorial waters. The data used were daily for both satellites with a period time from August 2016 to December 2016. The method used was Single Image Detection (SIED) to detect thermal fronts. Method of mass center point for determining potential fishing zones coordinate point from result thermal front detection. Furthermore, an analysis of overlapping was done to compare the coordinate point information from both satellites. Based on data analysis that had been done, the result showed that potential fishing zones coordinate points of Himawari-8 satellite was mostly far from potential fishing zones coordinate point of S-NPP VIIRS. The coordinate points whose positions were close together or nearly same from both satellites was only about 20 %. Differences in potential fishing zones coordinate positions occur due to the effect of different spatial resolutions of both satellite data and the size of the front thermal events that had high variability. The ideal potential fishing zones coordinate points information was probably a combination of the potential fishing zones coordinate points of S-NPP VIIRS and Himawari-8 by making two adjacent coordinate points to be a single coordinate point. Field validation testing was required to prove the accuracy of the coordinate point.

**Keywords:** Potential fishing zones; S-NPP VIIRS; Himawari-8; satellite; coordinate points

**WATERMARKING METHOD OF REMOTE SENSING DATA USING STEGANOGRAPHY TECHNIQUE BASED ON LEAST SIGNIFICANT BIT HIDING/ Destri Yanti Hutapea, Octaviani Hutapea**  
**IJRESES, 15 (1) 2018: 63-70**

Remote sensing satellite imagery is currently needed to support the needs of information in various fields. Distribution of remote sensing data to users is done through electronic media. Therefore, it is necessary to make security and identity on remote sensing satellite images so that its function is not misused. This paper describes a method of adding confidential information to medium resolution remote sensing satellite images to identify the image using steganography technique. Steganography with the Least Significant Bit (LSB) method is chosen because the insertion of confidential information on the image is performed on the rightmost bits in each byte of data, where the rightmost bit has the smallest value. The experiment was performed on three Landsat 8 images with different area on each composite band 4,3,2 (true color) and 6,5,3 (false color). Visually the data that has been inserted information does not change with the original data. Visually, the image that has been inserted with confidential information (or stego image) is the same as the original image. Both images cannot be distinguished on histogram analysis. The Mean Squared Error value of stego images of all three data less than 0.053 compared with the original image. This means that information security with steganographic techniques using the ideal LSB method is used on remote sensing satellite imagery.

**Keywords:** *Steganography; least significant bit; security*

**International Journal of  
Remote Sensing and Earth Sciences**

P-ISSN 0216 – 6739; E- ISSN 2549-516X  
Accreditation No. 30/E/KPT/2018

Vol. 15 No. 1 June 2018

The abstract may be copied without permission or charge

ABSTRACT

**LAPAN-A3 SATELLITE DATA ANALYSIS FOR LAND COVER CLASSIFICATION (CASE STUDY: TOBA LAKE AREA, NORTH SUMATRA)/ Jalu Tejo Nugroho, Zylshal, Dony Kushardono  
IJRESES, 15 (1) 2018: 71-80**

LAPAN-A3 is the 3<sup>rd</sup> generation satellite for remote sensing developed by National Institute of Aeronautics and Space (LAPAN). The camera provides imagery with 15 m spatial resolution and able to view a swath 120 km wide. This research analyzes the performance of LAPAN-A3 satellite data to classify land cover in Toba Lake area, North Sumatera. Data processing starts from the selection of region of interest up to the assessment of accuracy. Supervised classification with maximum likelihood approach and confusion matrix method was applied to classify and evaluate the assessment results. The land cover is classified into five classes; water, bare land, agriculture, forest and secondary forest. The result of accuracy test is 93.71%. It proves that LAPAN-A3 data could classify the land cover accurately. The data is expected to complement the need of the satellite data with medium spatial resolution.

**Keywords:** *LAPAN-A3 micro satellite; land cover; pixel-based classification*

**COMPARISON OF MODEL ACCURACY IN TREE CANOPY DENSITY ESTIMATION USING SINGLE BAND, VEGETATION INDICES AND FOREST CANOPY DENSITY (FCD) BASED ON LANDSAT-8 IMAGERY (CASE STUDY: PEAT SWAMP FOREST IN RIAU PROVINCE) /Faisal Ashaari, Muhammad Kamal, Dede Dirgahayu  
IJRESES, 15 (1) 2018: 81-92**

Identification of a tree canopy density information may use remote sensing data such as Landsat-8 imagery. Remote sensing technology such as digital image processing methods could be used to estimate the tree canopy density. The purpose of this research was to compare the results of accuracy of each method for estimating the tree canopy density and determine the best method for mapping the tree canopy density at the site of research. The methods used in the estimation of the tree canopy density are Single band (green, red, and near-infrared band), vegetation indices (NDVI, SAVI, and MSARVI), and Forest Canopy Density (FCD) model. The test results showed that the accuracy of each method: green 73.66%, red 75.63%, near-infrared 75.26%, NDVI 79.42%, SAVI 82.01%, MSARVI 82.65%, and FCD model 81.27%. Comparison of the accuracy results from the seventh methods indicated that MSARVI is the best method to estimate tree canopy density based on Landsat-8 at the site of research. Estimation tree canopy density with MSARVI method showed that the canopy density at the site of research predominantly 60-70% which spread evenly.

**Keywords:** *Tree canopy density; single band; vegetation indices; FCD*

**International Journal of  
Remote Sensing and Earth Sciences**

P-ISSN 0216 – 6739; E- ISSN 2549-516X  
Accreditation No. 30/E/KPT/2018

Vol. 15 No. 1 June 2018

The abstract may be copied without permission or charge

ABSTRACT

**ANALYSIS OF LAND USE SPATIAL PATTERN CHANGE OF TOWN DEVELOPMENT USING REMOTE SENSING/ Samsul Arifin, Mukhoriyah, Dipo Yudhatama  
IJRESES, 15 (1) 2018: 93-102**

The Assessment of the physical character of a city is considered relatively easier than the social-cultural aspects. It is important to recognize the type of city form and to predict the behavior of people in the city and its surrounding. Due to those characteristics, the study of the pattern of physical development of the city is required. The objective of research is to analyze the change of spatial pattern of the city due to the city growing by remote sensing. The multitemporal data of Landsat 5/7/8 year 2000, 2006 and 2015 in Jabodetabek area were used. The classification technique had been done and it produced five classes of land uses. Those are water, built-up area, vegetation, other land use and no data. The results of the analysis in Jabodetabek area (Jakarta, Bogor, Depok, Tangerang and Bekasi) show that there was land use changes from vegetation and other land use area to built-up area with an average accuracy of 78% in each year. The pattern of physical development of the city looks linear from year 2000 until year 2006, which is confirmed as concentric pattern from year 2006 to 2015. Based on those analysis, it confirmed that the city development in Jakarta as the center was influenced by the spatial land development of the surrounding cities of Depok, Bogor, Bekasi and Tangerang. The pattern of spatial development from 2000 to 2006 in Bogor, Bekasi and Depok areas is Linear pattern, whereas from 2006 - 2015 the pattern of spatial development shows Propagation Concentric pattern. For Tangerang Region in 2000-2015 its development is patterned Propagation Concentric.

**Keywords:** *Analysis; Spatial; Remote Sensing; Pattern; Development*

**International Journal of  
Remote Sensing and Earth Sciences**

P-ISSN 0216 – 6739; E- ISSN 2549-516X  
Accreditation No. 30/E/KPT/2018

Vol. 15 No. 2 December 2018

The abstract may be copied without permission or charge

ABSTRACT

**ACCURACY EVALUATION OF STRUCTURE FROM MOTION THERMAL MOSAICING IN THE CENTER OF TOKYO/ Atik Nurwanda, Tsuyoshi Honjo, Nobumitsu Tsunematsu, Hitoshi Yokoyama IJRESES, 15 (2) 2018: 103-112**

In the airborne and high-resolution measurement of Land Surface Temperature (LST) over large area, capturing and synthesizing of many images are necessary. In the conventional method, the process of georeferencing a large number of LST images is necessary to make one large image. Structure from Motion (SfM) technique was applied to automatized the georeferencing process. We called it "SfM Thermal Mosaicing". The objective of this study is to evaluate the accuracy of SfM thermal mosaicing in making an orthogonal LST image. By using airborne thermal images in the center of Tokyo, the LST image with the 2m resolution was created by using SfM thermal mosaicing. Its accuracy was then analyzed. The result showed that in the whole examined area, the mean error distance was 4.22m and in the small parts of the examined area, the mean the error distance was about 2m. Considering the image resolution, the error was minimal indicating good performance of the SfM thermal mosaicing. Another advantage of SfM thermal mosaicing is that it can make precise orthogonal LST image. With the progress of UAV and thermal cameras, the proposed method will be a powerful tool for the environmental researches on the LST.

*Keywords: accuracy evaluation; the center of Tokyo; georeferencing; structure from motion; land surface temperature; orthogonal*

**ANALYSIS OF ANTENNA SPECIFICATION FOR VERY HIGH RESOLUTION SATELLITE DATA ACQUISITION THROUGH DIRECT RECEIVING SYSTEM (DRS)/ Muchammad Soleh, Ali Syahputra Nasution, Arif Hidayat, Hidayat Gunawan, Ayom Widipaminto IJRESES, 15 (2) 2018: 113-130**

Very High Resolution Satellite Image (VHRSI) data for Indonesian Government license is required by ministries/agencies, TNI, police, and local government to support national programs. But Indonesia did not have a VHRSI data recipient facility to directly acquire this data. In accordance with Law 21/2013 on Space, LAPAN is mandate to provide high resolution satellite data, and based on a roadmap for provision of satellite data in 2017, LAPAN will provide a VHRSI data reception facility through direct receiving system (DRS). This will be more efficient than other methods in providing the data. Priority provision of satellite data is for acquiring Pleiades and TerraSAR-X operating in the frequency range 8 GHz (X-Band). Therefore, to receive both data, it requires antenna subsystem with optimum coverage throughout Indonesia. Parameters to obtain the minimum antenna specifications include Free Space Loss (FSL), Carrier to Noise Ratio (C/No) and Antenna Gain to Noise Temperature (G/T). The calculation of G/T antenna is done for both satellites based on satellite parameters and analysis of antenna product availability in the market. Based on the calculation of satellite parameters shows that the minimum G/T value with the elevation of 5 degrees is 27.71 dB/K for Pleiades data reception and the minimum G/T value of 26.10 dB/K for the TerraSAR-X data reception. In general, the minimum G/T value for receiving the Pleiades and TerraSAR-X data is at 28 dB/K. While based on the calculation of antenna products availability in the market is require G/T value of 33.45 dB /K for the elevation of 5 degrees with a diameter of 7.5 mm antenna. This can be conclude that the antenna products meets the minimum requirements specification and to receive both satellite data. However, both calculation for the antenna subsystem still will be evaluated further in order to be directly installed at Parepare Remote Earth Station (SPBJ), South Sulawesi.

*Keywords: VHRSI; Optic; SAR; Direct Receiving System (DRS); Antenna*

**International Journal of  
Remote Sensing and Earth Sciences**

P-ISSN 0216 – 6739; E- ISSN 2549-516X

Vol. 15 No. 2 December 2018

Accreditation No. 30/E/KPT/2018

The abstract may be copied without permission or charge

ABSTRACT

**OBSERVING THE INUNDATED AREA USING LANDSAT-8 MULTITEMPORAL IMAGES AND DETERMINATION OF FLOOD-PRONE AREA IN BANDUNG BASIN/Fajar Yulianto, Suwarsono, Sayidah Sulma, Muhammad Rokhis Khomarudin IJRESES, 15 (2) 2018: 131-140**

Flood is the most frequent hydro-meteorological disaster in Indonesia. Flood disasters in the Bandung basin result from increasing population density, especially in the Citarum riverbank area, accompanied by land use changes in upstream of the Citarum catchment area which has disrupted the river's function. One of the basic issues that need to be investigated is which areas of the Bandung basin are prone to flooding. This study offers an effective and efficient method of mapping flood-prone areas based on flood events that have occurred in the past through the use of historical remote sensing image data. In this research, Landsat-8 imagery was used to observe the inundated area in the Bandung basin in the past (2014–2018) using an improved algorithm, the modified normalized water index (MNDWI). The results of the study show that MNDWI is the appropriate parameter to be used to detect flooded areas in the Bandung basin area that have heterogeneous land surface conditions. The flood-prone area was determined based on flood events for 2014 to 2018, identified as inundated areas in the images. The estimation of the flood-prone area in the Bandung basin is 11,886.87 ha. Most of the flood-prone areas are in the subdistricts of Rancaekek, Bojongsoang, Solokan Jeruk, Ciparay, Cileunyi, Bale Endah and Cikancung. This area geographically or naturally is a water habitat area. Therefore, if the area will be used for residential, this will have consequences that flood will always be a threat to the area.

Keywords: *inundated area; flood-prone area; Bandung basin; Landsat-8; MNDWI*

**MANGROVE FOREST CHANGE IN NUSA PENIDA MARINE PROTECTED AREA, BALI - INDONESIA USING LANDSAT SATELLITE IMAGERY/August Daulat, Widodo Setiyo Pranowo, Syahrial Nur Amri IJRESES, 15 (2) 2018: 141-156**

Nusa Penida, Bali was designated as a Marine Protected Area (MPA) by the Klungkung Local Government in 2010 with support from the Ministry of Marine Affairs and Fisheries, Republic of Indonesia. Mangrove forests located in Nusa Lembongan Island inside the Nusa Penida MPA jurisdiction have decreased in biomass quality and vegetation cover. It's over the last decades due to influences from natural phenomena and human activities, which obstruct mangrove growth. Study the mangrove forest changes related to the marine protected areas implementation are important to explain the impact of the regulation and its influence on future conservation management in the region. Mangrove forest in Nusa Penida MPA can be monitored using remote sensing technology, specifically Normalized Difference Vegetation Index (NDVI) from Landsat satellite imagery combined with visual and statistical analysis. The NDVI helps in identifying the health of vegetation cover in the region across three different time frames 2003, 2010, and 2017. The results showed that the NDVI decreased slightly between 2003 and 2010. It's also increased significantly by 2017, where a mostly positive change occurred landwards and adverse change happened in the middle of the mangrove forest towards the sea.

Keywords: *mangrove changes; Nusa Penida MPA; remote sensing; NDVI*



**International Journal of  
Remote Sensing and Earth Sciences**

P-ISSN 0216 – 6739; E- ISSN 2549-516X  
Accreditation No. 30/E/KPT/2018

Vol. 15 No. 2 December 2018

The abstract may be copied without permission or charge

ABSTRACT

**DETECTING THE LAVA FLOW DEPOSITS FROM 2018 ANAK KRAKATAU ERUPTION USING DATA FUSION LANDSAT-8 OPTIC AND SENTINEL-1 SAR/ Suwarsono, Indah Prasasti, Jalu Tejo Nugroho, Jansen Sitorus, Djoko Triyono  
IJRESES, 15 (2) 2018: 157-166**

The increasing volcanic activity of Anak Krakatau volcano has raised concerns about a major disaster in the area around the Sunda Strait. The objective of the research is to fuse Landsat-8 OLI (Operational Land Imager) and Sentinel-1 TOPS (Terrain Observation with Progressive Scans), an integration of SAR and optic remote sensing data, in observing the lava flow deposits resulted from Anak Krakatau eruption during the middle 2018 eruption. RGBI and the Brovey transformation were conducted to merge (fuse) the optical and SAR data. The results showed that optical and SAR data fusion sharpened the appearance of volcano morphology and lava flow deposits. The regions are often constrained by cloud cover and volcanic ash, which occurs at the time of the volcanic eruption. The RGBI-VV and Brovey RGB-VV methods provide better display quality results in revealing the morphology of volcanic cone and lava deposits. The entire slopes of Anak Krakatau Volcano, with a radius of about 1 km from the crater is an area prone to incandescent lava and pyroclastic falls. The direction of the lava flow has the potential to spread in all directions. The fusion method of optical Landsat-8 and Sentinel-1 SAR data can be used continuously in monitoring the activity of Anak Krakatau volcano and other volcanoes in Indonesia both in cloudy and clear weather conditions.

*Keywords: lava flow; Anak Krakatau; data fusion; Landsat-8; Sentinel-1 SAR*

**GEOMETRIC ASPECTS EVALUATION OF GNSS CONTROL NETWORK FOR DEFORMATION MONITORING IN THE JATIGEDE DAM REGION/Made Ditha Ary Sanjaya, T. Aris Sunantyo, Nurrohmat Widjajanti  
IJRESES, 15 (2) 2018: 167-176**

Many factors led to dam construction failure so that deformation monitoring activities is needed in the area of the dam. Deformation monitoring is performed in order to detect a displacement at the control points of the dam. Jatigede Dam deformation monitoring system has been installed and started to operate, but there has been no evaluation of the geometry quality of control networks treated with IGS points for GNSS networks processing. Therefore, this study aims to evaluate the geometric quality of GNSS control networks on deformation monitoring of Jatigede Dam area. This research data includes the GNSS measurements of five CORS Jatigede Dam stations (R01, GG01, GCP04, GCP06, and GCP08) at doy 233 with network configuration scenarios of 12 IGS points on two quadrants (jat1), three quadrants (jat2), and four quadrants (jat3 and jat4). GNSS networks processing was done by GAMIT to obtain baseline vectors, followed by network processing using parameter method of least squares adjustment. Networks processing with least squares adjustment aims to determine the most optimal by precision and reliability criterion. Results of this study indicate that network configuration with 12 IGS stations in the two quadrants provides the most accurate coordinates of CORS dam stations. Standard deviations value of CORS station given by jat1 configuration are in the range of 2.7 up to 4.1 cm in X-Z components, whereas standard deviations in the Y component are in the range 5.8 up to 6.9 cm. An optimization assessment based on network strength, precision, and reliability factors shows optimum configuration by jat1.

*Keywords: Jatigede dam; control network; IGS; GNSS*

**International Journal of  
Remote Sensing and Earth Sciences**

P-ISSN 0216 – 6739; E- ISSN 2549-516X

Vol. 15 No. 2 December 2018

Accreditation No. 30/E/KPT/2018

The abstract may be copied without permission or charge

ABSTRACT

**PRELIMINARY STUDY OF HORIZONTAL AND VERTICAL WIND PROFILE OF QUASI-LINEAR CONVECTIVE UTILIZING WEATHER RADAR OVER WESTERN JAVA REGION, INDONESIA /Abdullah Ali, Riris Adrianto, Miming Saepudin IJRESES, 15 (2) 2018: 177-186**

One of the weather phenomena that potentially cause extreme weather conditions is the linear-shaped mesoscale convective systems, including squall lines. The phenomenon that can be categorized as a squall line is a convective cloud pair with the linear pattern of more than 100 km length and 6 hours lifetime. The new theory explained that the cloud system with the same morphology as squall line without longevity threshold. Such a cloud system is so-called Quasi-Linear Convective System (QLCS), which strongly influenced by the ambient dynamic processes, include horizontal and vertical wind profiles. This research is intended as a preliminary study for horizontal and vertical wind profiles of QLCS developed over the Western Java region utilizing Doppler weather radar. The following parameters were analyzed in this research, include direction pattern and spatial-temporal significance of wind speed, divergence profile, vertical wind shear (VWS) direction, and intensity profiles, and vertical velocity profile. The subjective and objective analysis was applied to explain the characteristics and effects of those parameters to the orientation of propagation, relative direction, and speed of the cloud system's movement, and the lifetime of the system. Analysis results showed that the movement of the system was affected by wind direction and velocity patterns. The divergence profile combined with the vertical velocity profile represents the inflow which can supply water vapor for QLCS convective cloud cluster. Vertical wind shear that effect QLCS system is only its direction relative to the QLCS propagation, while the intensity didn't have a significant effect.

*Keywords: horizontal and vertical wind profile; QLCS; doppler weather radar; Western Java Region; Indonesia*

**PRELIMINARY DETECTION OF GEOTHERMAL MANIFESTATION POTENTIAL USING MICROWAVE SATELLITE REMOTE SENSING/Atriyon Julzarika, Udhi Catur Nugroho IJRESES, 15 (2) 2018: 187-198**

The satellite technology has developed significantly. The sensors of remote sensing satellites are in the form of optical, Microwave, and LIDAR. These sensors can be used for energy and mineral resources applications. The example of those applications are height model and the potential of geothermal manifestation detection. This study aims to detect the potential of geothermal manifestation using remote sensing. The study area is the Northern of the Inverse Arc of Sulawesi. The method used is remote sensing approach for its preliminary detection with 4 steps as follow (a) mining land identification, (b) geological parameter extraction, (c) preparation of standardized spatial data, and (d) geothermal manifestation. Mining lands identification is using Vegetation Index Differencing method. Geological parameters include structural geology, height model, and gravity model. The integration method is used for height model. The height model integration use ALOS PALSAR data, Icesat/GLAS, SRTM, and X SAR. Structural geology use dip and strike method. Gravity model use physical geodesy approach. Preparation of standardized spatial data with re-classed and analyzed using Geographic Information System between each geological parameter, whereas physical geodesy methods are used for geothermal manifestation detection. Geothermal manifestation using physical geodesy approach in Barthelmes method. Grace and GOCE data are used for gravity model. The geothermal manifestation detected from any parameter is analyzed by using geographic information system method. The result of this study is 10 area of geothermal manifestation potential. The accuracy test of this research is 87.5 % in 1.96  $\sigma$ . This research can be done efficiently and cost-effectively in the process. The results can be used for various geological and mining applications.

*Keywords: The Northern of Inverse Arc of Sulawesi; geothermal manifestation; remote sensing; gravity model*

**International Journal of  
Remote Sensing and Earth Sciences**

P-ISSN 0216 – 6739; E- ISSN 2549-516X

Vol. 15 No. 2 December 2018

Accreditation No. 30/E/KPT/2018

The abstract may be copied without permission or charge

ABSTRACT

**THE UTILIZATION OF REMOTE SENSING DATA TO SUPPORT GREEN OPEN SPACE MAPPING IN JAKARTA, INDONESIA/Hana Listi Fitriana, Sayidah Sulma, Nur Febrianti, Jalu Tejo Nugroho, Nanik Suryo Haryani  
IJRESES, 15 (2) 2018: 199-208**

Green open space becomes critical in maintaining the balance of the environment and improving the quality of urban living for a healthy life. The use of remote sensing data for calculation of green open space has been done notably using NDVI (Normalized Difference Vegetation Index) method from Landsat 8 and SPOT data. This research aims to calculate the accuracy of the green open space classification from multispectral data of Landsat 8 and SPOT 6 using the NDVI methods. Green open space could be assessed from the value NDVI. The value of NDVI generated from Landsat 8 and SPOT 6's Red and NIR channels. The accuracy of NDVI values is then examined by comparing with Pleiades data. Pleiades data which has 50 cm panchromatic resolution and 2 m multispectral with 4 bands (B, G, R, NIR) can precisely visualize objects. So, it can be used as the reference in the calculation of the green open space based on NDVI. The results of the accuracy testing of Landsat 8 and SPOT 6 image could be used to identify the green open space by using NDVI SPOT of 6 can increase the accuracy of 5.36% from Landsat 8.

**Keywords:** *green open space; NDVI; Remote sensing*

# ACCURACY EVALUATION OF STRUCTURE FROM MOTION THERMAL MOSAICING IN THE CENTER OF TOKYO

Atik Nurwanda<sup>1</sup>, Tsuyoshi Honjo<sup>1\*</sup>, Nobumitsu Tsunematsu<sup>2</sup>, and Hitoshi Yokoyama<sup>3</sup>

<sup>1</sup>Graduate School of Horticulture, Chiba University, 648, Matsudo, Matsudo-shi, Chiba, Japan.

<sup>2</sup>Tokyo Metropolitan Research Institute for Environmental Protection, Tokyo Environmental Public Service Corporation, 1-7-5 Shinsuna, Koto-ku, Tokyo, Japan.

<sup>3</sup>National Research Institute for Earth Science and Disaster Resilience, 3-1 Tennodai, Tsukuba-shi, Ibaraki, Japan.

\*e-mail: honjo@faculty.chiba-u.jp

Received: 11 December 2017; Revised: 12 October 2018; Approved: 6 December 2018

**Abstract.** In the airborne and high-resolution measurement of Land Surface Temperature (LST) over large area, capturing and synthesizing of many images are necessary. In the conventional method, the process of georeferencing a large number of LST images is necessary to make one large image. Structure from Motion (SfM) technique was applied to automatized the georeferencing process. We called it "SfM Thermal Mosaicing". The objective of this study is to evaluate the accuracy of SfM thermal mosaicing in making an orthogonal LST image. By using airborne thermal images in the center of Tokyo, the LST image with the 2m resolution was created by using SfM thermal mosaicing. Its accuracy was then analyzed. The result showed that in the whole examined area, the mean error distance was 4.22m and in the small parts of the examined area, the mean the error distance was about 2m. Considering the image resolution, the error was minimal indicating good performance of the SfM thermal mosaicing. Another advantage of SfM thermal mosaicing is that it can make precise orthogonal LST image. With the progress of UAV and thermal cameras, the proposed method will be a powerful tool for the environmental researches on the LST.

Keywords: *accuracy evaluation, the center of Tokyo, georeferencing, structure from motion, land surface temperature, orthogonal.*

## 1 INTRODUCTION

Land surface temperature (LST) is widely used in urban heat island (UHI) studies and other environmental researches. There have many studies which analyzed the LST of satellite images (Chen *et al.* 2014; Connors *et al.* 2013; Dousset and Gourmelon 2013; Estoque *et al.* 2017; Streutker 2002; Weng *et al.* 2004). The resolution of commonly used satellite-derived LST are 100m (Landsat 8 TIRS), 60m (Landsat ETM), 90m (Terra ASTER), Landsat TM (120m), 1km (MODIS), 1.1km (NOAA), 1km (ENVISAT), and 3km (Meteosat) (Darlington *et al.* 2017). Airborne measurement of high-resolution LST is

preferable to analyze the detail of urban environment because the size of roads and buildings are mostly less than 10m.

In the airborne and high-resolution measurement of LST over a large area, capturing and synthesizing of many images are necessary because the airborne thermal camera can only take the LST of a small area. In the conventional method, the process of georeferencing and mosaicing small LST images is necessary to make one large image. The manual positioning of many ground control points (GCPs) should be done in georeferencing of each LST images.

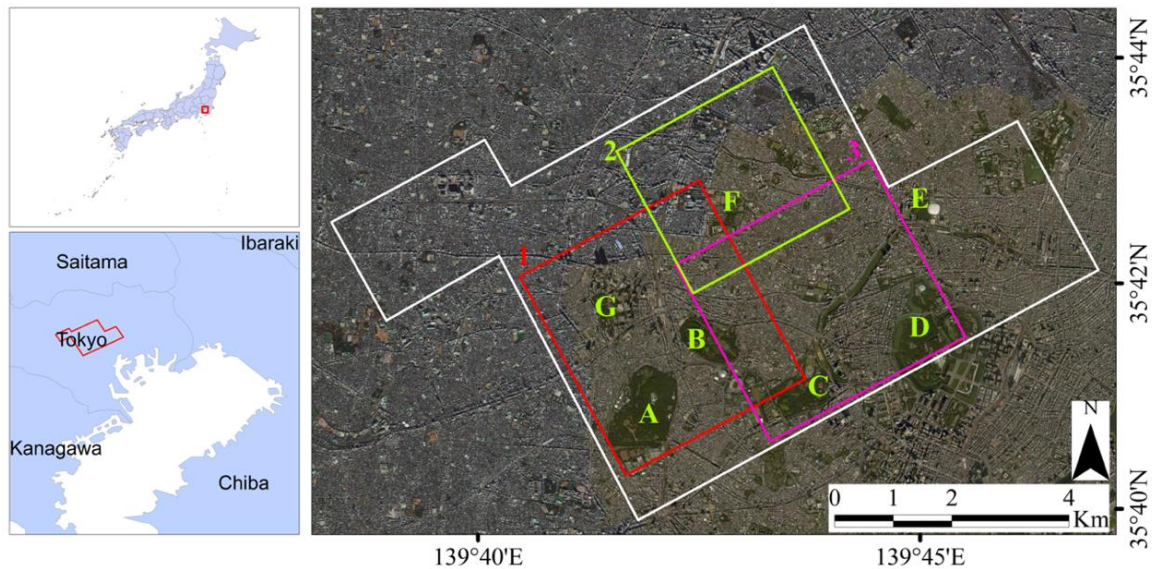


Figure 1-1: The area of interest in the center of Tokyo. The aerial photo on the map was taken on August 19th, 2014. The white border is a large area used for the analysis. The squares of 1, 2, and 3 are the small analyzed areas. (A. Yoyogi Park & Meiji Jingu Shrine, B. Shinjuku Goen National Garden, C. Akasaka Palace, D. Imperial Palace, E. Koishikawa Korakuen Garden, F. Korakuen Garden, and G. Shinjuku Chuo Park).

These processes require a lot of labor force and time if the images are in large quantities. Hence, this difficulty even influences the decision to make the measurement.

To solve this problem, Honjo *et al.* (2017) applied Structure from Motion (SfM) technique to the georeferencing and mosaicing process and named the process as “SfM thermal mosaicing”. Formally, thermal images were not used in the process of SfM because of its low resolution and low contrast, but in SfM thermal mosaicing only thermal images were used to make an orthogonal LST image. The method effectively reduces the labor of obtaining GCPs in georeferencing. Honjo *et al.* (2017) also analyzed the relation between urban LST change and urban morphology. In the study, the LSTs of the two periods were overlaid, and the difference was well detected. But in the overlaid process, the pixel to pixel coincidence was impossible, and the detailed analysis of the accuracy of the technique was not made. The quantitative accuracy measurement is necessary for the further application of

SfM thermal mosaicing to the LST analysis.

SfM has been used in many studies where 3D models were made from photographs (Colomina and Molina, 2014; Westoby *et al.* 2012), i.e., 3D mapping for surveying earthwork projects (Siebert and Teizer 2014), 3D mapping of vegetation spectral dynamics (Dandois and Ellis 2013), 3D reconstruction of sedimentary outcrops (Chesley *et al.* 2017), urban flood modelling (Meesuk *et al.* 2015), and topographic survey (James *et al.* 2017).

In this study, we evaluated the accuracy of LST image made by SfM thermal mosaicing process. By using airborne thermal images in the center of Tokyo, the LST image was made by using SfM thermal mosaicing, and its accuracy was measured. In the analysis of the accuracy, the LST image and Google Map image were overlaid, and the distances of the corresponding referenced points of both images are defined as an error distance. From the measurement of the error distances, we analyzed the accuracy of the method.

## 2 MATERIALS AND METHODOLOGY

### 2.1 Location and Data

The analyzed area is shown in Figure 1-1. It is the center area of Tokyo, including Shinjuku area and north area of Imperial Palace. The area is a typical urban area which includes high-rise buildings, low-rise buildings, and urban green areas (Imperial Palace, Shinjuku Gyoen National Garden, Yoyogi Park, Koishikawa Korakuen Garden, etc.). Airborne thermal images were used which were taken on August 19<sup>th</sup>, 2014 from the height of 600m above surface land.

### 2.2 SfM Thermal Mosaicing

The comparison of SfM thermal mosaicing and conventional method of manual georeferencing process are described in Figure 2-1. The original images are a small thermal image in the daytime and night-time. In SfM thermal mosaicing, we used 3065 daytime images

and 3097 night-time images. Each image is 599x451 pixels (8bit and grayscale) with 2m resolution. From the original images, we made daytime and night-time LST image. In SfM thermal mosaicing process, Photoscan Pro (Agisoft) was used. After the SfM thermal mosaicing process, the image was georeferenced only once on the map.

In the conventional method of manual georeferencing process (Figure 2-1, B), detecting at least three GCPs were necessary for each image and detection of GCPs should be done for all original images. After georeferencing process, the mosaicing process was executed to make the LST image. The human error for each georeferencing process affects the accuracy of LST image. To compare the SfM thermal mosaicing and manual georeferencing, daytime and night-time images made by Skymap Inc. was used as examples of manual georeferencing images (Figure 2-1, B3).

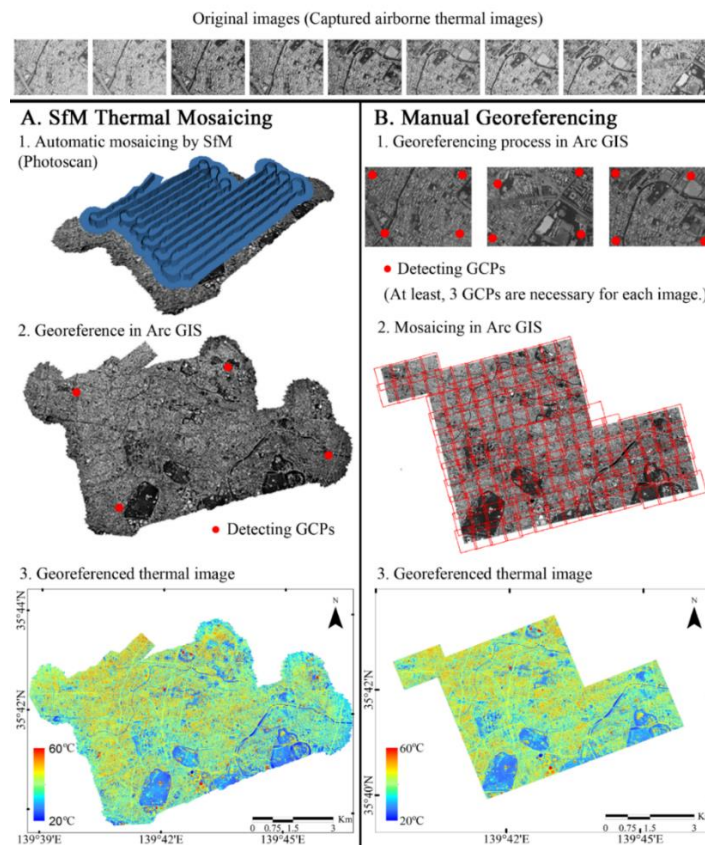


Figure 2-1: SfM thermal mosaicing and manual georeferencing



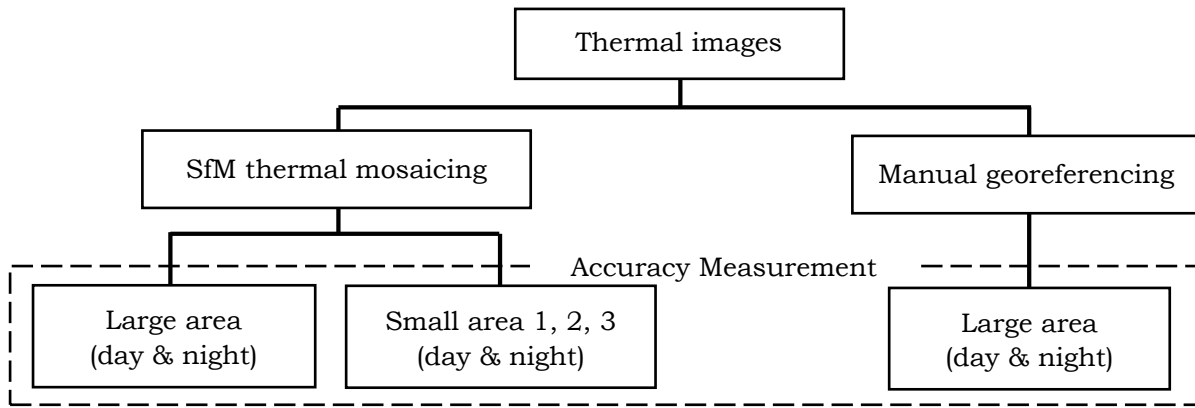


Figure 2-2: Flowchart of accuracy measurement

### 2.3 Accuracy Measurement

Flowchart of the accuracy assessment is shown in Figure 2-2. To measure the accuracy, we used SfM thermal mosaicing and manual georeferencing images of large area (whole analyzed area) both in daytime and night-time. We also analyzed small area (three small parts of the area shown as squares 1, 2 and 3 in Figure 1-1). In manual georeferencing, the only large area is analyzed because the error distance is relatively same either large and small areas. In the SfM thermal mosaicing, georeferencing process was - conducted once for large small areas, respectively. For accuracy evaluation, the accuracy of LST image was analyzed for large and small areas. The same procedure of accuracy analysis was conducted for a large area of manual georeferencing image.

Twenty sample points were selected at the point of the building edges, the cross-section center, and the corner of the bridges on each LST image in Figure 2-2 (a large area and three small areas in SfM thermal mosaicing, and a large area in manual georeferencing).

The accuracy measurement is illustrated in Figure 2-3. The red dot represents the reference point in Google Map which is the same place as the sample point of the overlaid LST image.

The distance between the reference point and the sample point was defined as the error distance. The error distance (*ED*) is expressed by the following formula:

$$ED = \sqrt{(x1 - x2)^2 + (y1 - y2)^2} \quad (2-1)$$

where,  $(x1, y1)$  is a reference point on the Google Map, and  $(x2, y2)$  is the sample point on the LST image. The error vector is also defined as  $(x2 - x1, y2 - y1)$ .

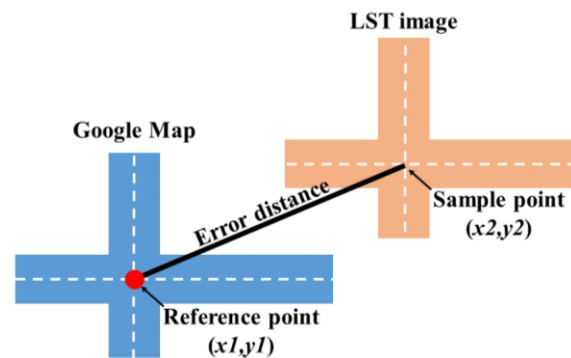


Figure 2-3: Diagram of measurement of error distance.

When the error distance value is low, it means the accuracy is high. The error distance measurement was conducted in Q-GIS which connected with Google Map. The error distance was adjusted as the mean x- and y-component of error distance become zero (0) as follows:

$$\sum (x_1 - x_2) = 0 \quad (2-2)$$

$$\sum (y_1 - y_2) = 0 \quad (2-3)$$

### 3 RESULTS AND DISCUSSION

#### 3.1 Daytime and Night-time LST Image with SfM Thermal Mosaicing

The LST images of the daytime and night-time large area by SfM thermal mosaicing are shown in Figure 3-1. The process of making the LST image of the large area took about 45 hours with PC for (CPU: Intel Core i7-4790K, Memory: 12GB). The result showed that the standard deviation of daytime LST images is 16.52°C and night-time LST image is 8.87°C. The standard deviation of daytime LST image was wider than that of night-time LST image because LST value was higher in the daytime. The standard deviation was quite wide range either in the daytime and nighttime representing the variety of the objects of the urban surface, i.e., water surfaces, green areas, roads, and buildings.

Daytime LST image is more clear and has a clear contrast because the temperature difference in the daytime LST distribution is larger than that in the night-time LST distribution. In the daytime, hot areas were observed in the building, the cross-section of roads, square, etc. Meanwhile, cool areas were observed in urban trees, lawn area (grass), and water. Edges of these objects were well recognized with the resolution of the images. On the other hand, the standard deviation of night-time LST image is relatively narrow. It implies the

recognition of the objects is slightly difficult in the night-time.

#### 3.2 The Accuracy of SfM Thermal Mosaicing

The error vectors in automatic georeferencing with SfM thermal mosaicing are shown in Figure 3-1. The red dot represents the center of the reference point, and the black line is the error distance. The directions of errors are randomly distributed. The error distance of daytime and night-time thermal images are 4.22m and 4.65m, respectively (Figure 3-4). The error distance of daytime thermal image is a slightly better than night-time thermal image. One of the reasons is that the objects in night-time thermal images were more obscure in the SfM thermal mosaicing.

In Figure 3-2, the accuracy of the small areas (1, 2, & 3) is shown. Comparing Figure 3-1 and Figure 3-2, the error distance of the small areas area mostly shorter than the error distance of the large area both day and night. The error distance of small areas ranges from 1.80m to 2.76m, while large area range from 4.22m to 5.18m (Figure 3-4).

#### 3.3 The Accuracy of Manual Georeferencing

The error vector of manual georeferencing of the large area is shown in Figure 3-3. The error vector is randomly distributed. As the result of the SfM thermal mosaicing in Figure 3-1, the error distance of manual georeferencing in daytime thermal image is slightly better than night-time thermal image.



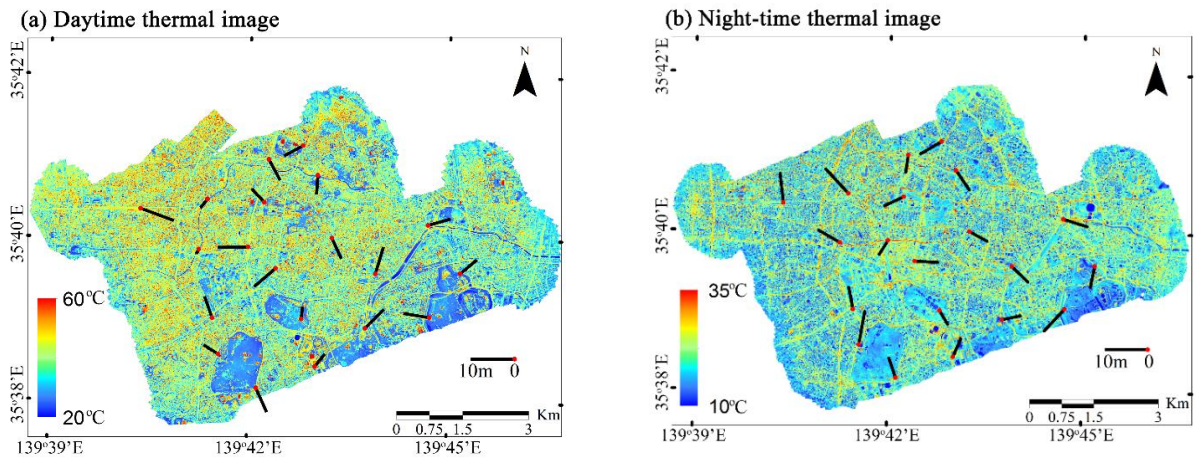


Figure 3-1: Images of error vector in SfM thermal mosaicing (large area).

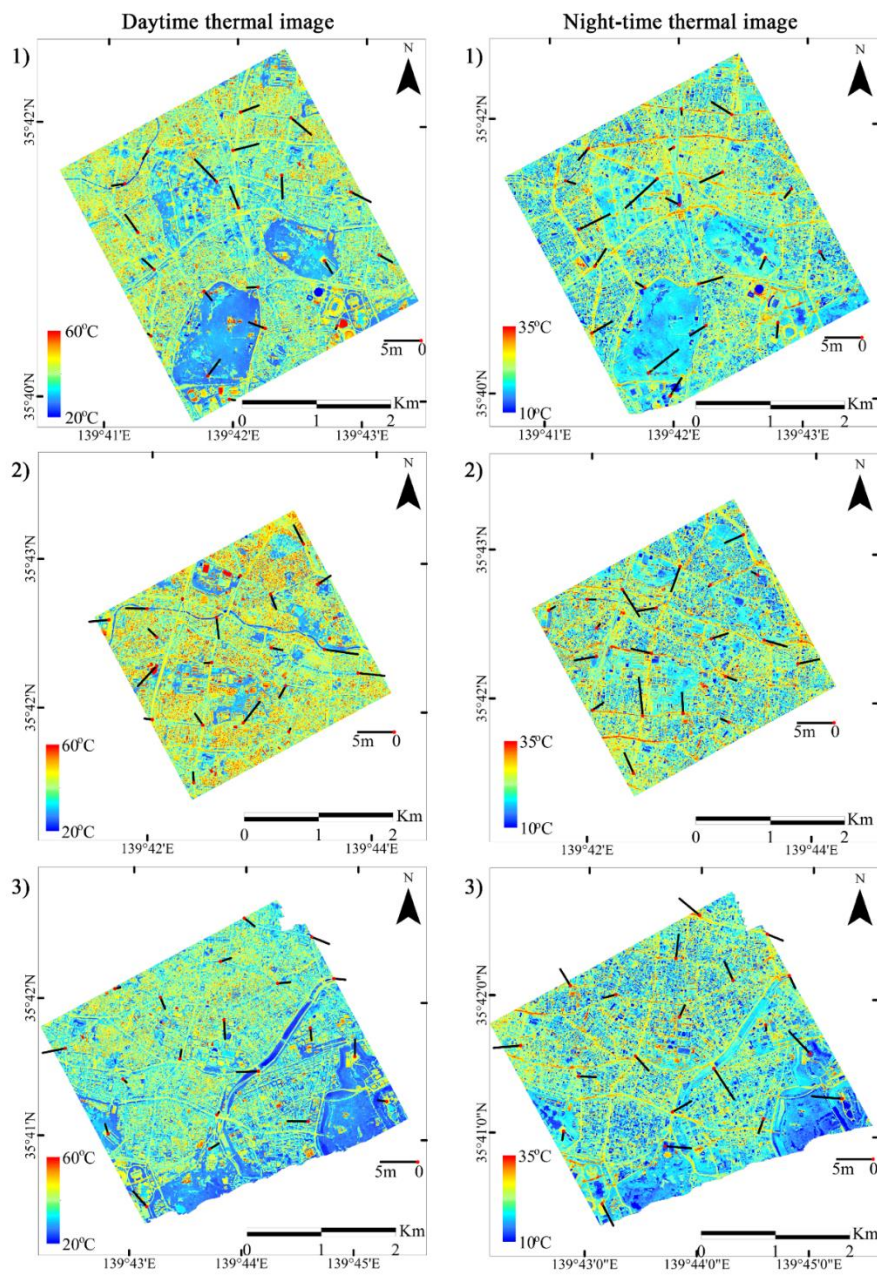


Figure 3-2: Images of error vector in SfM thermal mosaicing (small area).

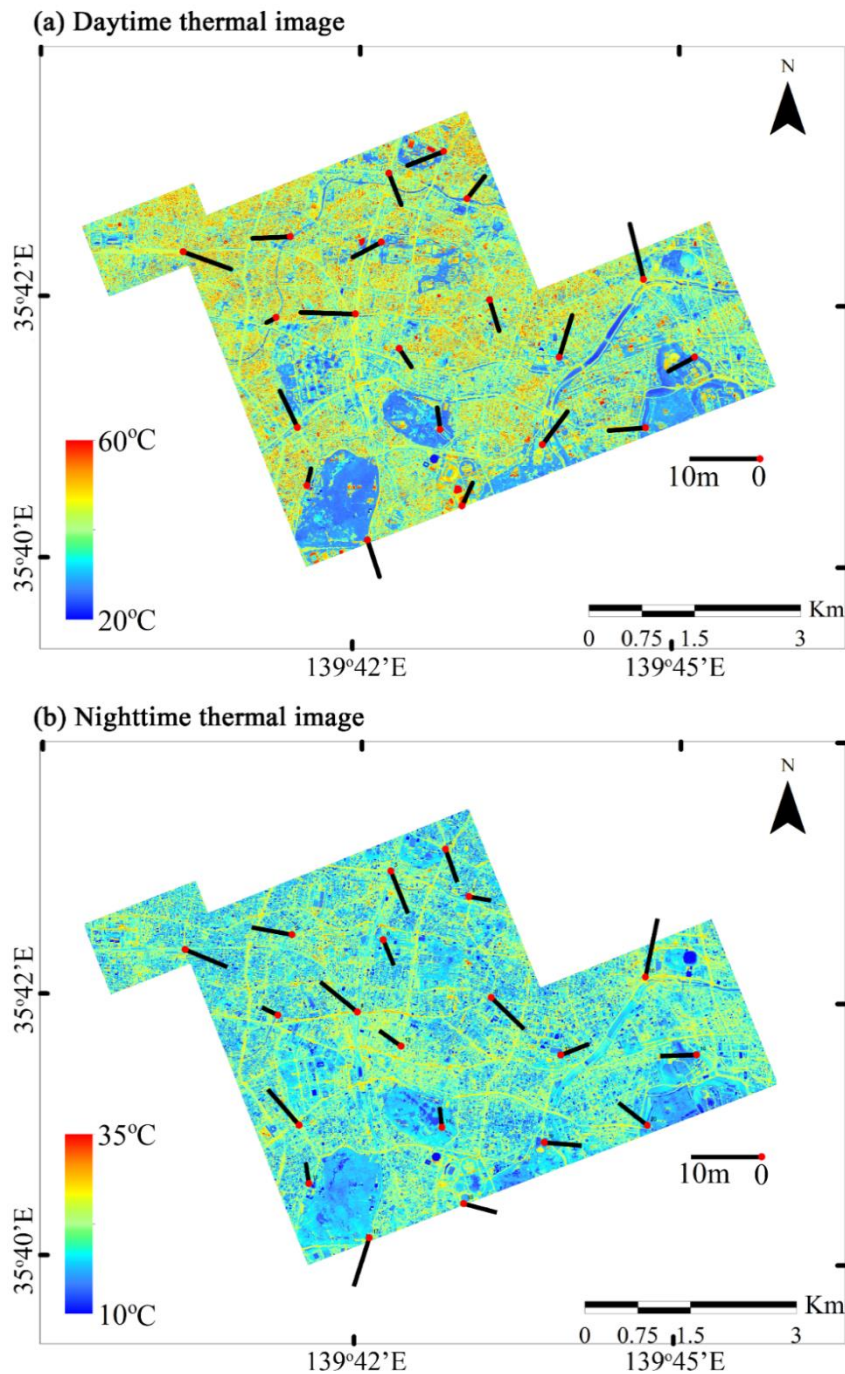


Figure 3-3: Images of error vector in manual georeferencing.

### 3.4 Accuracy Comparison

The error distance in Figure 3-1, 3-2, and 3-3 are summarized in Figure 3-4. The accuracy of LST image made by SfM thermal mosaicing in a large area is 4.22m (daytime) and 4.65m (night-time). While in small areas, their accuracy is about 2m. Considering the resolution of

the image is 2m, the accuracy is nearly the best.

The error distances of manual georeferencing in the large area are 5.05m (daytime) and 5.18m (night-time). The error distance of SfM thermal mosaicing is almost the same as that of manual georeferencing.



### 3.5 The Advantage of SfM Thermal Mosaicing

In SfM thermal mosaicing process in this study, no GCPs are used. But, even though there is no GCPs, we found that SfM thermal mosaicing was accurate to make the LST images (Figure 3-4).

In the case of manual georeferencing, it is difficult to use all the overlapped images because it is convenient to use fewer and less overlapped images to reduce the time for manual georeferencing process. In the SfM thermal mosaicing, overlapping of the images has a good effect in making an orthographic image.

### 3.6 Image Quality of Automatic Georeferencing Thermal Image

Images of SfM thermal mosaicing and manual georeferencing are compared in Figure 3-5. In the case of manual georeferencing, many sides (walls) of high buildings remain as the dark blue shadow in Figure 3-5b. While there is no reducing process of side building in manual georeferencing, the SfM thermal mosaicing can reduce the side of buildings, and the image becomes orthogonal as shown in Figure 3-5a. In the process of detection of corresponding points by SfM thermal mosaicing, the points in the original images are calculated as an orthogonal point cloud.

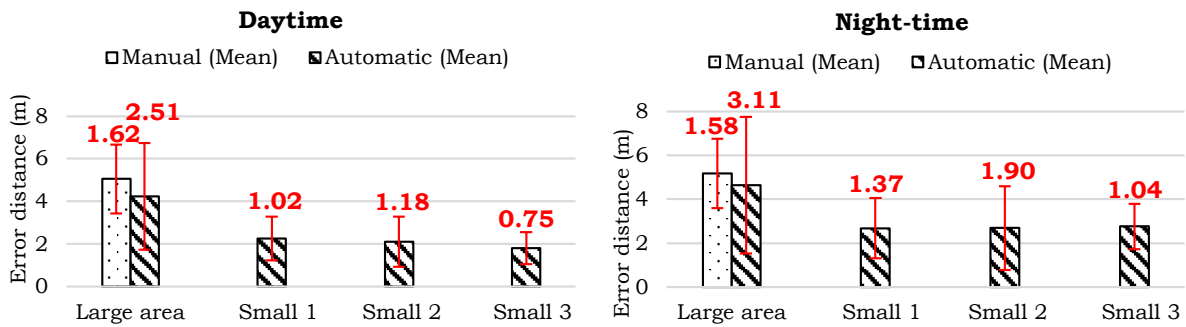


Figure 3-4: Mean and standard deviation of error distance.

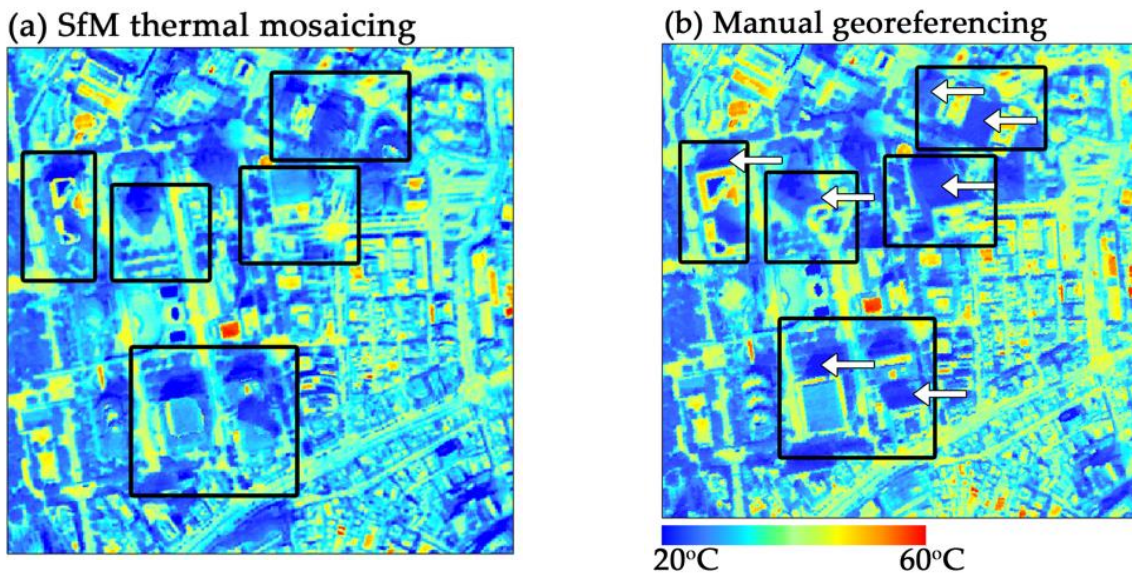


Figure 3-5: Comparison of SfM thermal mosaicing and manual georeferencing. Arrows show the side (wall) of the building.

#### 4 CONCLUSION

Based on the error distance analysis we conclude that it is possible to make the LST image effectively with high accuracy both in daytime and night-time by SfM thermal mosaicing. The accuracy in small areas was better than the large area. The mean error distance of small area was about 2m. Considering the resolution was 2m, the error was nearly the best. SfM thermal mosaicing also have an advantage in making orthogonal LST image.

The accurate method in this study will be a powerful tool for further environmental studies on the LST. In the future, the airborne LST measurement will become more practical and economical with SfM thermal mosaicing and with the progress of UAV or drone and the development of small thermal cameras.

#### ACKNOWLEDGEMENTS

This work was partly supported by Research Support of LIXIL JS Foundation.

#### REFERENCES

- Chen A., Yao XA, Sun R., Chen L., (2014), Effect of urban green patterns on surface urban cool islands and its seasonal variations. *Urban Forestry and Urban Greening*, 13(4), 646–654. doi.org/10.1016/j.ufug.2014.07.006
- Chesley JT, Leier AL, White S., Torres R., (2017), Using unmanned aerial vehicles and structure-from-motion photogrammetry to characterize sedimentary outcrops: An example from the Morrison Formation, Utah, USA. *Sedimentary Geology*, 354, 1–8. doi.org/10.1016/j.sedgeo.2017.03.013
- Colomina I., Molina P., (2014), ISPRS Journal of Photogrammetry and Remote Sensing Unmanned aerial systems for photogrammetry and remote sensing: A review. *ISPRS Journal of Photogrammetry and Remote Sensing*, 92, 79–97. doi.org/10.1016/j.isprsjprs.2014.02.013
- Connors JP, Galletti CS, Chow WTL, (2013), Landscape configuration and urban heat island effects: Assessing the relationship between landscape characteristics and land surface temperature in Phoenix, Arizona. *Landscape Ecology*, 28(2), 271–283. doi.org/10.1007/s10980-012-9833-1
- Dandois JP, Ellis EC, (2013), Remote Sensing of Environment High spatial resolution three-dimensional mapping of vegetation spectral dynamics using computer vision. *Remote Sensing of Environment*, 136, 259–276. doi.org/10.1016/j.rse.2013.04.005
- Darlington T., Odindi J., Dube T., Nyasha T., (2017), Remote Sensing Applications: Society and Environment Remote sensing applications in monitoring urban growth impacts on in-and- out door thermal conditions: A review. *Remote Sensing Applications: Society and Environment*, 8(August), 83–93. doi.org/10.1016/j.rsase.2017.08.001
- Dousset B., Gourmelon F., (2003), Satellite multi-sensor data analysis of urban surface temperatures and landcover. *ISPRS Journal of Photogrammetry and Remote Sensing*, 58(1–2), 43–54. doi.org/10.1016/S0924-2716(03)00016-9
- Estoque RC, Murayama Y., Myint SW, (2017), Effects of landscape composition and pattern on land surface temperature: An urban heat island study in the megacities of Southeast Asia. *Science of the Total Environment*, 577, 349–359. doi.org/10.1016/j.scitotenv.2016.10.195
- Honjo T., Tsunematsu N., Yokoyama H., (2017), Urban Climate Analysis of urban surface temperature change using structure-from-motion thermal mosaicing. *Urban Climate*. doi.org/10.1016/j.uclim.2017.04.004
- James MR, Robson S., Oleire-oltmanns S., Niethammer U., (2017), Geomorphology Optimising UAV topographic surveys processed with structure-from-motion: Ground control quality, quantity and bundle adjustment. *Geomorphology*, 280, 51–66. doi.org/10.1016/j.geomorph.2016.11.021
- Meesuk V., Vojinovic Z., Mynett AE, Abdullah AF, (2015), Urban flood modelling combining top-view LiDAR data with ground-view SfM observations. *Advances*

- in *Water Resources*, 75, 105–117.  
doi.org/10.1016/j.advwatres.2014.11.008
- Siebert S., Teizer J., (2014), Mobile 3D mapping for surveying earthwork projects using an Unmanned Aerial Vehicle (UAV) system. *Automation in Construction*, 41, 1–14.  
doi.org/10.1016/j.autcon.2014.01.004
- Streutker DR, (2002), A remote sensing study of the urban heat island of Houston, Texas. *International Journal of Remote Sensing*, 23 (March 2015), 2595–2608.  
doi.org/10.1080/01431160110115023
- Weng Q., Lu D., Schubring J., (2004), Estimation of land surface temperature-vegetation abundance relationship for urban heat island studies. *Remote Sensing of Environment*, 89(4), 467–483.  
doi.org/10.1016/j.rse.2003.11.005
- Westoby MJ, Brasington J., Glasser NF, Hambrey MJ, Reynolds JM, (2012), Geomorphology “Structure-from-Motion” photogrammetry: A low-cost , effective tool for geoscience applications. *Geomorphology*, 179, 300–314.  
doi.org/10.1016/j.geomorph.2012.08.021

# ANALYSIS OF ANTENNA SPECIFICATION FOR VERY HIGH RESOLUTION SATELLITE DATA ACQUISITION THROUGH DIRECT RECEIVING SYSTEM (DRS)

Muchammad Soleh<sup>1</sup>, Ali Syahputra Nasution, Arif Hidayat, Hidayat Gunawan, and Ayom Widipaminto

Remote Sensing Technology and Data Center

Indonesian National Institute of Aeronautics and Space

<sup>1</sup>E-mail: muchammad.soleh@lapan.go.id

Received: 6 November 2017; Revised: 21 December 2018; Approved: 29 December 2018

**Abstract.** Very High Resolution Satellite Image (VHRSI) data for Indonesian Government license is required by ministries/agencies, TNI, police, and local government to support national programs. But Indonesia did not have a VHRSI data recipient facility to directly acquire this data. In accordance with Law 21/2013 on Space, LAPAN is mandate to provide high resolution satellite data, and based on a roadmap for provision of satellite data in 2017, LAPAN will provide a VHRSI data reception facility through direct receiving system (DRS). This will be more efficient than other methods in providing the data. Priority provision of satellite data is for acquiring Pleiades and TerraSAR-X operating in the frequency range 8 GHz (X-Band). Therefore, to receive both data, it requires antenna subsystem with optimum coverage throughout Indonesia. Parameters to obtain the minimum antenna specifications include Free Space Loss (FSL), Carrier to Noise Ratio (C/No) and Antenna Gain to Noise Temperature (G/T). The calculation of G/T antenna is done for both satellites based on satellite parameters and analysis of antenna product availability in the market. Based on the calculation of satellite parameters shows that the minimum G/T value with the elevation of 5 degrees is 27.71 dB/K for Pleiades data reception and the minimum G/T value of 26.10 dB/K for the TerraSAR-X data reception. In general, the minimum G/T value for receiving the Pleiades and TerraSAR-X data is at 28 dB/K. While based on the calculation of antenna products availability in the market is require G/T value of 33.45 dB /K for the elevation of 5 degrees with a diameter of 7.5 mm antenna. This can be conclude that the antenna products meets the minimum requirements specification and to receive both satellite data. However, both calculation for the antenna subsystem still will be evaluated further in order to be directly installed at Parepare Remote Earth Station (SPBJ), South Sulawesi.

Keywords: *VHRSI, Optic, SAR, Direct Receiving System (DRS), Antenna*

## 1 INTRODUCTION

Recently, satellite data of Very High Resolution Satellite Image (VHRSI) with panchromatic channel at <1 meter, has been on a high demand for utilization and important due to support national priority activities, such as completion of the preparation of a Spatial Detail Plan (RDTR), mapping of Priority Industrial Estates (KIP) and Special Economic Zones (KEK) and mapping of border areas,

optimize planning and monitoring of urban/regional development. This in accordance with the Presidential Regulation of the Republic of Indonesia Number 79 of 2017 concerning Government Work Plans (RKP) and to support national program at providing large scale map (1:5,000). LAPAN and Geospatial Information Agency (BIG) are the Indonesian's government institutional that lead in supporting the program,

where LAPAN's responsibilities is mostly to provide VHRSI data.

Provision of data through procurement of VHRSI data at LAPAN has been carried out since January 2013 to October 2016. The VHRSI data includes Pleiades (70 cm), Quickbird (50 cm), GeoEye-1 (41 cm), Worldview-2 (46 cm) and Worldview-3 (31 cm) with cloud cover <20% in primary level and Geotiff (Airbus DS 2006; Digital Globe 2016). All VHRSI data before 2017 are archived in the National Remote Sensing Data Bank (BDPJN) with total coverage area at 998,835.21 km<sup>2</sup>, but requires more circa 923,734.79 km<sup>2</sup> in order to cover the entire Indonesian land area. Therefore, in order to fulfill the rest of the area it will requires 3 years to obtain the imagery circa 310,000 km<sup>2</sup>/year.

Indonesia as a tropical climate country causes the optical satellite data are largely constrained by clouds. For this reason, complementary data is needed such as SAR satellite data that can penetrate clouds and can be acquired at any time of day or night. Currently the infrastructure for providing the VHRSI and SAR data is not available at LAPAN. Based on current conditions, to prepare the VHRSI and SAR data acquisition

system, additional equipment is needed in the form of X-Band receiving antenna subsystem as shown in Figure 1-1.

The objective of this research is to carry out the preparation and operation of Direct Receiving System (DRS) to achieve the target number of high resolution optical VHRSI and SAR data.

## 2 ACQUISITION OF REMOTE SENSING SATELLITE DATA ON LAPAN GROUND STATION

Regarding the provision of satellite data through direct acquisition, LAPAN has already three ground stations system located in Parepare, Jakarta/Pekayon, and Rumpin. The ground station that is located in Parepare has 3 antenna system units and has been operating to carry out direct acquisition and processing of various satellite remote sensing data, such as Terra satellite data, Aqua, Suomi NPP, SPOT-6, SPOT-7, Landsat 7 and Landsat 8, while the ground station in Jakarta acquires and processes NOAA-18, NOAA-19, METOP-A, and Himawari-8 satellite data. The third ground station located in Rumpin acquires Terra, Aqua and Landsat 7 and Landsat 8 satellite data.

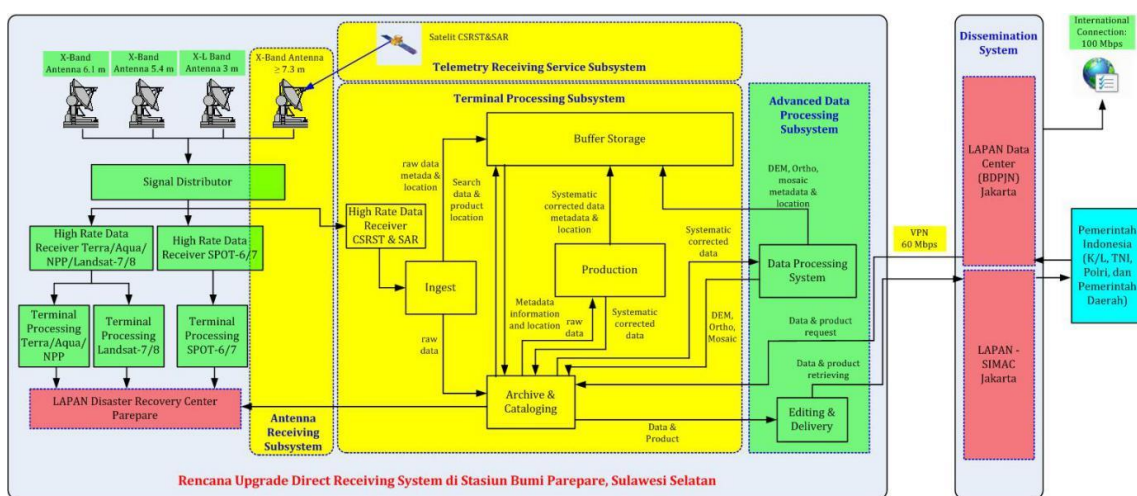


Figure 1-1: Current LAPAN Parepare Ground Station system architecture (green) and post reinforcement (yellow)



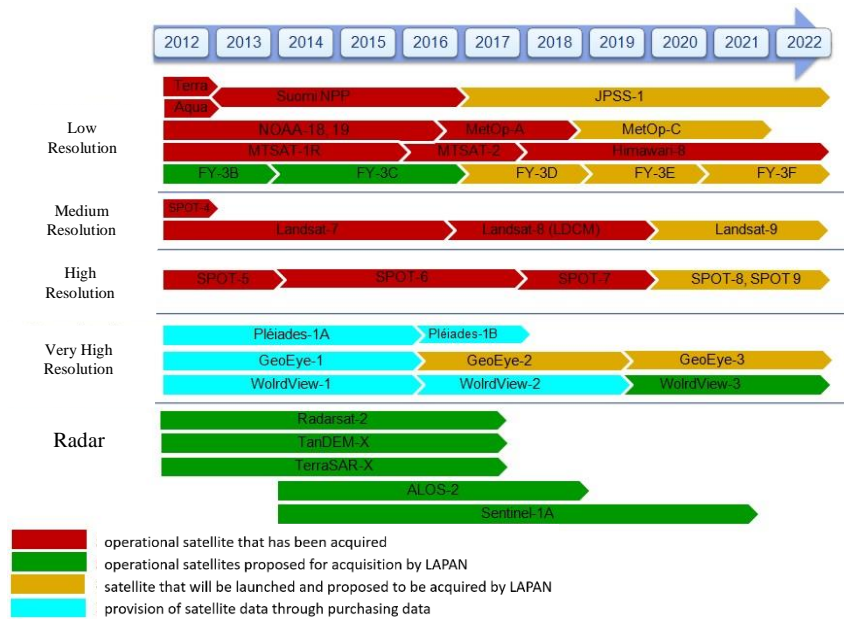


Figure 2-1: Plans for the acquisition of satellite remote sensing data by the LAPAN Ground Station until 2022

In early 2018, LAPAN Parepare ground station has planned to acquire VHRSI Optical data and high SAR resolution. The addition of a new antenna subsystem with X-Band frequency for receiving Pleiades optical satellite data and TerraSAR-X radar satellite data in order to meet the target number of optical VHRSI data area and high SAR resolution is shown in Figure 2-1.

**2.1 Efforts to Provide Pleiades and TerraSAR-X Data through Direct Receiving System (DRS)**

Pleiades satellite is one of the earth monitoring satellites with polar orbit which has a very high resolution of 0.5 m for panchromatic imagery and 2 m for multispectral imagery as shown in Figure 2-2. This Pleiades satellite is one of the constellation satellites operated by Airbus Defense and Space which has 4 spectral bands namely Panchromatic (480-830 nm), Blue (430-550 nm), Green (490-610 nm), Red (600- 720 nm), Near Infrared (750-950 nm) (Eoportal 2017). With the advantage of having a constellation satellite, the Pleiades Satellite can get data for an area everyday so that the process of

observing the area to be observed can run with maximum changes. This very useful for observing areas that are being affected by disaster and monitoring an area under construction. The Pleiades-1 Satellite and the Pleiades-2 Satellite are planned to be received in the Parepare Remote Sensing Ground Station.

The TerraSAR-X satellite is one of the radar satellites built by the German Aerospace Center (DLR) and EADS Astrium as shown in Figure 2-3. The TerraSAR-X satellite uses an active radar sensor onboard which the data is not interfere by the weather (Eoportal 2017).

The satellite has 3 imaging modes namely SpotLight, StripMap and ScanSAR. The SpotLight imaging mode has a spatial resolution of up to 1 m with the dimensions of the image in one portrait at 10 km (width) x 5 km (length). The StripMap imaging mode has a spatial resolution of up to 3 m with image dimensions 30 km (width) x 50 km (length), and the last TerraSAR-X Satellite has ScanSAR imaging mode, where the imaging mode has a resolution of up to 16 m with 100 km image dimensions (width) x 150 km (length) (Eoportal 2017).



The TerraSAR-X Satellite has been widely used for several applications such as mining, oil and gas exploration, topographic mapping, state defense and security, monitoring flood areas, earthquake prone areas, land use monitoring and others.

Provision of Pleiades and TerraSAR-X data above can be done with two alternatives, namely through purchasing/procurement for multi-users (limited licenses) and through direct acquisition/DRS (Direct Receiving System) which under the license of the Government of the Republic of Indonesia.

Provision of data through the procurement will be very limited to the availability of archived data acquired by satellite operators. In addition, the licenses given are usually limited, with a maximum of 10 users. Moreover, the provision for multi-users (limited licenses) will initially be cheaper and simpler when compared to direct data acquisition and no need to upgrade the antenna processing system at the earth station.

However, to meet all ministries/institutions and regional needs with limited license and to fulfill the rest of the target's coverage, it is necessary acquire the data through order programming the satellite, yet more expensive prices, with almost twice the price of archived data.

Comparing with the procurement in obtaining the data, in the long term, acquiring the data through DRS will be far more economical. In addition, user access for all ministries/institutions and local governments is not limited, because the license to use it is an Indonesian Government License.

The transmission from both satellite will sends a large data capacities at more than 300 Mbps. Therefore, to avoid damage to data when shipping, fading margins, it needs to be calculated so that the interference during transmission can be avoided.

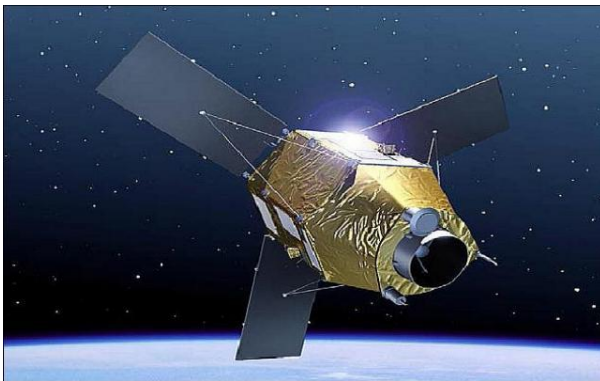


Figure 2-2: Pleiades-1/2 (Eoportal 2017)

**Product :** Panchromatic : 50 cm  
Multispectral : 2 m  
**Revisit rate :** Daily (constellation)  
**Spectral Bands :** Panchromatic (470 – 830 nm)  
Blue (430 – 550 nm)  
Green (500 – 620 nm)  
Red (590 – 710 nm)  
Near-infrared (740 – 940 nm)  
**Swath Width :** 20 Km  
**Processing Level :** Primary (1A)  
Ortho (automatic) or Tailored Ortho

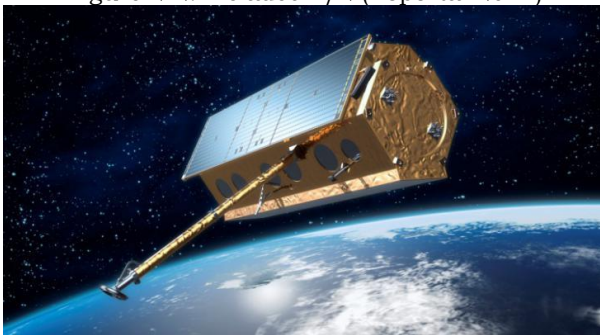


Figure 2-3: TerraSAR-X (Eoportal 2017)

**Product :** Staring SpotLight : up to 25 cm  
High Resolution Spot Light : up to 1 m  
StripMap : up to 3 m  
Scan SAR : up to 16 m  
Wide Scan SAR : up to 40 m  
**Revisit rate :** 11 days  
**Polarisation :** Single, dual - depending on imaging mode  
quadruple is available as advanced polarisation mode for dedicated acquisition campaigns

The other benefit of acquiring the data through programming order through DRS are the flexibility to obtain the VHRSI data in meeting high priority needs to cover all regions of Indonesia. Through direct data acquisition or DRS, the latest data can be obtain quickly according to priority. Another advantage of providing data with direct data acquisition is that it is flexible in producing multiple levels of data (bundle products and/or pansharpned products), better access services (emergency tasking, priority tasking, standard tasking and / or archive data), operational guarantee of acquisition by several satellites, wider data area compared to the purchase of archived data (for the same budget amount), and data licensed by the Government of the Republic of Indonesia.

The benefit of obtaining the SAR data is to be the complement of optical data due to ability to penetrate clouds.

In term of build the earth station system for direct reception (DRS) for VHRSI optical data and high resolution SAR, there are 3 main subsystems to be considered, namely the Telemetry Receiving Service Subsystem (TRSS), Antenna Receiving Subsystem (ARS) and Terminal Processing Subsystem (TPS).

This research is limited to reviewing and analyzing the Antenna Receiving Subsystem (ARS) subsystem which is planned to be implemented at LAPAN Parepare Ground Station through DRS for

receipt of Pleiades optical satellite data and TerraSAR-X radar satellite data. LAPAN Parepare Ground Station was chosen because of its location which is able to cover almost all parts of Indonesia.

As shown in Figure 2-4, the main components of the ARS subsystem for optical VHRSI data acquisition and high resolution SAR include several subsystems, namely the RF section consisting of X-Band, LNA and Feed-Power antennas and IF parts consisting of X-Band Down- Converter, Line Driver to Demodulator. All the systems must be able to be integrated with the antenna system that is already in LAPAN Parepare Ground Station.

## 2.2 High Resolution Satellite Parameters

Low earth satellite communication system has been using a single carrier communication system (Hidayat, 2006). Where sending data is sent in one channel, so that if there is damage then the data is not received properly. Single carrier transmission has a vulnerability to distortion interference due to interference or multipath signals. In addition, errors due to error pointing in tracking can be one of the causes of reception interference in the recipient (Hidayat et al. 2017; Hidayat 2014). We need a careful calculation so that the entire system can run according to needs.

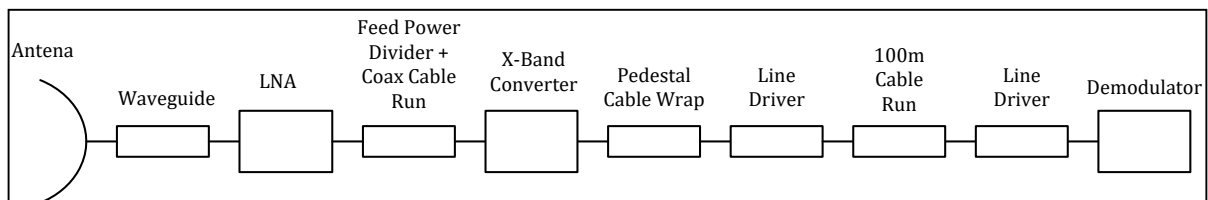


Figure 2-4: The main antenna system components on ARS (*Antenna Receiving Subsystem*)

To obtain the required G/T antenna parameters, a satellite EB/No value will be needed (Judianto, 2012). EB/No parameters can be seen in Figure 2-5a and b. The parameter value for Figure 2-5a is EB/No without coding gain while 2-5b uses error coding gain control, (Thales 2012). Error control coding functions as a control if there is damage or error bits of information received by the demodulator (Haykin 2007). Using error control coding can reduce the bit energy needed by satellite transmitters.

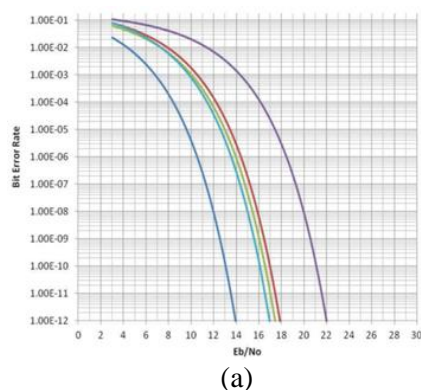
The use of error control reduces the number of bits of information transmitted because correction bits. According to Symon Haykin (2007), the bit rate value can be calculated with Equation:

$$\text{Data Rate} = \log_2(\text{Modulation}) * \text{Bandwidth} \quad (2-1)$$

However, when using the control bit, the calculation is multiplied by coding rate. Calculation of the value of data rates based on the coding value of 8 PSK gain multiplied by effective bandwidth multiplied by the coding gain factor (Hidayat 2006).

$$\text{Data Rate} = \text{Modulation} * \text{Bandwidth} * \text{Coding Rate} \quad (2-2)$$

The Pleiades satellite technical data can be seen in Table 2-1. Satellite Pleiades has 2 constellations, namely Pleiades 1 and Pleiades 2. Satellite Pleiades 1 and Pleiades 2 have 3 channel downlink, with



EIRP 15.3 dB at an altitude of 694 km with modulation of 8 PSK. The required EB/No value is 8.9 dB. From the satellite data, the value of the C/No system and G/T will be determined in the antenna demodulator. Following are the Pleiades satellite downlink parameters according to the Space Agency 2017 and Thales 2017.

The technical data of TerraSAR-X and Tandem-X satellites can be seen in Table 2-2. The TerraSAR-X satellite is a satellite made in Germany. This satellite has active SAR sensor capabilities. The downlink parameters of this satellite are shown in Table 2-2.

### 2.3 Geometry of Receiving Satellite Data and Power Requirements in Antenna Demodulators

The position of the satellite against the ground station antenna is depicted in Figure 2-6. Antenna elevation and satellite position on the antenna affect the distance of the satellite to the ground station. The lower the position of the antenna towards the horizon the further the position of the satellite is towards the ground station. The LEO satellite (Low Earth Orbit) moves quickly around the earth according to the speed of rotation. The distance between satellites and the earth varies very quickly. The tracking time is only 5 to 30 minutes depending on the antenna elevation to the horizon line.

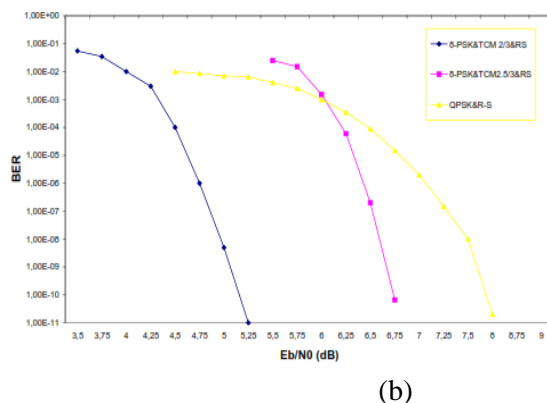


Figure 2-5: BER Graph against EB/No. (a) Without Error Control, (b) With Error Control 3/4 Trellis Code

Table 2-1: PLEIADES DOWNLINK PARAMETERS (UK SPACE AGENCIES, 2017)

No	Parameters	Pleaiades 1	Pleaiades 2
1	Apoge & Perigee	694 km	694 km
2	Inclination	98.3 Degree	98.3 Degree
3	Carrier Freq Ch 1	8165.5 MHz	8165.5 MHz
4	Carrier Freq Ch 2	8295.5 MHz	8295.5 MHz
5	Carrier Freq Ch 3	8353.5 MHz	8353.5 MHz
6	Bandwidth Ch1, Ch2, Ch3	105 MHz total 315 MHz	105 MHz total 315 MHz
7	EIRP ch 1,Ch2,Ch3	15.3 dB	15.3 dB
9	Modulation	8 PSK	8 PSK
10	BER	Min 10E-11	Min 10E-11
11	EB/No with Coding Gain	8.9 dB	8.9 dB
12	Data Rate at 8 PSK	155 Mbps Single Channel	155 Mbps Single Channel
13	Data Rate at 8 PSK	465 Mbps Full Channel	465 Mbps Full Channel

Table 2-2: TERRASAR-X AND TANDEM-X DOWNLINK PARAMETERS (UK SPACE AGENCY, 2017).

No	Parameters	TerraSAR X	Tandem X
1	Apoge & Perigee	514.8 km	514.8 km
2	Inclination	98.3 Degree	98.3 Degree
3	Carrier Freq	8150.0MHz	8150.0MHz
4	Bandwidth	225.0 MHz	225.0 MHz
5	EIRP	23dB	23dB
6	Modulation	QPSK	QPSK
7	BER	10 E-11	10 E-11
8	EB/No without coding gain	12 dB	12 Db
9	Bitrate	450 Mbps	450 Mbps

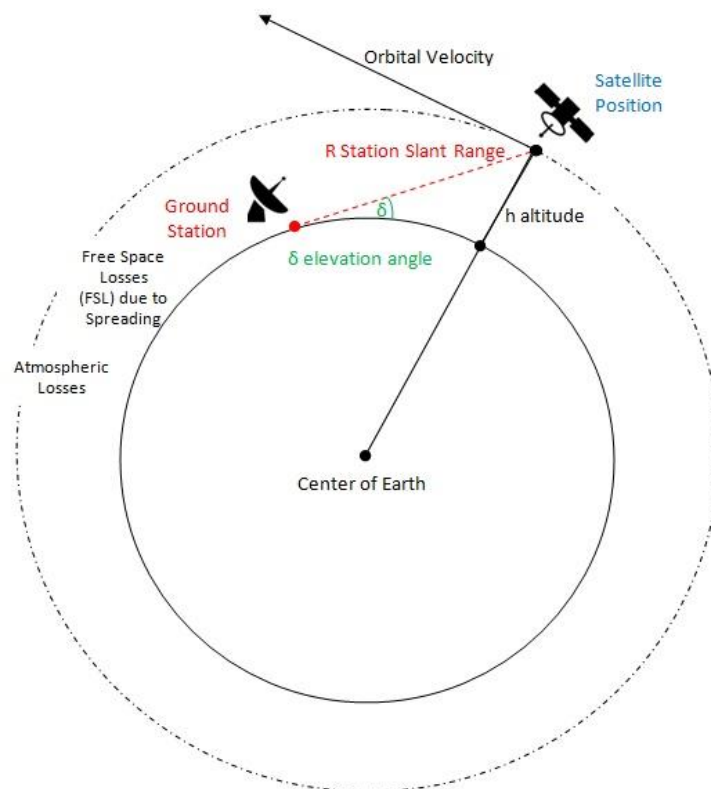


Figure 2-6: Illustration of Satellite Position on Earth Station Antennas

Calculation of the slant range distance from the highest elevation to the 5 degree elevation limit is done to obtain Free Space Losses (FSL) which will be used as C/No and G/T antenna calculations. The distance of the satellite with an antenna (RStation Slant Range) can be calculated based on the finger of the earth at the center of the earth with the satellite using equation 2-3 (Judianto, 2012).

$$R_{station\ slant\ range} = R_{earth} \left[ \sqrt{\frac{(h+R_{earth})^2}{R_{earth}^2} - \cos^2(\delta)} - \sin(\delta) \right] \quad (2-3)$$

where:

$R_{station\ slant\ range}$  = Distance from Satellite to Antenna (km)

$h$  = Altitude (km)

$R_{earth}$  = The radius of earth (km)

$\delta$  = Elevation Angle (degree)

To get the maximum distance, can be measured from the calculations of satellite geometry, where the maximum distance will be obtained when reaching 5 degrees elevation. According to Judianto (2012) the calculation of satellite distance to the earth station consists of several components, namely the distance of the satellite to the surface of the earth, the finger of the earth, the elevation angle of the antenna, the angle of the satellite with the center of the earth.

To measure the power lost in free space without obstacles, the FSL value is determined. FSL depends on two parameters, namely carrier signal frequency (f) and wireless transmission

distance (h). The FSL value is obtained from the following equation 2-4.

$$Free\ Space\ Losses\ (FSL) = 32.44 + 20\ log(h) + 20\ log(f) \quad (2-4)$$

where:

$FSL$  = Free Space Losses (dB)

$h$  = Altitude (km)

$f$  = Carrier Frequency (MHz)

The carrier value for Noise Ratio (C/No) in the receiving antenna is obtained by multiplying Energy per Bit to Noise Power Spectral Density Ratio (Eb/No) with a divided Bitrate (Rb) with Bandwidth (B) (Hidayat 2014). Mathematically C/No in the receiving antenna in the logarithmic form is stated in equation 2-5 (Judianto 2014):

$$\frac{C}{No} = \frac{Eb}{No} + Rb - B \quad (2-5)$$

where:

$\frac{C}{No}$  = Carrier to Noise Ratio (dB)

$\frac{Eb}{No}$  = Energy per Bit to Noise Power Spectral Density Ratio (dB)

$Rb$  = Bit Rate (dB)

$B$  = Bandwidth (dB)

The last parameter calculated is the value of antenna performance (G/T). G/T is a measure of the antenna's ability to obtain satellite data where G is an Antenna Gain and T is a System Noise Temperature, so G/T is the ratio of the Antenna Gain to System Noise Temperature. The relationship between C/No and G/T is expressed in the equation 2-6:

$$\frac{C}{No} = EIRP + \frac{G}{T} - FSL - L - K - B \quad (2-6)$$

The G/T value can be calculated as follows:

$$\frac{G}{T} = \frac{C}{No} - EIRP + FSL + K + B \quad (2-7)$$

where:

- G/T = Antenna gain-to-noise-temperature (dB)
- EIRP = *Effective (or Equivalent) Isotropic Radiated Power* (dbW)
- FSL = *Free Space Losses* (dB)
- K = *Boltzman Constant* (1.38064852(79) × 10<sup>-23</sup> J/K)
- B = *Bandwidth* (dB)
- L = *Loss Margin* (dB)

ARS Technical Needs for VHRSI Optical Data Acquisition and SAR High Resolution.

In general, the ARS technical requirements that will be applied in the LAPAN Parepare Ground Station are shown in Table 2-3.

The antennas operate on X-Band channels (8-12 GHz), minimum antenna diameter 7.3 m, polarisari RHCP/LHCP antenna (Right/Left Hand Circular Polarization), antennas are intended to be able to receive directly (DRS) data Pleiades and TerraSAR-X.

### 3 RESULTS AND DISCUSSION

#### 3.1 Analysis of Free Space Loss dan G/T Antenna

The results of calculation of *R<sub>station slant range</sub>* for Pleiades and TerraSAR-X are shown in Figure 3-1. *R<sub>station slant range</sub>* Indicates the distance of the satellite to the earth station antenna. The image is plotted using Equation 3. It can be seen that the distance at elevation is high, while the slant range for the two satellites tends to be closer to the satellite and both have similar value, which are for the Satellite Pleiades is 694 km and for TerraSAR-X is 514.8 km. While the calculation results at low elevation, the slant range distance for the two satellites tends to show far differences and the slant range between satellites and earth stations is very significant. The results are for Satellite Pleiades is ca. 3,055.23 km and for TerraSAR-X is ca. 2,613.79 km.

In this research, the author uses the antenna elevation reference value of 5 degrees, where for Pleiades *R<sub>station slant range</sub>* = 2,549.50 km and for TerraSAR-X *R<sub>station slant range</sub>* = 2,116.36 km.

The calculation of the value of the antenna elevation is used because the satellite transmission signal will begin to be captured by an antenna in a lock position at an elevation of 5 degrees. This also avoids the satellite transmission signal experiencing multipath fading and interference from the obstacle around the earth station at very low elevations (generally <3 degrees) (Hidayat, 2017).

Table 2-3: TECHNICAL NEEDS OF ANTENNA RECEIVING SUBSYSTEM (ARS)

Parameters	Specifications
Reflector Diameter	Minimum 7.3 m
Panel Material & Reflector Trusses	Aluminium
Feeder Type	Cassegraine
Tracking Ability	Program Track & Autotrack
Polarisation	
Data Channel	Simultaneous RHCP/LHCP
Tracking Channel	Selectable RHCP/LHCP
Frequency	X-band only
G/T	
Data Channel	Minimum 32.5 dB/K @ 5 degree elevation
Tracking Channel	Minimum 31.0 dB/K @ 5 degree elevation
Accuration	

Autotracking	Maximum 0.05° rms BRE
Pointing	Maximum 0.10° rms BRE
Insertion loss	Maximum 0.20 dB
Passband ripple	Maximum ± 0.05 dB
Axis Support	Az/EI/Train or Az/EI/Tilt
Position Accuration	0.025° rms
Center Frequency \IF	720 MHz (1200 MHz preferable)
Down Converter Availability (DC)	Minimum 3 units (Dual channel data reception, 1 channel tracking)
Up Converter Availability (UC)	Minimum 1 unit
Converter Type	Block/Modular
Temperature Outdoor	
Operational	-40°C to +55°C
Storage	-40°C to +65°C
Wind	
Operational	72 km/hr Gusting to 85 km/h
Survival	200 km/hr, sustained
Radome	Optional
Guaranteed availability of maintenance and spare parts	Minimum 10 years
Satellite Support	Could receive very high resolution optical satellite data such as Pleiades; and Radar satellite data such as TanDEM-X, TerraSAR-X
Can be integrated with existing LAPAN Parepare Ground Station devices	Mandatory

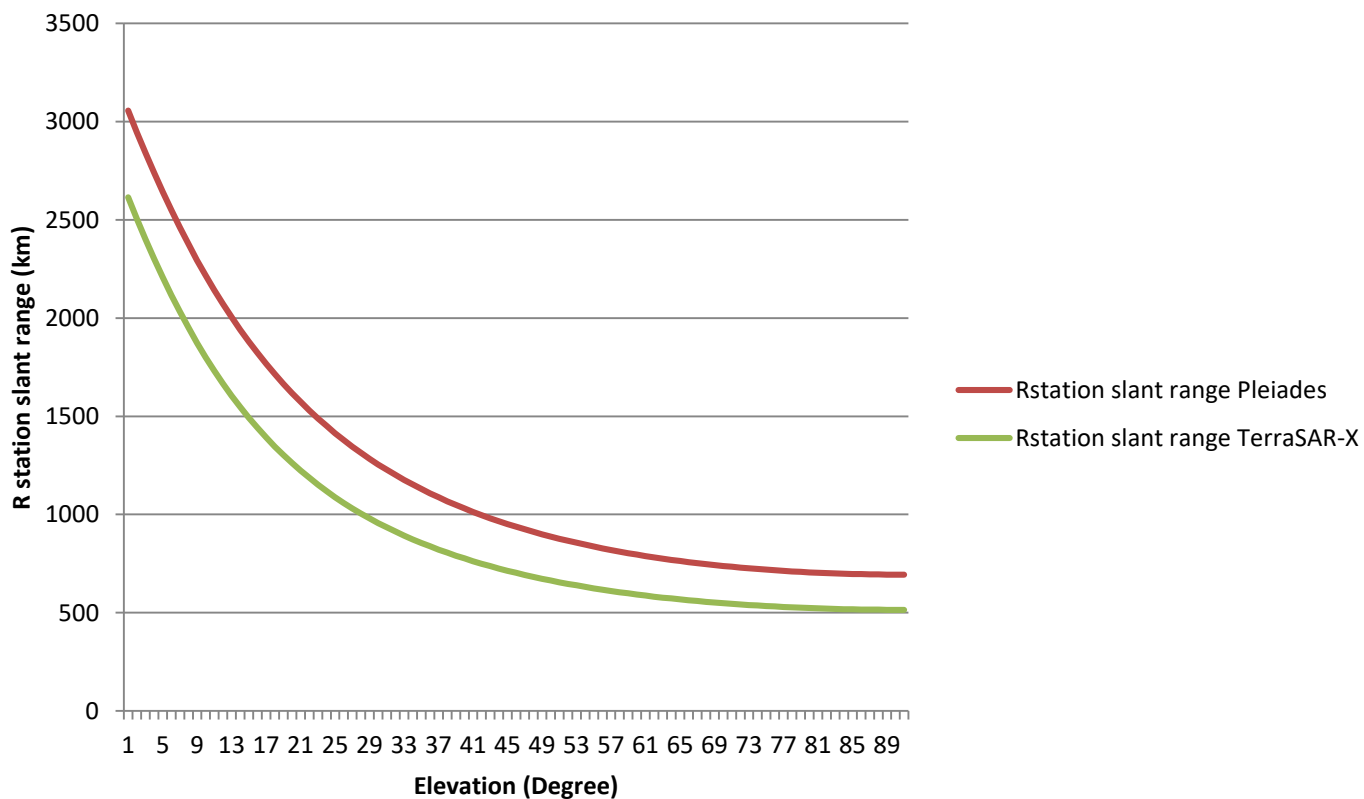


Figure 3-1: Distance of Pleiades and TerraSAR-X satellites to Earth Station Antennas



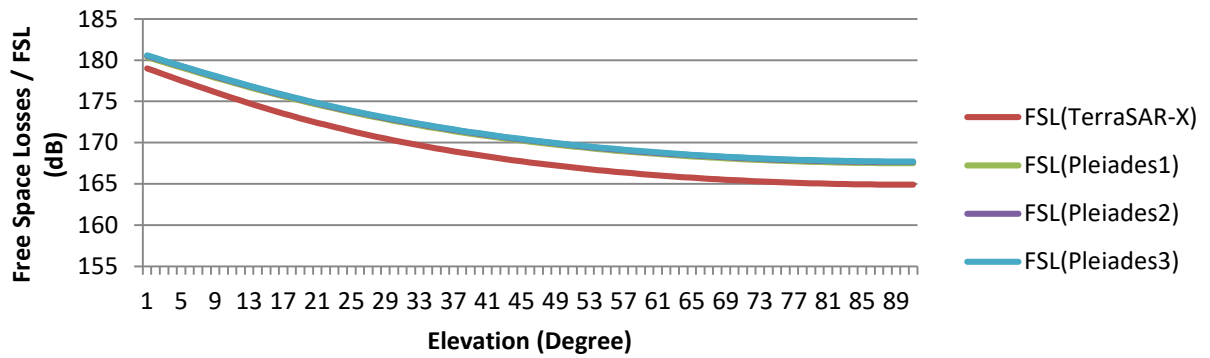


Figure 3-2: Free Space Loss (FSL) of Pleiades and TerraSAR-X Satellite

Table 3-1: Carrier to Noise Ratio (C/No) calculation values of Pleiades dan TerraSAR-X Satellite

No	Satellite	C/No (dB)
1	Pleiades	10.59
2	TerraSAR-X	15.01

Table 3-2: Parameters of Pleiades and TerraSAR-X Satellite Data Receipt at 5 Degrees Elevation

Downlink (Satellite to station)	Pleaides 1	Pleaides 2	Pleaides 3	TerraSAR-X	Unit
C/No Requirement di Demodulator	10.59	10.59	10.59	15.01	dB
EIRP	15.3	15.3	15.3	23.0	dBW
Loss Margin	2.0	2.0	2.0	2.0	dB
Bolzmant	228.6	228.6	228.6	228.6	dBW
Free Space Losses	178.81	178.95	179.00	177.17	dB
Bandwidth (B)	80.2118	80.2118	80.2118	83.5218	dB
G/T	26.10	26.53	27.14	27.71	dB

Electromagnetic waves emitted to the earth by the frequency of X-Band experience a loss of power due to vacuum and air. The power loss can be calculated based on the function of distance and frequency (Haykin, 2007). From the slant range distance parameters, the calculation can be derived to find the Free Space Losses (FSL) parameter values. The FSL calculation results are shown in Figure 3-2.

FSL values for TerraSAR-X appear to be lower than Pleiades, one of which is due to the TerraSAR-X slant range is smaller than the Pleiades. And based on its elevation, the FSL values of the two satellites will be greater at lower elevations and the smaller the FSL value at high

elevation. But at 5 degrees, the FSL Pleiades (1,2 and 3) and TerraSAR-X values are relatively similar, where the values are 178.81, 178.95, 179.00 and 177.17 dB, respectively.

Another parameter to calculate the antenna G/T requirement is the Carrier to Noise Ratio (C/No). C/No can be written as satellite transmit power plus reinforcement against noise minus loss minus the Boltzman constant and total Bandwidth in logarithmic form as shown in Equation 5. From the calculation results, it is shown in Table 3-1. The TerraSAR-X satellite has a C/No value greater than the Pleiades even though it uses QPSK modulation because it does not implement error control code.



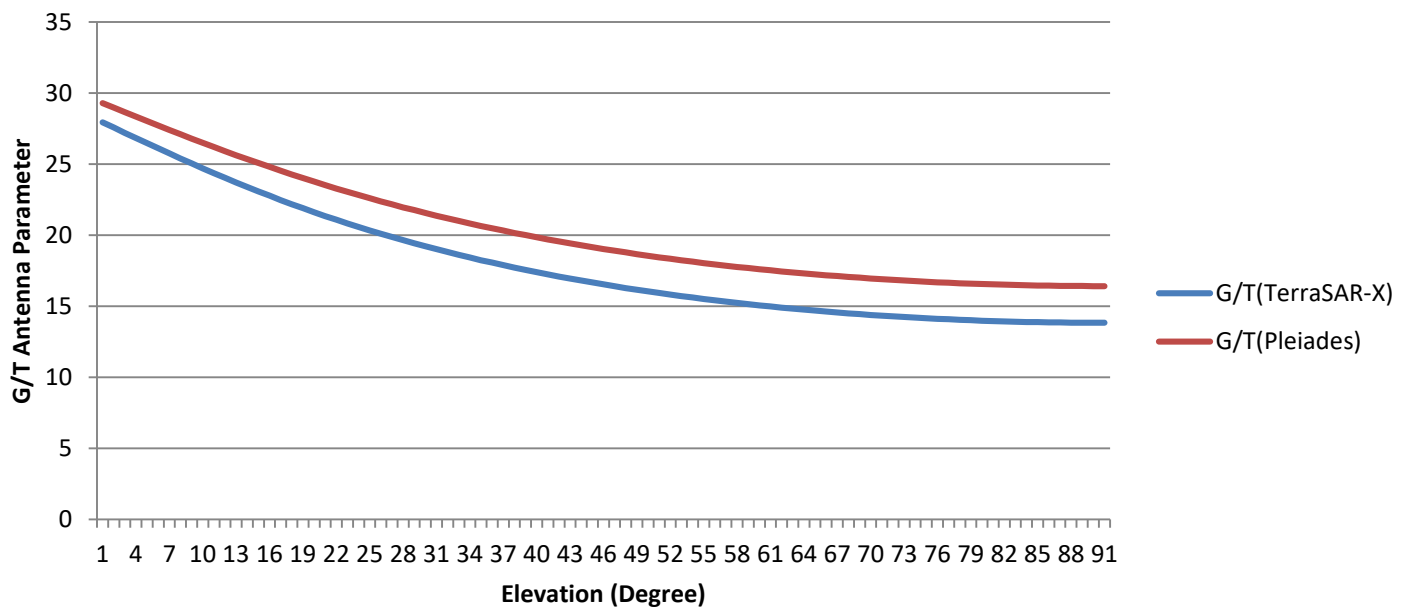


Figure 3-3: The Need for G/T Antenna for Every Elevation Based on Satellite Downlink Parameters

From result of calculation the FSL and C/No parameters, those value will be used to calculate the minimum G/T antenna requirements based on satellite downlink parameters that based on Tables 2-1 and 2-2 as shown in Figure 3-3.

All of the G/T values in Figure 3-3 above are expressed in logarithmic form derived based on satellite downlink parameters. According to R. Metzger (2011) and Klugel (2012) antennas used for data reception systems in Germany use an antenna with G/T 32 dB/K. In this section, the real demand for G/T will be calculated at the receiving antenna at the earth station based on previously calculated satellite parameters, namely C/No demodulator, FSL, Satellite EIRP, Bandwidth frequency and cable attenuation and connectors (Loss Margin) based on Equation 6. At an elevation of 5 degrees, the minimum requirement for G/T Pleiades is 26.10 dB/K and for TerraSAR-X is 27.71 dB/K. The results of G/T antenna calculations based on all satellite downlink parameters are summarized in Table 3-2.

### 3.2 Calculation of Requirements Analysis of G/T Antennas based on Availability of Antenna Products

Another calculation for determining the antenna G/T requirements for receiving VHRSI data is by reviewing it based on product specifications available on the market. Antenna input parameters that are taken into account include: antenna diameter, antenna efficiency, frequency, Sky Temperature, Waveguide, LNA, Power Divider Feed + Cable Run Coax, X-Band Converter, Pedestal Cable Wrap, Line Driver, 100m Cable Run and Demodulator. If the antenna diameter is 7.5 m with an efficiency of 71.72% and the signal frequency is 8 GHz, then the signal wavelength ( $\lambda$ ) transmitted is  $\lambda = \frac{c}{f} = 0.0375$  meters and Gain Antenna  $G = \frac{4\pi DF}{\lambda^2} \times efficiency$  amounting to 54.52 dBi. By calculating losses due to noise/temperature noise on the antenna system ( $T_{sys}$ ) of 21.06 dB/K, the antenna G/T value is obtained at 33.45 dB/K. Table 3-3 is a summary calculation to determine the G/T value of an antenna by considering several input parameters as mentioned above.

Table 3-3: CALCULATION OF G/T ANTENNAS BASED ON AVAILABILITY OF ANTENNA PRODUCTS IN THE MARKET

No	Parameters	Values	Units	No	Parameters	Values	Units
<b>Input Parameters :</b>				<b>Calculation Results (Output) :</b>			
1	Antenna Diameter	7,5	meter	1	Signal Wavelength	0,0375	meter
2	Antenna Efficiency	71,72	%	2	Antena Gain	283139,2	
3	Operating Frequency	8000	MHz	3	<b>Antena Gain Calculation Result</b>	<b>111</b>	
4	Antenna Sky Temperature	52,8	Kelvin	4	Noise Contribution From Antena	46,7341	Kelvin
5	Waveguide Temperature	290	Kelvin	5	Noise Contribution From Waveguide	33,3165	Kelvin
6	Waveguide Gain	-0,53	dB	6	Noise Contribution From LNA	45,0000	Kelvin
7	LNA Temperature	45	Kelvin	7	Noise Contribution From Coax Cable Run	0,0241	Kelvin
8	LNA Gain	45	dB	8	Noise Contribution From X-Band Converter	2,6115	Kelvin
9	Feed Power Divider + Coax Cable Run Temperature	290	Kelvin	9	Noise Contribution From Pedestal Cable Wrap	0,0096	Kelvin
10	Feed Power Divider + Coax Cable Run Gain	-5,6	dB	10	Noise Contribution From Line Driver	0,0443	Kelvin
11	X-Band Converter Temperature	290	Kelvin	11	Noise Contribution From 100m Cable Run	0,0002	Kelvin
12	X-Band Converter Gain	8	dB	12	Noise Contribution From Line Driver	0,0000	Kelvin
13	X-Band Converter Noise Figure	19	dB	13	Noise Contribution From Line Driver	0,0662	Kelvin
14	Pedestal Cable Wrap Temperature	290	Kelvin	14	<b>System Noise Temperature (T<sub>sys</sub>)</b>	<b>127,8066</b>	<b>Kelvin</b>
15	Pedestal Cable Wrap Gain	-4,5	dB	15	<b>System Noise Temperature (T<sub>sys</sub>)</b>	<b>21,0655</b>	<b>dB K</b>
16	Line Driver Wrap Temperature	290	Kelvin	16	<b>System G/T</b>	<b>33,4545</b>	<b>dB K</b>
17	Line Driver Gain	25	dB				
18	Line Driver Noise Figure	6	dB				
19	100m Cable Run Temperature	290	Kelvin				
20	100m Cable Run Gain	-6,5	dB				
21	Line Driver Temperature	290	Kelvin				
22	Line Driver Gain	0	dB				
23	Line Driver Noise Figure	0	dB				
24	Demodulator Temperature	290	Kelvin				
25	Demodulator Gain	0	dB				
26	Demodulator Noise Figure	25	dB				

The results of the calculation of G/T antenna requirements are carried out for both satellites based on satellite parameters and an analysis of the availability of antenna products on the market. From the satellite parameters obtained the calculation of the minimum G/T value at 5 degrees elevation of 27.71 dB/K for receipt of Pleiades data and the minimum G/T value of 26.10 dB/K for receiving TerraSAR-X data. Whereas based on the calculation of available antenna products on the market, the G/T value of 33.45 dB/K is obtained at 5 degrees elevation with a 7.5 meter antenna diameter. The analysis shows that the minimum G/T value for receiving Pleiades and TerraSAR-X data is 28 dB/K, and based on analysis of available antenna products on the market meet the minimum requirement specifications and allow them to receive data from both satellites with G/T values reaching 33 dB/K

at 5 degrees elevation if using an antenna with a diameter of 7.5 m. Therefore, it technically can be stated that the minimum requirement of G/T antenna to receive Pleiades and TerraSAR-X data is possible to be implemented in SPBJ Parepare. But the two results of these calculations need to be tested and evaluated directly for the X-Band antenna subsystem that will be planned to be installed at the Parepare Remote Sensing Ground Station, South Sulawesi.

Regarding the wiring and power problems on the X-Band antennas, the proposed is to build a new X-Band antenna with a diameter of 7.5 m at the LAPAN Parepare ground station which according to the results of the study is planned as shown in Figure 3-4, where the red line shows the cable line for power and the yellow line is the IF (Intermediate Frequency) cable line.

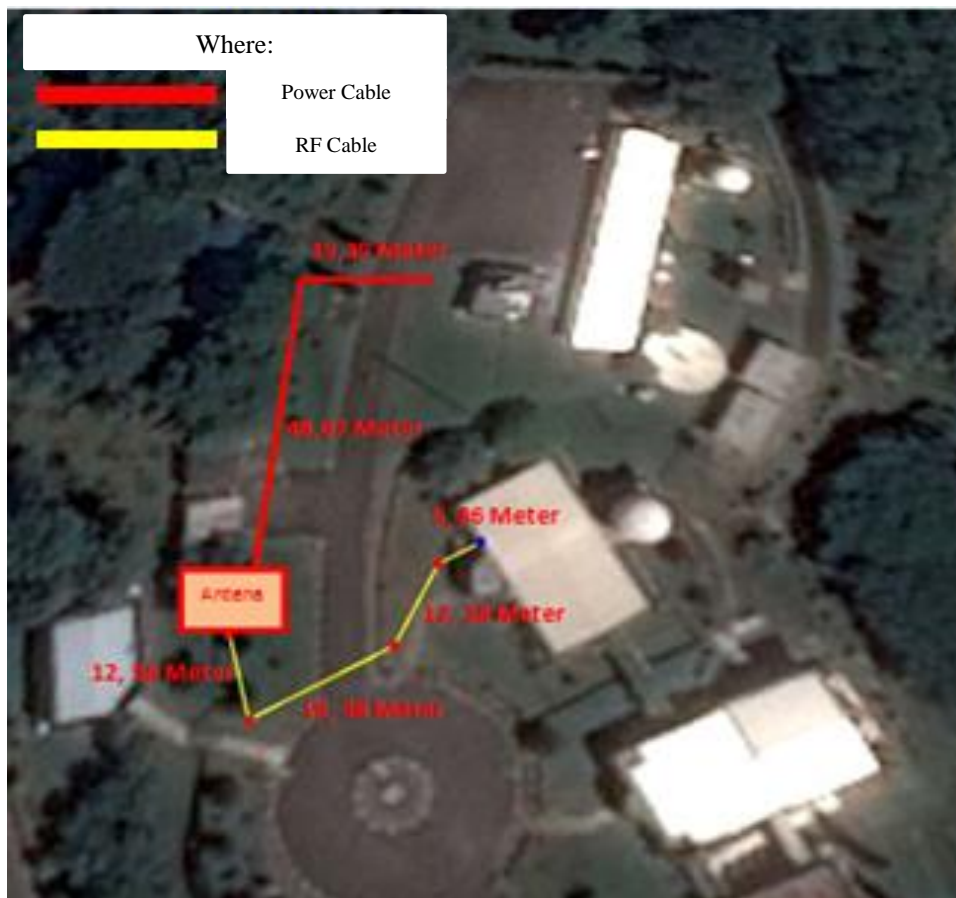


Figure 3-4: X-Band Antenna Allocation Plan For VHRSI Data Acquisition

#### 4 CONCLUSION

This study and analysis of the antenna subsystem is carried out for the reception of VHRSI optical data and direct high-resolution SAR (Direct Receiving System) data in order to meet the amount of data to support national priority programs. The benefit of acquiring the data through the DRS systems is to obtain the latest data of VHRSI (Pleiades) and SAR (TerraSAR-X) that can be provide quickly based on national priority. Another advantage of providing data with direct data acquisition is the flexibility in producing multiple levels of data (bundle products and/or pansharpened products), better access services (emergency tasking, priority tasking, standard tasking and / or archive data), operational guarantee of acquisition by several satellites, wider data area compared to the purchase of archived data (for the same amount of budget), and data with licenses from the Government of the Republic of Indonesia and the data provided can meet user needs in accordance with their priorities, while the advantages, in obtaining the Synthetic Aperture Radar (SAR) is for the complement of optical data due to ability to penetrate clouds.

Based on the measurement, in supporting the development of DRS for acquiring Pleiades and TerraSAR-X, some of the finding are to suggest that the new antenna will better has elevation reference value at 5 degrees due to a lock position types. This in order to avoids the satellite transmission signal experiencing multipath fading and interference from the obstacle around the earth station usually occurred at very low elevations (<3 degrees). The elevation reference at 5 degrees also will gives best FSL (relatively similar) for all the satellite (TerraSAR-X, Pleiades 1,2 and 3) which benefit to minimize the loss of power due to vacuum and air.

Moreover, based on the results of the calculation of G/T antenna requirements have been carried out for both satellites based on satellite parameters and an analysis of the availability of antenna products on the market, the satellite parameters obtained for the calculation of the minimum G/T value at 5 degrees elevation of 27.71 dB/K for receipt of Pleiades data and the minimum G/T value of 26.10 dB/K for receiving TerraSAR-X data. Whereas based on the calculation of available antenna products on the market, the G/T value of 33.45 dB/K is obtained at 5 degrees elevation with a 7.5 meter antenna diameter. The analysis shows that the minimum G/T value for receiving Pleiades and TerraSAR-X data is 28 dB/K, and based on analysis of available antenna products on the market meet the minimum requirement specifications and allow them to receive data from both satellites with G/T values reaching 33 dB/K at 5 degrees elevation if using an antenna with a diameter of 7.5 m. Therefore technically it can be stated that the minimum requirement of G/T antenna to receive Pleiades and TerraSAR-X data is possible to be implemented in Parepare Ground Station. But the two results of these calculations need to be tested and evaluated directly on the X-Band antenna subsystem which will be planned to be installed at the Parepare Ground Station, South Sulawesi.

Regarding the wiring and power problems needed to operate X-Band antennas, the proposed placement of a new X-Band antenna with a diameter of 7.5 m at the LAPAN Parepare Ground Station according to the results of the study is shown in Figure 3-4. Where the red line shows the cable line for power and the yellow line is the IF cable line.

## ACKNOWLEDGEMENT

The authors would like to thank LAPAN, especially the Head of Technology and Data Center LAPAN, Head of Programs and Facilities Division as well as the Acquisition Technology Research Group and LAPAN Remote Sensing Ground Station which provided input related to the study and plan for implementing the earth station system for receiving and recording remote sensing satellite data very high resolution optics and high resolution SAR.

## REFERENCES

- Airbus Inc., (2006), LAPAN Multi-Mission Direct Receiving Service Upgrade for High Resolution Optical & Radar Imagery.
- DigitalGlobe Inc., (2016), Imagery Intelligence on Command Direct Access Program & Imagery Solutions.
- Clinton E., et.al., (2017), Xband Communication. <http://propagation.ece.gatech.edu/ECE6390/project/Sum2015/team5/x-band-communication.html> Access on 15 September 2017.
- Eoportal, (2017), Pleiades-HR (High-Resolution Optical Imaging Constellation of CNES). <https://eoportal.org/web/eoportal/satellite-missions/p/pleiades>. Access on 15 September 2017.
- Eoportal, (2017), TSX (TerraSAR-X) Mission. <https://eoportal.org/web/eoportal/satellite-missions/p/pleiades>. Access on 15 September 2017.
- Haykin S., (2007), *Communication System 4 Edition*. John Wiley And Sons, New York.
- Hidayat A., et.al., (2014), Desain dan Implementasi Sistem Pakar Analisis Performansi Antena Seaspace Axyom 5.1 Berbasis Web. *Jurnal Teknologi Dirgantara*, 12 (20), 154-162.
- Hidayat A., et.al., (2014)., Analisis Carrier to Interference Transmisi Gelombang Mikrowave Link X Band dengan Downlink Satelit Penginderaan Jauh. Paper presented at the Seminar Nasional Inderaja:LAPAN, Bogor, Indonesia
- Hidayat A., et.al. (2014), *Calibration Directions Antenna Method Sun Pointing At Antena 3 Axis*, Paper presented at the Seminar Nasional Inderaja:LAPAN, Bogor, Indonesia.
- Hidayat A., Munawar, STA, Suprijanto, A., Setyasaputra, N., (2014), *Integration System for Receiving and Recording NPP Satellite Data at Remote Sensing Ground Station*. Paper presented at the Makassar International Conference on Electrical Engineering and Informatics (MICEEI) IEEE:UNHAS, 26-30 November 2014, Makassar, Indonesia.
- Hidayat A., Munawar STA, Syarif S., Andani A., (2017), *LEO Antenna Ground Station Analysis Using Fast Fourier Transform*, Paper presentend at The 7 th International Anual engineering Seminar (IEEE: UGM), 1-2 Agustus, Yogyakarta, Indonesia.
- Hidayat A., Ramadhan P.R., Suprijanto A., Munawar S.T.A., (2017), Kajian Kebutuhan Spesifikasi Antena Untuk Penerimaan Data Resolusi Sangat Tinggi. Paper presented at the Seminar Nasional Inderaja 2017:LAPAN, Depok, Indonesia.
- Hidayat A., (2006), Pemodelan Perencanaan Jaringan Wimax Untuk Daerah Urban dan Sub Urban. Tugas Akhir, Sekolah Tinggi Teknologi Telkom (STT Telkom) Bandung.
- Instruksi Presiden Nomor 6 Tahun 2012 tentang Penyediaan, Penggunaan, Pengendalian Kualitas, Pengolahan dan Distribusi Data Satelit Penginderaan Jauh Resolusi Tinggi.
- Integrasia SISS., (2017), *KOMPASAT Direct Receiving Station*".
- Judianto CT, (2012), Analisis Potensi Stasiun Bumi Sateli LAPAN-TUBSAT Kototabang Untuk Pengawasan Jalur Strategis Selat Malaka, *Jurnal Teknologi Dirgantara* Vol. 10 No. 1 Juni 2012 : 13-23
- KlÜgel T., et.al., (2014), Earth and space observation at the German Antarctic Receiving Station O'Higgins. electronic Publication Information Center, Alfred Wegener Institute for Polar and Marine Research (AWI), Bremerhaven, Germany.

Peraturan Presiden Republik Indonesia Nomor 79 tahun 2017 tentang Rencana Kerja Pemerintah (RKP) Tahun 2018.

Metzig R., Diedrich E., Reissig R., Schwinger M., Riffel F., Henniger H., Schättler B., (2011), *The tanDEM-X Ground Station Network*. Geoscience and Remote Sensing Symposium (IGARSS), 2011 IEEE International 24-29 July 2011, Vancouver, BC, Canada.

Setyasaputra N., Hidayat A., Hadiyanto AL, dan Munawar S.T.A., (2015), Analisis

Kebutuhan Integrasi Antena Orbital 3.0 dengan Sistem yang Telah Beroperasi di Stasiun Bumi Stasiun Bumi Penginderaan Jauh Parepare. Seminar Nasional Penginderaan Jauh (Sinasinderaja) 2015, IICC Bogor, Indonesia.

Thales, (2012), 8 PSK Data Downlink Subsystem. <https://www.thalesgroup.com/>. Access on 17 September 2017.

UK space Agency, (2017), Scfg X Band Database. <https://www.ofcom.org.uk>



# OBSERVING THE INUNDATED AREA USING LANDSAT-8 MULTITEMPORAL IMAGES AND DETERMINATION OF FLOOD-PRONE AREA IN BANDUNG BASIN

Fajar Yulianto<sup>1</sup>, Suwarsono, Sayidah Sulma, and Muhammad Rokhis Khomarudin

Remote Sensing Application Center

Indonesian National Institute of Aeronautics and Space (LAPAN)

<sup>1</sup>E-mail: fajar.yulianto@lapan.go.id

Received: 30 November 2018; Revised: 12 December 2018; Approved: 27 December 2018

**Abstract.** Flood is the most frequent hydro-meteorological disaster in Indonesia. Flood disasters in the Bandung basin result from increasing population density, especially in the Citarum riverbank area, accompanied by land use changes in upstream of the Citarum catchment area which has disrupted the river's function. One of the basic issues that need to be investigated is which areas of the Bandung basin are prone to flooding. This study offers an effective and efficient method of mapping flood-prone areas based on flood events that have occurred in the past through the use of historical remote sensing image data. In this research, Landsat-8 imagery was used to observe the inundated area in the Bandung basin in the past (2014–2018) using an improved algorithm, the modified normalized water index (MNDWI). The results of the study show that MNDWI is the appropriate parameter to be used to detect flooded areas in the Bandung basin area that have heterogeneous land surface conditions. The flood-prone area was determined based on flood events for 2014 to 2018, identified as inundated areas in the images. The estimation of the flood-prone area in the Bandung basin is 11,886.87 ha. Most of the flood-prone areas are in the subdistricts of Rancaekek, Bojongsoang, Solokan Jeruk, Ciparay, Cileunyi, Bale Endah and Cikancung. This area geographically or naturally is a water habitat area. Therefore, if the area will be used for residential, this will have consequences that flood will always be a threat to the area.

Keywords: *inundated area, flood-prone area, Bandung basin, Landsat-8, MNDWI*

## 1 INTRODUCTION

Flood is an overflow of river water caused by river discharge that exceeds the capacity of river channels in high rainfall conditions, or inundation that occurs in certain areas which are usually not stagnant (Kodoatie & Sugiyanto 2002). Flood is the most frequent hydro-meteorological disaster in Indonesia, especially in Java, and is often associated with deforestation in the upstream area of the watershed system (Harliani 2014). Flood disasters in the Citarum watershed often occur in its upper part, which comprises the Bandung basin area. The main problem that causes flooding in the Bandung basin is the increasing population

pressure and economic activity which has caused land use changes (Wangsaatmaja *et al.* 2006). Floods in the Bandung area cause economic and social losses. Such disasters occur when rainfall is high, and the water volume exceeds the capacity of the Citarum watershed (Darwin *et al.* 2018).

One of the basic issues that need to be investigated is which areas of the Bandung basin are prone to flooding. Understanding natural hazards is an important aspect for city planning and the implementations of policy and development. Understanding and awareness of the hazards will help improve planning for future city development (Raharjo 2017).



Almost all of the hazard and disaster data collected in the past presents many difficulties for analysis. This study offers an effective and efficient method of mapping flood-prone areas based on flood events that have occurred in the past by utilizing remote sensing image data.

Remote sensing shows important capabilities in mapping surface water objects and monitoring these dynamics. The design of the spectral water index is based on the fact that water objects will absorb energy at near-infrared (NIR) and short-wave (SWIR) wavelengths. The normalized water difference index (NDWI) has been used successfully to describe surface water features (Ji *et al.* 2009).

Gao (1996) developed an NDWI used for estimating water content of vegetation canopy. Gao's NDWI is calculated as the normalized difference of NIR and SWIR bands. Unlike Gao (1996), Rogers and Kearney (2004) used red and SWIR bands (bands 3 and 5 in Landsat TM) to produce NDWI. McFeeters (1996) developed the normalized difference water index (NDWI) based on Green and NIR channel. The NDWI value ranges from -1 to 1. McFeeters (1996) set zero as the threshold. Water is defined if  $NDWI > 0$  and it is non-water if  $NDWI \leq 0$ .

Furthermore, Xu (2006) found that McFeeters' NDWI was unable to completely separate built-up features from water features. NDWI showed positive values in built-up features which were similar to water because the NIR reflectance was lower than the green reflectance. Then, Xu (2006) proposed the modified NDWI (MNDWI), in which the SWIR band was used to replace the NIR band in McFeeters' NDWI formula. Same with McFeeters' NDWI, the threshold value for MNDWI was set to zero. By using this formula, it found a manual adjustment of the threshold

could achieve a more accurate result in the water mapping (Xu 2006).

The MNDWI can enhance open water features while efficiently suppressing and even removing built-up land noise as well as vegetation and soil noise. The improved algorithm has improved the ability to sharpen surface water objects, and in the context of these parameters can reduce interference from building objects, vegetation, and soil and is therefore very appropriate to be used to detect water objects that are associated with such land cover (Xu 2006).

The Bandung basin area has varied land cover conditions, most of which are forests, plantations, settlements, and agriculture (Narulita *et al.* 2008). There has been a massive conversion of agricultural land and plantations into built-up land (Nuraeni *et al.* 2017). By considering the condition of varied and dynamic land cover, the MNDWI method from Xu (2006) is a suitable method for inundation area mapping in Bandung basin.

## 2 MATERIALS AND METHODOLOGY

### 2.1 Location and data

Referred to Dam *et al.* (1996), the greater Bandung area is a large intermontane basin surrounded by volcanic highlands. The central Bandung plain is surrounded by Late Tertiary and Quaternary volcanic. North of Bandung, the Sunda-Tangkuban Perahu volcanic complex is located. The adjacent Lembang plain is bordered to the south by the conspicuous Lembang fault. The Citarum River with its tributaries forms the main drainage system of the Bandung basin catchment. It meanders through the center of the basin in a western direction and, after crossing several topographical barriers through narrow gorges, reaches the northern coastal lowlands. Deposits in the basin

comprise coarse volcanoclastic, fluvial sediments and notably a thick series of lacustrine deposits.

The research location is the part of the Bandung basin covered by Landsat-8 satellite path/row 122/065. The research sites are located in the Bandung City, Bandung Regency, and Sumedang Regency, West Java Province. Figure 2-1 shows the location of the study.

The data used are Landsat-8, path/row 122/065, with data acquisition times of:

- 9 June 2014
- 12 June 2015
- 6 January 2016
- 16 May 2017
- 6 July 2018

Landsat-8 data were obtained from the Remote Sensing Technology and Data Center of the Indonesian National Institute of Aeronautics and Space (LAPAN). The data format is GeoTIFF, and the level of the Landsat-8 data is the one terrain-corrected product (L1T). The L1T data is available to users as radiometric and geometrically corrected images. The level image is presented in units of Digital Numbers (DN) which can be easily rescaled to spectral radiance or top of atmosphere (TOA) reflectance (Zanter 2015).

Table 2-1: OLI spectral and spatial specification (Irons *et al.* 2012)

Bands	Bandwidth (µm)	GSD (m)
1	0.433 – 0.453	30
2	0.450 – 0.515	30
3	0.525 – 0.600	30
4	0.630 – 0.680	30
5	0.845 – 0.885	30
6	1.560 – 1.660	30
7	2.100 – 2.300	30
8	0.500 – 0.680	15
9	1.360 – 1.390	30

The Landsat 8 satellite is the latest generation of the Landsat satellite series from the NASA and the United States of Geological Survey (USGS) - Department of the Interior. It has advantages over its predecessors (Landsat 1, Landsat 2, Landsat 3, Landsat 4, Landsat 5, Landsat 6 (failed to reach orbit) and Landsat 7), in that it carries a charge sensor (the Operational Land Imager or OLI) which consists of nine spectral channels with a spatial resolution of 30 m (15 m for the panchromatic channel) and a thermal infrared sensor (TIRS) which measures land-surface temperature in two thermal bands with a 100 m spatial resolution (Irons *et al.* 2012).



(a)

Figure 2-1: Location of the study area of Bandung basin (red rectangle), coverage of Landsat-8 for path/row 122/065 (green rectangle). Map source: <http://landsat-catalog.lapan.go.id/>

Table 2-2: TIRS spectral bands and spatial resolution (Irons *et al.* 2012)

Bands	Center wavelength ( $\mu\text{m}$ )	Minimum lower band edge ( $\mu\text{m}$ )
10	10.9	10.6
11	12.0	11.5

## 2.3 Methods

### 2.3.1 Radiometric correction

The radiometric correction includes converting the DN data into a TOA reflectance (Zanter 2015). Then, the atmospheric correction is done by the DOS (Dark Object Subtraction) model (Chavez 1988; Chavez 1989).

### 2.3.2 Extraction of the MNDWI pixels

In this research, the inundated area of the Bandung basin was analyzed using Landsat-8 images based on the modified normalized water index (MNDWI), as developed by Xu (2006). The MNDWI can be expressed as follows:

$$MNDWI = (\rho_{\text{Green}} - \rho_{\text{MIR}}) / (\rho_{\text{Green}} + \rho_{\text{MIR}}) \quad (2-1)$$

Where  $\rho_{\text{MIR}}$  is the middle infrared reflectance value, and  $\rho_{\text{Green}}$  is the green reflectance value. Then, by using Landsat 8 data, the formula can be written as follows:

$$MNDWI = (\rho_3 - \rho_6) / (\rho_3 + \rho_6) \quad (2-2)$$

Where  $\rho_3$  is the reflectance value of band 3 and  $\rho_6$  is the reflectance value of band 6.

The obtained MNDWI images will show that water will have greater positive values than from the NDWI, built-up land will have negative values and soil and vegetation will also have negative values. So, the greater enhancement of water in the MNDWI image will result in more accurate extraction of open water features, because the built-up land, soil, and vegetation associated with them will have negative values (Xu 2006). Based on

the MNDWI equation, the pixels of the inundated area can be extracted with the following logical expression:

$$\text{IF } MNDWI_{ij} > 0 \text{ THEN } IA_{ij} \quad (2-3)$$

Where  $\rho MNDWI_{ij}$  is MNDWI value for specific row and column pixels.  $IA_{ij}$  is inundated area pixels for the specific rows and columns.

### 2.3.2 Flood-prone area determination

The flood-prone area was determined based on flood events for 2014 to 2018, identified as inundated areas in the images. Flood-prone areas (FPA), (as raster polygon) were determined as a union (U) of all raster polygons of inundated areas (IA) as follows:

$$FPA = IA_{t1} \cup IA_{t2} \cup IA_{t3} \cup IA_{t4} \cup IA_{t5} \quad (2-4)$$

Where  $IA_{t1}$ ,  $IA_{t2}$ ,  $IA_{t3}$ ,  $IA_{t4}$ , and  $IA_{t5}$  are Pixels of Inundated Area derived from Landsat-8 date acquisition of 9 June 2014, 12 June 2015, 6 January 2016, 16 May 2017, and 6 July 2018 consecutively.

## 3 RESULTS AND DISCUSSION

### 3.1 Inundated areas identified visually from Landsat-8

Inundated areas can be identified visually from Landsat-8 composite false color RGB 654 images. In the images, water is indicated by bluish colours, vegetation by greenish colours and built-up objects by reddish colours. Figure 3-1 shows the inundated areas seen visually from Landsat-8 composite false color RGB 654 images of the Bandung basin. The events are for 9 June 2014, 12 June 2015, 6 January 2016, 16 May 2017 and 6 July 2018. Based on the description of some of these images, it can be seen that the most severe flooding occurred on 6 January 2016.

**3.2 Inundated areas extracted from Landsat-8 imagery based on MNDWI**

Inundated areas were extracted from Landsat-8 imagery based on the MNDWI parameter (Equations 2 and 3) for all images. The results (raster polygons of inundated areas) can be seen in Figure 3-2. The spread of the spatial distribution of the inundated area varies from year to year (Table 3-1). Based on the images, the most severe flooding, with an area of 11,116 hectares, occurred on 6 January 2016.

**3.3 Determination of flood-prone area**

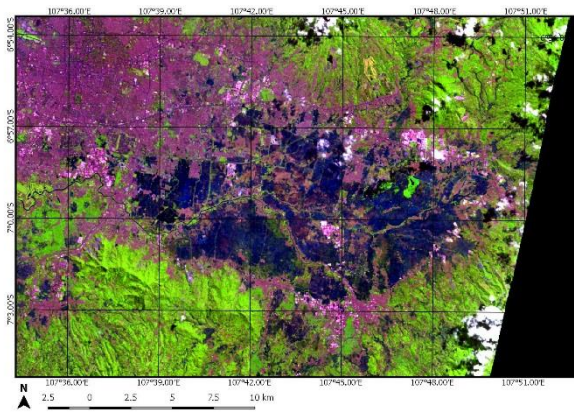
Figure 3-5 shows the flood-prone area of the Bandung basin, the result of the union of several inundated area raster polygons. The estimation of the extent of flood-prone areas in the

Bandung basin is 11,886.87 hectares. This area covers three districts: Bandung City, Bandung, and Sumedang. Most of the flood-prone areas are in the subdistricts of Rancaekek, Bojongsoang, Solokan Jeruk, Ciparay, Cileunyi, Bale Endah, and Cikancung. Based on spatial distribution and area, these six subdistricts were the most severely affected by the flood. When an outline is drawn which limits the flood-prone areas, it forms a kind of 'bowl'. Noting the topographic conditions, it can be seen that the bowl area is a concentration area of water flow originating from the north, south, west and east slopes. The area geographically or naturally is a water habitat area. Therefore, if the area will be used for residential, this will have consequences that flood will always be a threat to the area.

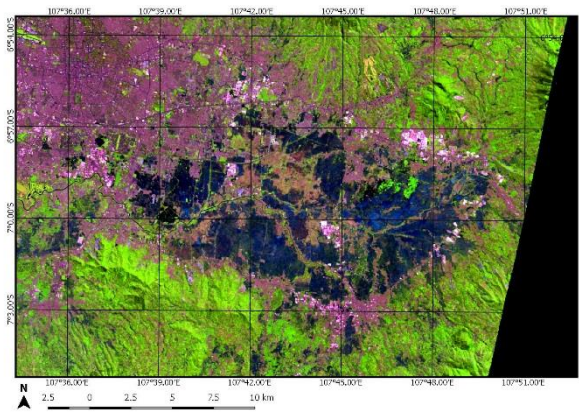
Table 3-1: The spread of inundated area spatial distribution

Date	Inundated areas (hectares)
9 June 2014	5,089
12 June 2015	4,772
6 January 2016	11,116
16 May 2017	3,822
6 July 2018	3,631

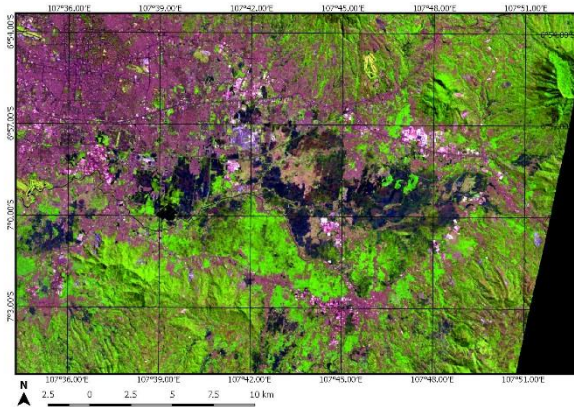




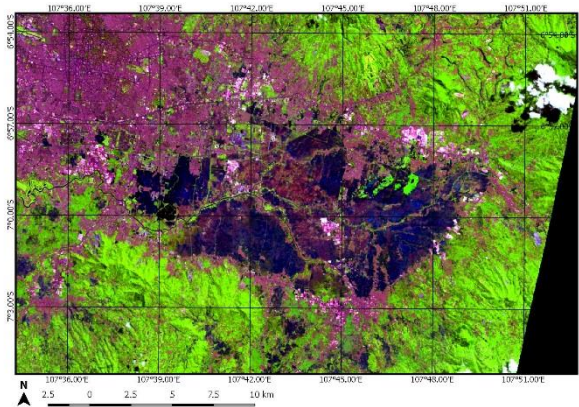
9 June 2014



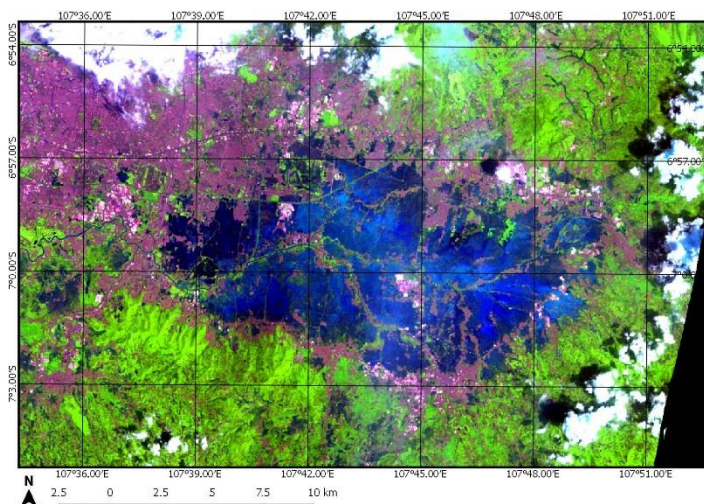
12 June 2015



6 July 2018



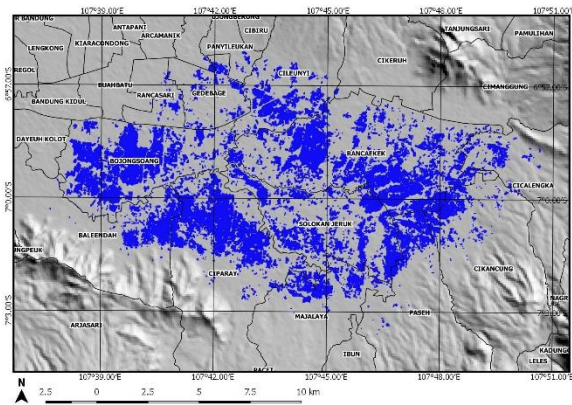
16 May 2017



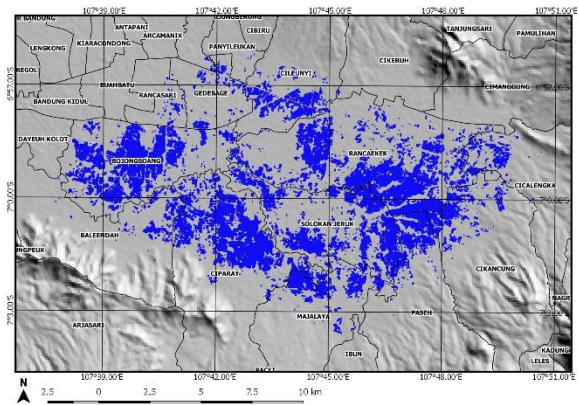
6 January 2016

Figure 3-1: Inundated areas (shown in blue) seen visually from Landsat-8 composite false color RGB 654 images of the Bandung basin

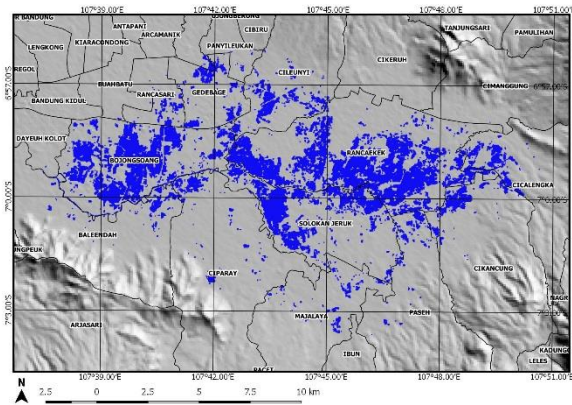




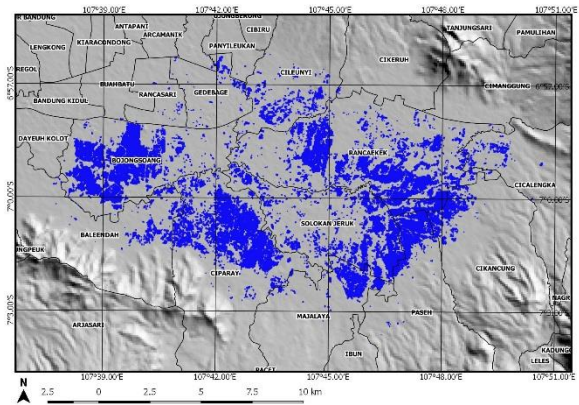
9 June 2014 (5,089 hectares)



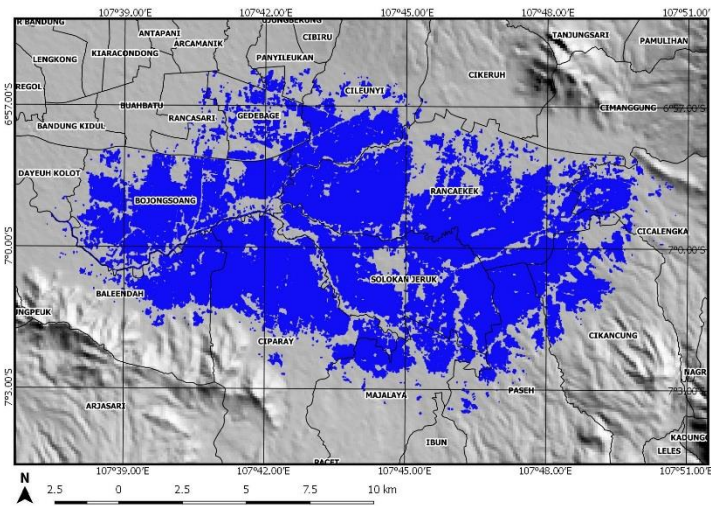
12 June 2015 (4,772 hectares)



6 July 2018 (3,631 hectares)



16 May 2017 (3,822 hectares)



6 January 2016 (11,116 hectares)

Figure 3-2: Inundated areas of the Bandung basin (shown in blue) extracted from Landsat-8 images, based on MNDWI, were compiled above the SRTM30 DEM.

Table 3-2: Distribution of flood-prone areas based on administrative boundaries

Subdistrict	District	Area (ha)	Area %
Rancaekek	Bandung	2,944.04	24.77
Bojongsoang	Bandung	1,736.93	14.61
Solokan Jeruk	Bandung	1,723.37	14.50
Ciparay	Bandung	1,708.53	14.37
Cileunyi	Bandung	685.59	5.77
Bale Endah	Bandung	652.69	5.49
Cikancung	Bandung	633.40	5.33
Paseh	Bandung	547.73	4.61
Majalaya	Bandung	481.20	4.05
Gedebage	Bandung City	355.17	2.99
Cicalengka	Bandung	303.09	2.55
Rancasari	Bandung City	70.10	0.59
Panyileukan	Bandung City	19.17	0.16
Cinambo	Bandung City	14.23	0.12
Cikeruh	Sumedang	5.73	0.05
Dayeuh Kolot	Bandung	3.05	0.03
Cimanggung	Sumedang	1.84	0.02
Buahbatu	Bandung City	1.02	0.01
<b>Total area</b>		<b>11,886.87</b>	<b>100.00</b>

### 3.4 Verification

Verification of the results of the analysis was carried out through field surveys. As many as 30 location points, based on image analysis of flood-prone areas, were chosen by purposive sampling. The ground checks were conducted between 6 and 12 August 2018. Figure 3-3 showed the point locations of ground checks. Figure 3-4 showed the examples of the field condition of flood-prone areas in floodplains. We found that 28 locations are Floodplains, 1 location is Ox-Bow Lake, and 1 location is River Course.

Based on geomorphological point of view, Floodplain, Ox-Bow Lake and River Course are flood-prone areas.

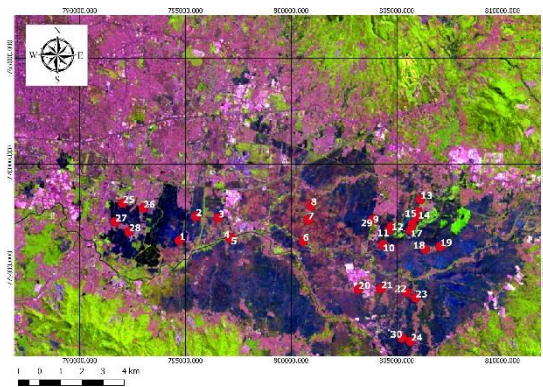


Figure 3-3: The point locations of ground checking (red dots)



Location 17: 06.98489° S / 107.75792° E



Location 19: 06.97846° S / 107.76930° E



Location 22: 06.98629° S / 107.76608° E

Figure 3-4: Examples of the field condition of flood-prone areas in floodplains



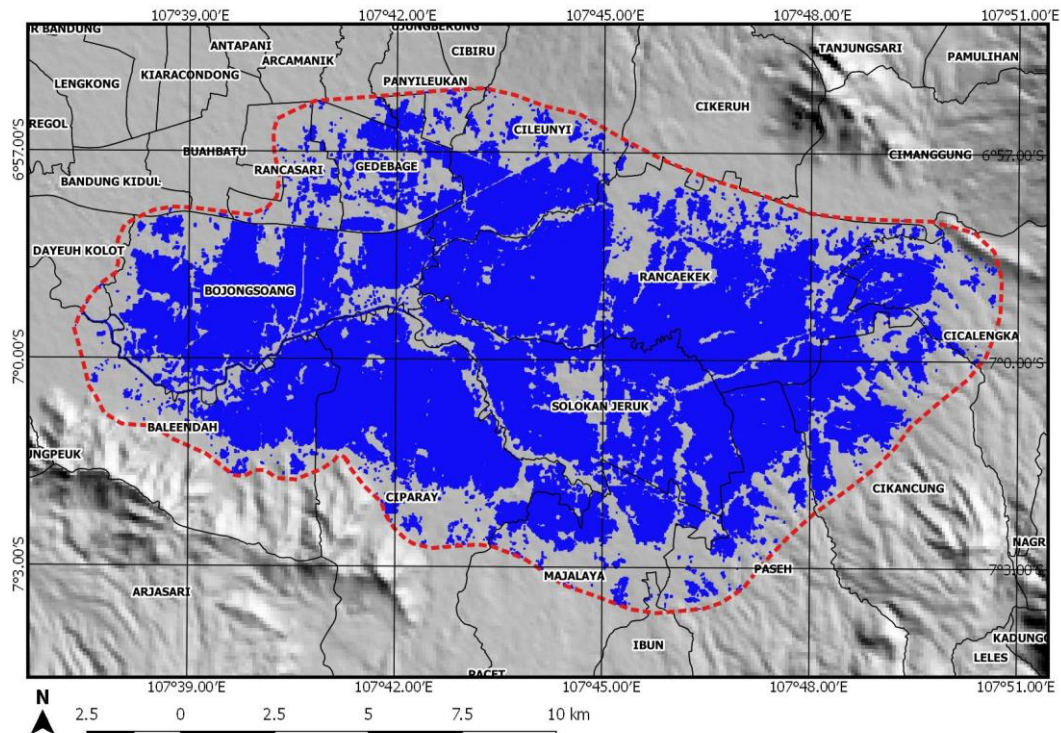


Figure 3-5: Flood-prone area (in blue) in the Bandung basin, compiled above the SRTM30 DEM. The red polyline indicates the outer boundary of the flood-prone area.

We also tried to compare the flood-prone areas with the flood vulnerability map in the Bandung basin resulting from the research of Darwin *et al.* (2018). Darwin *et al.* (2018) tried to compose a flood vulnerability map in the Bandung basin using the Chi-square Automatic Interaction Detection (CHAID) method. The comparison results show that both have a similar pattern, where the flood-prone area produced is included in the high and moderate hazard classes in the flood vulnerability map composed by Darwin *et al.* (2018).

#### 4 CONCLUSION

MNDWI is the appropriate parameter to be used to detect flooded areas in the Bandung basin area that have heterogeneous land-surface conditions. The flood-prone area map can be composed based on flood events, identified as inundated areas in the Landsat-8 images. The estimation of the flood-prone area in the Bandung basin is 11,886.87 ha. Most of the flood-prone areas are in the subdistricts of

Rancaekek, Bojongsoang, Solokan Jeruk, Ciparay, Cileunyi, Bale Endah, and Cikancung. The area geographically or naturally is a water habitat area. Therefore, if the area will be used for residential, this will have consequences that flood will always be a threat to the area. Further research is needed to classify flood-prone area by using more image data representing seasonal conditions.

#### ACKNOWLEDGEMENTS

This paper is a part of the research activities entitled 'The utilization of remote sensing data for disaster mitigation in Indonesia'. This research was funded by the Program of National Innovation System Research Incentive (INSINAS) in 2018, Ministry of Research Technology and Higher Education, Republic of Indonesia. Thank Dr. Dony Kushardono as the group leader in this activity. SRTM30 DEM was provided by the U.S. Geological Survey (USGS) and Landsat 8 OLI/TIRS was provided by Remote Sensing Technology and Data



Center, LAPAN. We thank the Statistics Service Unit, Ministry of Communication and Information-West Java Province, and Regional Disaster Management Agency (BPBD) West Java Province for discussions and collaborations to support this research.

## REFERENCES

- Chavez Jr. PS, (1988), An improved dark-object subtraction technique for atmospheric scattering correction of multispectral data. *Remote Sensing of Environment* 24:459-79.
- Chavez Jr. PS, (1989), Radiometric Calibration of Landsat Thematic Mapper Multispectral Images. *Photogrammetric Engineering and Remote Sensing* 55(9):1285-1294.
- Dam MAC, Suparan P., Nossin JJ, Voskuil, RPGA and GTL Group, (1996), A chronology for geomorphological developments in the greater Bandung area, West-Java, Indonesia. *Journal of Southeast Asian Earth Sciences* 14 Nos 1/2:101-115.
- Darwin, Kombaitan B., Yudoko G., and Purboyo, H., (2018), Application of GIS on determination of flood prone areas and critical arterial road network by using CHAID method in bandung area. *MATEC Web of Conferences* 147: No. 02007, 11 pages.
- Gao BC, (1996), NDWI a normalized difference water index for remote sensing of vegetation liquid water from space. *Remote Sensing of Environment* 58:257-266.
- Harliani, F., (2014), Persepsi Masyarakat Kampung Cieunteung, Kabupaten Bandung tentang Rencana Relokasi Akibat Bencana Banjir. *Jurnal Perencanaan Wilayah dan Kota* 25(1):37-57.
- Irons JR, Dwyer JL, Barsi JA, (2012), The next Landsat satellite: The Landsat Data Continuity Mission. *Remote Sensing of Environment* 122:11-21.
- Ji L., Zhang L., and Wylie, (2009), Analysis of Dynamic Thresholds for the Normalized Difference Water Index. *Photogrammetric Engineering & Remote Sensing* (75)11:1307-1317.
- Kodoatie R., and Sugiyanto, (2002), *Banjir: Beberapa Penyebab dan Metoda Pengendaliannya dalam Perspektif Lingkungan*. Yogyakarta: Pustaka Belajar.
- McFeeters SK, (1996), The use of normalized difference water index (NDWI) in the delineation of open water features. *International Journal of Remote Sensing*, 17:1425-1432.
- Narulita I., Rahmat A., and Maria R., (2008), Aplikasi Sistem Informasi Geografi untuk Menentukan Daerah Prioritas Rehabilitasi di Cekungan Bandung. *Jurnal Riset Geologi dan Pertambangan* 18(1): 23-35.
- Nuraeni R., Sitorus SRP, and Panuju DR, (2017), Analisis Perubahan Penggunaan Lahan dan Arah Penggunaan Lahan Wilayah di Kabupaten Bandung. *Buletin Tanah dan Lahan*, 1(1): 79-85
- Raharjo PP, (2017), Understanding and Identifying Natural Hazard for Bandung City Preparedness and Mitigation against Natural Disaster. *MATEC Web of Conferences* 103: No. 07011, 6 pages.
- Rogers AS, and Kearney MS, (2004), Reducing signature variability in unmixing coastal marsh Thematic Mapper scenes using spectral indices. *International Journal of Remote Sensing*, 25(12): 2317-2335.
- Wangsaatmaja S., Sabar A., and Prasetiati, MAN, (2006), Permasalahan dan Strategi Pembangunan Lingkungan Berkelanjutan, Studi Kasus: Cekungan Bandung. *Jurnal Geologi Indonesia* 1(3): 163-171.
- Xu H., (2006), Modification of normalised difference water index (NDWI) to enhance open water features in remotely sensed imagery. *International Journal of Remote Sensing* 27(14): 3025-3033.
- Zanter K. (Ed)., (2015), *Landsat 8 (L8) Data Users Handbook, Version 1*. Sioux Falls, South Dakota: Department of the Interior, U.S. Geological Survey.

# MANGROVE FOREST CHANGE IN NUSA PENIDA MARINE PROTECTED AREA, BALI - INDONESIA USING LANDSAT SATELLITE IMAGERY

August Daulat<sup>1</sup>, Widodo Setiyo Pranowo, Syahrial Nur Amri

Marine Research Center, Ministry of Marine Affairs and Fisheries, Republic of Indonesia

Komplek Bina Samudera, Jalan Pasir Putih Raya, Ancol-Jakarta, 14430

<sup>1</sup>e-mail: daul.sinaga@gmail.com

Received: 28 March 2018; Revised: 4 December 2018; Approved: 6 December 2018

**Abstract.** Nusa Penida, Bali was designated as a Marine Protected Area (MPA) by the Klungkung Local Government in 2010 with support from the Ministry of Marine Affairs and Fisheries, Republic of Indonesia. Mangrove forests located in Nusa Lembongan Island inside the Nusa Penida MPA jurisdiction have decreased in biomass quality and vegetation cover. It's over the last decades due to influences from natural phenomena and human activities, which obstruct mangrove growth. Study the mangrove forest changes related to the marine protected areas implementation are important to explain the impact of the regulation and its influence on future conservation management in the region. Mangrove forest in Nusa Penida MPA can be monitored using remote sensing technology, specifically Normalized Difference Vegetation Index (NDVI) from Landsat satellite imagery combined with visual and statistical analysis. The NDVI helps in identifying the health of vegetation cover in the region across three different time frames 2003, 2010, and 2017. The results showed that the NDVI decreased slightly between 2003 and 2010 but increased significantly in 2017, where a mostly positive change occurred landwards and adverse change happened in the middle of the mangrove forest towards the sea.

Keywords: mangrove changes, Nusa Penida MPA, remote sensing, NDVI

## 1 INTRODUCTION

Deforestation and forest degradation has become a major global issue, especially in light of climate change, global warming, and other environmental factors. Global Forest Change analysis has shown global deforestation around the world, whereas Indonesia exhibited an enormous loss in forest approximately 1,021 km<sup>2</sup>/year (Hansen *et al.* 2013), with total primary forest loss estimated at over 60,200 km<sup>2</sup> between 2002 and 2012 and increased on average by 470 km<sup>2</sup>/year (Margono *et al.* 2014).

Indonesia is renowned for the largest mangrove forests in the world,

which have decreased from 42,000 km<sup>2</sup> to less than 31,100 km<sup>2</sup> (Giri *et al.* 2011). Deforestation and forest degradation in Indonesia mostly caused by human intervention and commercial purposes such as agriculture, aquaculture, tourism, coastal development, and other purposes (Kissinger *et al.* 2012, Spalding 2010). Mangrove forests are found in tropical and subtropical regions providing several ecosystem services such as; spawning, breeding, hatching and nursery ground for many living fauna (Cannicci *et al.* 2008). They also provide construction materials, food, and fuel (Rönnbäck *et al.* 2007), and social value

such as cultural sites and recreational purposes (Giri *et al.* 2011). In addition, they have been cited for reducing tsunami impact (Kathiresan and Rajendran 2005), protecting the shoreline of coastal communities (Gedan *et al.* 2011), and reduce the impact of global climate change through carbon storage (Alongi 2008, Alongi *et al.*, 2016 Donato *et al.* 2011, Murdiyarso *et al.* 2015). Mangroves are renowned as productive ecosystems which provide both ecological and socio-economic benefit (Alongi 2002, Walters *et al.* 2008). Mangrove forest in Nusa Lembongan located inside the Nusa Penida Marine Protected Area (MPA) which purposes of conserving biodiversity, economic resources and much more by creating an area of specific regulation (Dudley 2008). The management of MPAs in Indonesia controlled by the Ministry of Marine Affairs and Fisheries, the Ministry of Environment and Forestry, and Local Government (Nurhidayah and Alam 2017, Dirhamsyah, 2016) (Table 1-1).

Kusumaningtyas *et al.* (2014) conducted a blue carbon stock study in Nusa Penida MPA mangrove ecosystems and found five dominant mangrove species in the region with density from 100 to 2620 tree/ha and potential to store carbon up to 14,29 MgC, and CO<sub>2</sub>

absorbed around 54,792. Mg CO<sub>2</sub>e. They estimated the mangrove forest cover in the Nusa Penida MPA using Landsat 7 ETM+ with NDVI technique and measured approximately 164.5 ha. The previous study by Widagti *et al.* (2011) mapped the Nusa Penida region using ALOS AVNIR-2 (Advanced Land Observing Satellite) with 10-meter resolution (ALOS 2017) resulted in the mangrove coverage decrease by 47.09 ha within two years with variation in density change. Both of the researches explained the recent condition of the mangrove forest in Nusa Lembongan Island as part of Nusa Penida MPA after the implementation. Therefore, it is important to analyze the condition before and after the MPA implementation, and as an update data and information regarding the mangrove forest.

The proposed research will integrate remote sensing technology with site observations to monitor the spatial and temporal changes in the mangrove forest coverage and density in Nusa Lembongan from 2003 to 2017. Satellite images of Nusa Penida region in 2003 were chosen as a point when tourism increased significantly in Bali, resulting in massive economic activities in the study area over the years between 2003 and 2010.

Table 1-1: Indonesian Marine Protected Areas

No	Conservation Areas	Ministry of Forestry	Ministry of Marine Affairs and Fisheries	Area (km <sup>2</sup> )
1	Marine National Park	7	1	75,646.71
2	Marine Recreation Park	14	6	20,322.88
3	Wildlife Reserve	5	0	56.78
4	Marine Nature Reserve	6	3	6,001.10
5	Marine Protected Area	0	89	55,614.63
Total		32	99	157,642.10

(Source: Suraji 2014)

Besides 2010 to present (2017) was chosen as the period during which an MPA was designated and enforced in the region by the government. This research examines the condition of mangrove forest regarding the implementation of Nusa Penida MPA in the region.

## 2 MATERIALS AND METHODOLOGY

### 2.1 Site Location

Nusa Penida (Figure 2-1(a)) administratively under the authority of Klungkung District, Bali Province, which famous for its natural resources potencies such as tourism, aquaculture, and fisheries. Nusa Penida consisted of three islands where Nusa Penida is the biggest island compared to other two islands such as Nusa Lembongan and Nusa Ceningan with the total area around 202,84 km<sup>2</sup> and population 46,749 people (Central Bureau of Statistics, 2017). Nusa Penida located apart from Bali island and considered as an area with high marine biodiversity based on its location in Lombok straits as one of the Indonesia Through-Flow (ITF) from the Pacific Ocean to Hindian Ocean through Makassar Straits (Gordon *et al.* 1999, Murray and Arief, 1988). Several National and international collaborations established in Nusa Penida including Blue Economy Project proposed by the Ministry of Marine Affairs and Fisheries, Republic of Indonesia (The Jakarta Post 2014),

and Blue Solutions Project with IUCN (2014).

The Nusa Penida MPA (Figure 2-1(b)) was implemented by applying several restriction zoning systems with specific restriction including core zone (no take zone), special tourism zone, sustainable.

Fishery zone, seaweed farming zone, marine tourism zone, sacred zone, and utilization zone. The MPA's main purpose is to establish and protect the marine biodiversity of the area and reduce conflict among these resource users for the benefit of local communities (Weeks *et al.* 2014).

### 2.2 Materials

This study relies on the utilization of Landsat satellite imagery with 15 years observation started from 2003 until 2017, which divided into three different time frames with seven years gap. The surface reflectance of Landsat 7 Enhanced Thematic Mapper Plus (ETM+) and Landsat 8 (Operational Land Imager (OLI) and Thermal Infrared Sensor (TIRS)) from USGS database used for this study. Landsat 7 ETM + and Landsat 8 (OLI and TIRS) have the same characteristics in sensors, correction methods, and resolution: spatial, temporal, and spectral with repeat 16 days, coverage 170 km X 183 km, and 30-meter resolution (USGS, 2017). They also have similar correction methods and sensors characteristics (Table 2-1).

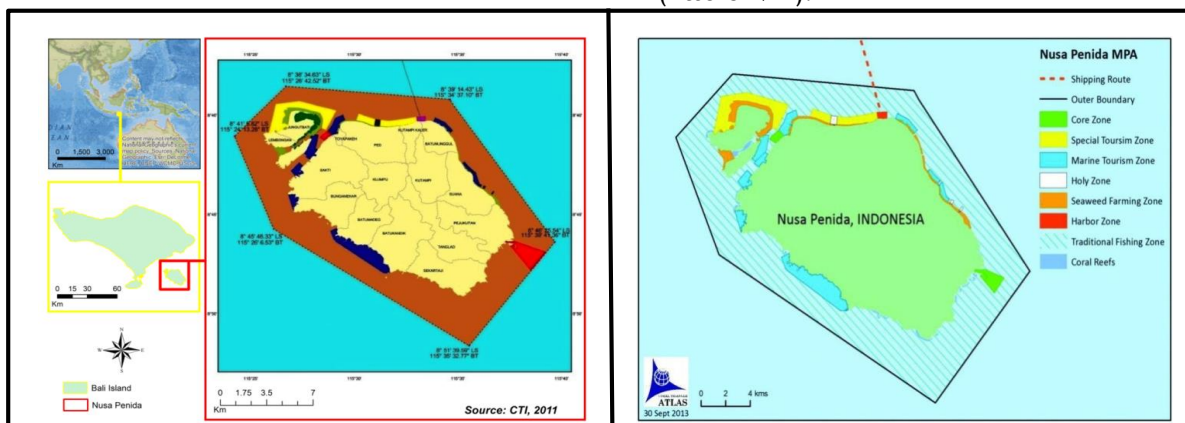


Figure 2-1: Nusa Penida administrative (a) Nusa Penida MPA (b), Bali – Indonesia

Table 2-1: Landsat 7 ETM+ and Landsat 8 (OLI and TIRS sensors)

No	Landsat 7 ETM Bands	Landsat 7 ETM+ Wavelength (µm)	Landsat 8 OLI-TIRS Wavelength (µm)	Landsat OLI-TIRS Bands
1			0.435-0.451	Band 1 30 m Coastal/Aerosol
2	Band 1 30 m Blue	0.441-0.514	0.452-0.512	Band 2 30 m Blue
3	Band 2 30 m Green	0.519-0.601	0.533-0.590	Band 3 30 m Green
4	Band 3 30 m Red	0.631-0.692	0.636-0.673	Band 4 30 m Red
5	Band 4 30 m NIR	0.772-0.898	0.851-0.879	Band 5 30 m NIR
6	Band 5 30 m SWIR	1.547-1.749	1.566-1.651	Band 6 30 m SWIR-1
7	Band 6 30 m TIR	10.31-12.36	2.107-2.294	Band 7 30 m SWIR-2
8	Band 7 30 m SWIR-2	2.064-2.345	0.503-0.676	Band 8 15 m Pan
9	Band 8 15 m Pan	0.515-0.896	1.363-1.384	Band 9 30 m Cirrus
10			10.60-11.19	Band 10 100 m TIR-1
11			11.50-12.51	Band 11 100 m TIR-2

(Source: USGS 2017)

Even though there is a slight difference in length of the light spectrum (spectral range) between two satellites, where most of the bands in Landsat 8 OLI narrower than Landsat 7 ETM+, but the utilization of the visible bands especially for NDVI is not affected so much (Jensen 2015). It's only to create a better visualization for vegetated and non-vegetated area (Irons et al. 2012).

### 2.3 Methods

The research activities in monitoring mangrove forest change utilized the images from Landsat 7

ETM+ and Landsat 8 (OLI and TIRS) from three different years, where Landsat 7 ETM+ used for 2003 and 2010, while Landsat8 OLI and TIRS for 2017 (USGS, 2017). The satellite images in 2010 are used as the references in which the MPA designation begins, while the satellite images from 2003 (pre-designation) and 2017 (after designation) used as the comparison for mangrove forest monitoring before and after the MPA implementation. Several steps conducted in this study such as Image Processing, Image Analysis, and Image Visualization (Figure 2-2).

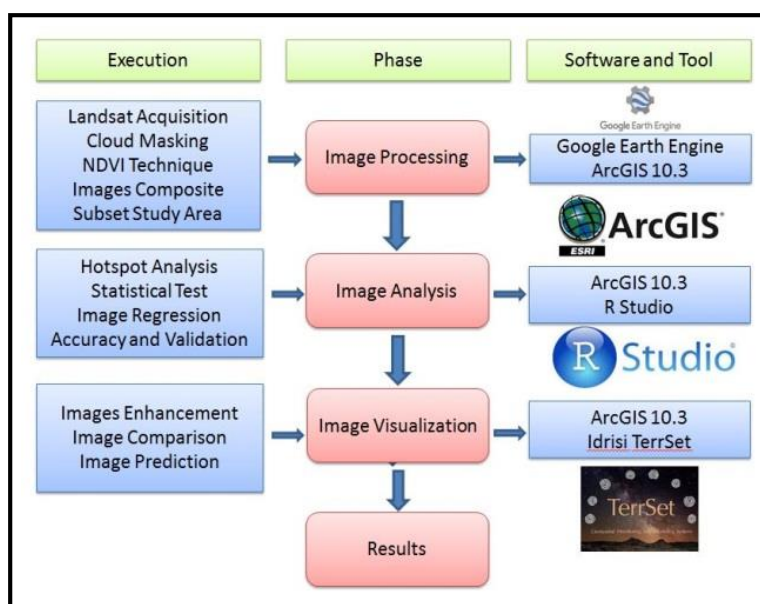


Figure 2-2: Flowchart of methodological process

### 2.3.1 Image Processing

Its multi-temporal, long-term availability, and study length observation, which freely used under the USGS authorization, made Landsat satellite images were chosen as the main dataset (Wulder *et al.* 2012).

Satellite imagery acquisition gathered using Google Earth Engine Application Program Interface (GEE-API) (Gorelick *et al.* 2017), by generating satellite images within two years for each chosen time frame and creating layer stack of images known as image collection. CFMask as the C language version of Mask algorithm function used to generate a cloud mask to standardize dataset from images with high intensity of cloud cover, which have the best overall accuracy compared to other algorithms (Foga *et al.* 2017).

Normalized Difference Vegetation Index (NDVI) is to determine mangrove classification based on its index value, which indicates the presence of green plants and the vegetation health index around the study area utilizing visible Red band combined with Near-Infrared band from the chosen satellite imagery. NDVI value ranging between -1 and +1 where the higher value (positive) showed the high quality of vegetation, while small value (negative) of NDVI indicates non-vegetation (Mather and Koch 2011). NDVI assessed by combining the visible Red and Near-infrared (NIR) light reflected by vegetation and display healthy vegetation that absorbs the most incoming visible light and reflects most of the near-infrared light, and so the opposite for unhealthy vegetation written mathematically as:

$$NDVI = \frac{(NIR - Red)}{(NIR + Red)} \quad (2-1)$$

Where,

NDVI = Normalized Difference Vegetation Index

NIR = Near Infrared canal

Red = Red Canal

Google Earth Engine used to generate the NDVI from image collection and composite the NDVI image collection using reducer section by it median value to reduce noise from “salt and pepper” and avoid outliers in the dataset (Toh *et al.* 2008, Wang and Zhang 1999, Bhosale and Manza 2013).

### 2.3.2 Image Analysis

Several methods used to analyze the satellite images by describing image characteristics, spatial distributions, examine the images using statistical approaches, and image regression. Lastly, accuracy assessment conducted to support the results of the study.

Hotspot analysis performed to identify statistically significant spatial cluster of high values (hotspots) and low values (cold spots) from pixel values between time frames, it also determine the spatial correlation between images based on its pixel values and distinguish the spatial distribution from the dataset in confidence level 99%, 95%, and 90%. Hotspot analysis for each time frame executed using spatial analysis feature in ArcGIS 10.3 Getis-Ord GI\* (Nallan *et al.* 2015).

Statistical analysis performed to examine the characteristics of dataset statistically, and determine the relationship among dataset from three different time frames by generating a regression model. Paired T-test performed to determine statistical evidence related to the mean difference between paired observations or to distinguish the significance of treatment between images in a different time observation.

Image regression implemented to produce statistical information, relationship, and the correlation coefficient between two different images. The first regression analysis compared the points value of observed images

from 2003 and 2010, while the second regression analysis compared the points value observed image from 2010 and 2017 (Eastman 2016).

Accuracy Assessment and error performed on image classification to determine the level of accuracy based on task achievements. The classification ordered to verify the mangrove forest and non-mangrove forest by utilizing the georeferencing and rectification technique of Google Earth High-Resolution image to study area. The accuracy assessment used Cohen's kappa coefficient as the coefficient of agreement between inter-rater which combined the proportions and frequencies among sample units and determine the significance, degree, and stability for illustration (Cohen 1960).

$$K = \frac{\text{Observed} - \text{Expected}}{1 - \text{Expected}} \quad (2-2)$$

Where:

- $K$  = Kappa Coefficient
- Observed = Total number of correct observed points
- Expected = Total number of correct expected points

### 2.3.3 Image Visualization

Visualization of the results carried out by enhancing the images to simplify the contrast for better analysis and precise comparison. Image projection was undertaken by applying the equation resulted from statistical analysis and image regression to new images and compared the condition with or without MPA.

## 3 RESULTS AND DISCUSSION

The map shows mangrove forest health index (Figure 3-1) for three different time frames in Nusa Lembongan island, where the brightest green to red represents the negative value that indicates non-vegetation cover, while the positive value

represented by darker green displayed mangrove vegetation cover.

Time Frame 1 (2003) used the image collection from 2002 – 2003 combination, resulted in 23 images with least cloud cover 4%, Time Frame 2 (2010) from 2009 – 2010, resulted in 17 images with least cloud cover 0.15%, while Time Frame 3 (2010) used the image collection from 2016 – 2017, resulted in 25 images with the least cloud cover 1.7%. This technique used to avoid outliers within the observation and stripes problem occurred in Landsat 7 ETM+ after the 2003 incident (SLC off) that may distract the analysis.

Negative values located spread along the coast (east part and top north) while the positive value spread out landwards with the highest NDVI is 0.919, and the lowest 0.300 based on Landsat USGS classification (Weier and Herring, 2000). Visually the levels of greenness distinguish the mangrove health condition among three different years, wherein 2003 the condition of mangrove forest in the coastal region dominated by healthy vegetation cover showed by dark green color, while mangrove forest landwards is mixed from low to high NDVI.

In 2010, the mangrove forest NDVI in the coastal region, especially in the eastern side decreased slightly as shown in the picture with several areas spotted to transform from dark green to light green. The same thing with the area near to inland also degraded slightly, which explain the mangrove health degradation occurred, while mangrove in the northern coast increased slightly. In 2017 the mangrove forest condition both seawards and landwards dominated by dark green scattered smoothly along the coast and into land compared to the condition in 2003 and 2010, which portrayed as an increase in biomass and healthier vegetation.

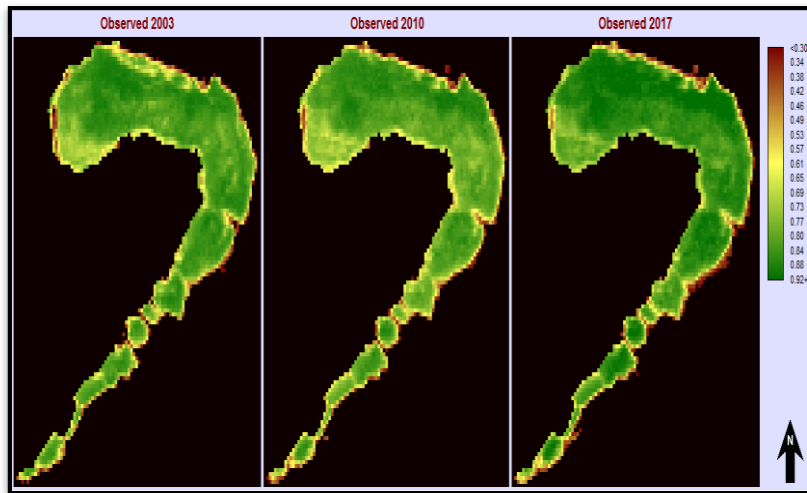


Figure 3-1: Mangrove NDVI over periods

The histogram shows the NDVI composition over periods (Figure 3-2), where the index composition in 2003 somewhat changed a little bit in 2010. Changes in NDVI ranged from 0.7 to 0.9 with most of the NDVI ranged from 0.8 to 0.9 decreased slightly to a range between 0.7 and 0.8, while the NDVI ranged from 0.3 to 0.6 remains steady. Massive changes occurred in 2017 where the NDVI ranged 0.85 to 0.9 escalated significantly in number from below 1.000 points observation to almost 1.500 points, which strengthened by the new highest NDVI above 0.9 with approximately 200 points. The condition in 2017 regarded

as the mangrove health upgrade in this region derived from low to moderate and converted into high NDVI from 2010 condition.

Statistically, the mangrove forest health in 2010 was somewhat decreasing as shown by its both median and mean value with approximately 0.01 gap compared to 2003, while in 2017 the median and mean value escalate significantly by 0.6 to 0.7 respectively compared to 2010. The standard deviation of points observation in 2017 is 0.11, which are varied compared to 2003 and 2010 with around 0.10 (Table 3-1).

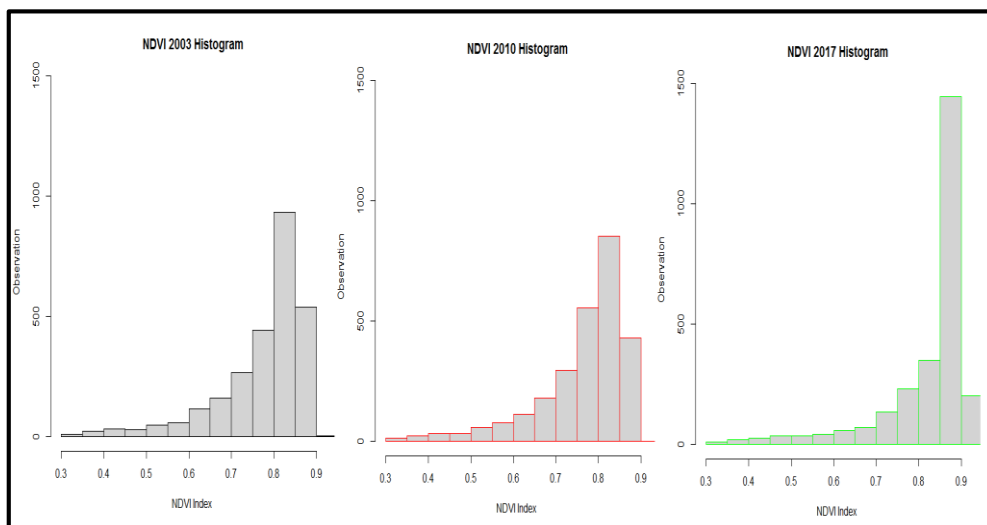


Figure 3-2: Mangrove forest condition based on the number of pixels over time frames



Table 3-1: Statistical information of NDVI index over time frames

No	Category	NDVI 2003	NDVI 2010	NDVI 2017
1	Minimum	0.302	0.311	0.305
2	Maximum	0.903	0.901	0.919
3	Median	0.809	0.796	0.867
4	Mean	0.773	0.763	0.821
5	Standard Deviation	0.106	0.106	0.110

Regression Analysis One (Figure 3-3(a)) derived from the image 2010 with 2003 resulted in a strong positive correlation between both images with  $R^2=0.78$  (coefficient determination), which explained 78% total variation of point observation in image 2003 by the point observation in image 2010. The same methods applied for image 2010 and 2017 named Regression Analysis Two (Figure 3-3(b)) and resulted in the same firm positive correlation with  $R^2=0.78$ . Both Regression Analysis illustrates how the treatment experienced by the NDVI image 2003

influenced NDVI image in 2010, while the NDVI 2010 affecting the image in 2017.

The results of Paired T-test between two images NDVI 2003 and NDVI 2010 using two-sided tailed with confidence level 99% shows that both images are a statistically significant difference between the mean of NDVI 2003 and NDVI 2010 based on its p-value  $< 0.01$ . The same condition occurred between NDVI 2010 and NDVI 2017, which concluded the NDVI image 2003, 2010 and 2017 are statistically different.

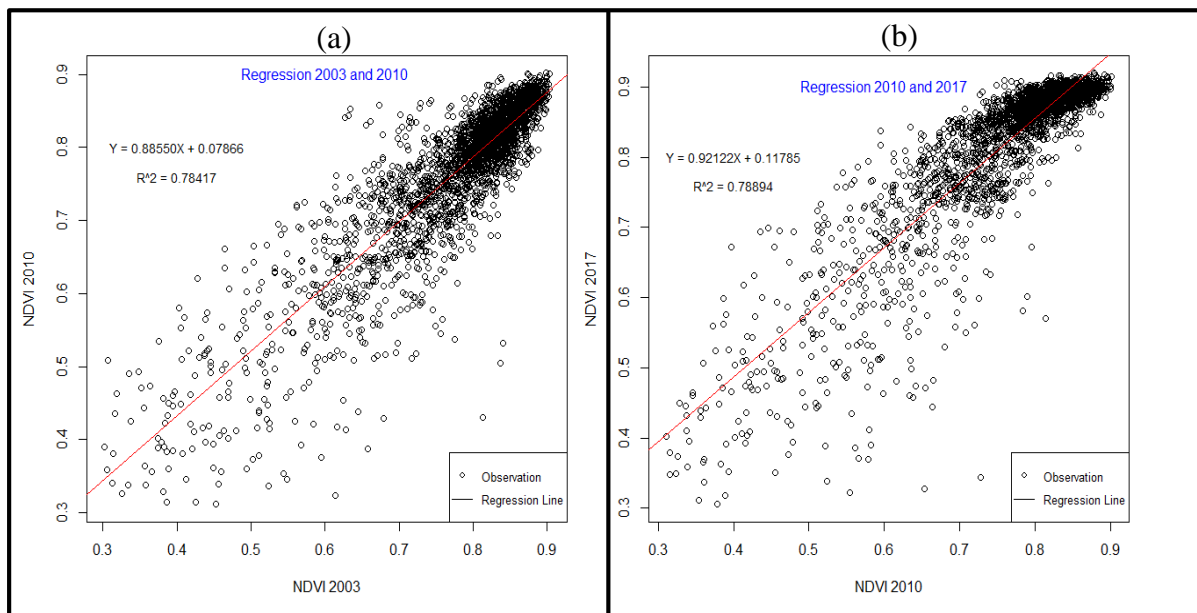


Figure 3-3: Regression between 2003 and 2010 (a) and between 2010 and 2017 (b)

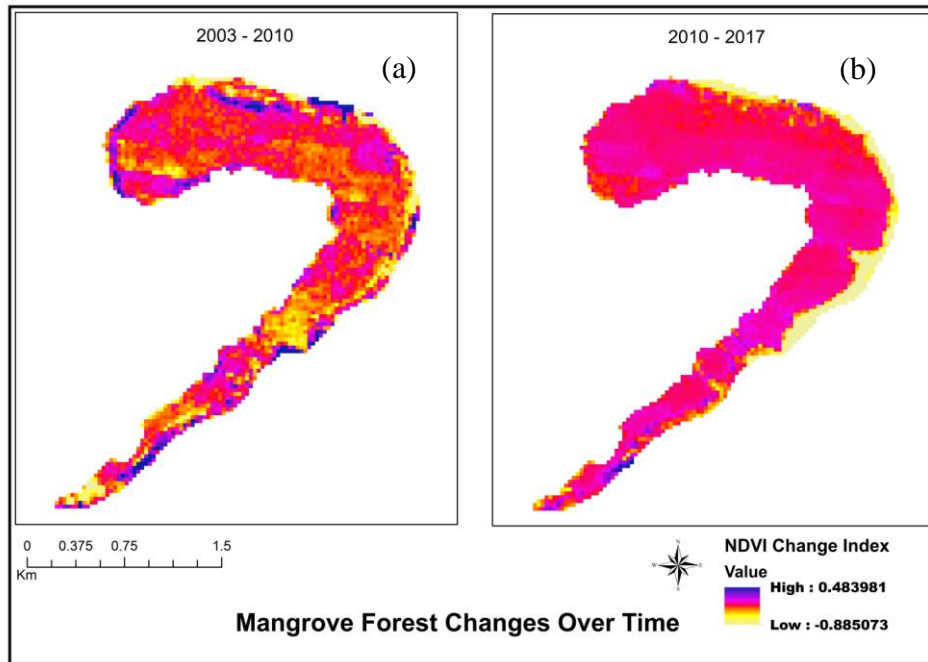


Figure 3-4: Mangrove Change 1 (a) and Mangrove Change 2 (b)

Table 3-2: Statistical information of Mangrove Change

No	Category	Mangrove Change 1	Mangrove Change 2
1	Minimum	-0.382	-0.384
2	Maximum	0.219	0.275
3	Median	-0.010	0.058
4	Mean	-0.009	0.057
5	Standard Deviation	0.051	0.051

Mangrove forest change index over time (Figure 3-4) derived by subtracting two images resulted in mangrove change index named as Mangrove Change 1 (images 2003 and 2010, Figure 3-4(a)), and Mangrove Change 2 (images 2010 and 2017, Figure 3-4(b)). These changes index illustrates the magnitude of changes occurred within the period before the MPA designation and after the MPA designation. Blue color represents the high-positive change of NDVI mangrove forest, while yellow indicates the low-negative change of NDVI. Mangrove Change 1 consisted of mixed change index between positive and negative change, where the Mangrove Change 2 dominated by small positive changes spread along the mangrove forest area, with negative change along the east coast. From 2003

to 2010, more areas appeared to have lower growth in NDVI, while between 2010 and 2017 mostly experienced higher growth with low growth concentrated in the coastal region.

Statistically, the Mangrove Change 1 dominated by negative changes across the region shown by the median and mean value -0.010 and -0.009 respectively, while the opposite condition happened in Mangrove Change 2 where changes controlled by positive value with median 0.058 and mean 0.057. Standard deviations in Mangrove Change 1 and 2 are relatively similar with 0.051, which indicates uniform variation as shown in table 3-2.

The Mangrove Change index histogram (Figure 3-5) explains the changes in NDVI before and after MPA

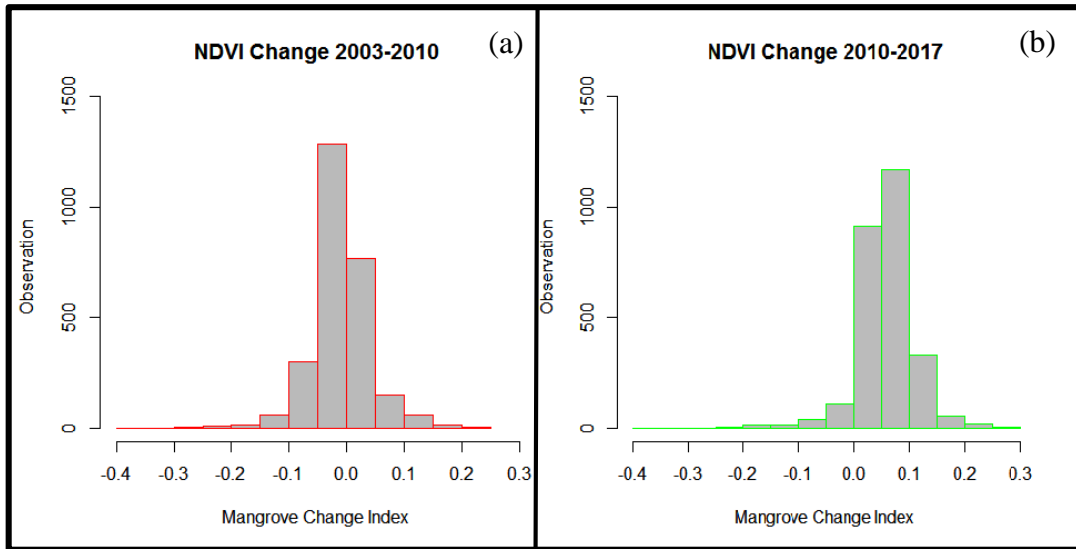


Figure 3-5: Mangrove Change 1 Index (a) and Mangrove Change 2 Index (b)

designation in Nusa Penida. Before the MPA designation (Figure 3-5(a)), the mangrove forest change dominated by negative to slightly no change, which considered as degradation condition demonstrated by numerous values ranged between -0.1 to below 0.05. While after the MPA designation (Figure

3-5(b)) its turnout to a positive value with range started from 0.05 to 0.15.

Mangrove Change Regression Analysis derived from Mangrove Change 1 and Mangrove Change 2 resulted in a regression equation model to estimate the effect of MPA on the change in mangrove NDVI per 7 years as follows:

$$Y = MPA * 0.067585 - 0.0098933 \tag{3-1}$$

Where,

Y : Change NDVI

MPA : The average effect of the MPA implementation on change in NDVI/7years

$$MPA\ Impact = Observed\ 2017 * 0.067585 - 0.0098933 \tag{3-2}$$

$$NDVI\ in\ 2017\ without\ MPA = Observed\ 2017 - 0.0098933 \tag{3-3}$$

The impact of MPA designation in Nusa Lembongan was mapped using the Mangrove Change Regression Analysis (Figure 3-6(a)), and project the condition of mangrove forest in Nusa Lembongan without MPA (Figure 3-6(b)). The NDVI impact mostly occurred almost in all mangrove forest regions, especially positive impact landwards indicated by dark green, while yellow color displayed slightly no changing effect, and red color that represents the negative impact of

the MPA designation occurred along the coastal region.

The accuracy assessment using Cohen's Kappa resulted in similar Kappa coefficient (Table 3-3) between periods with average 0.71, which means that the accuracy assessment displays a good agreement between the invented random samples applied to Google Earth High-Resolution with the satellite images.

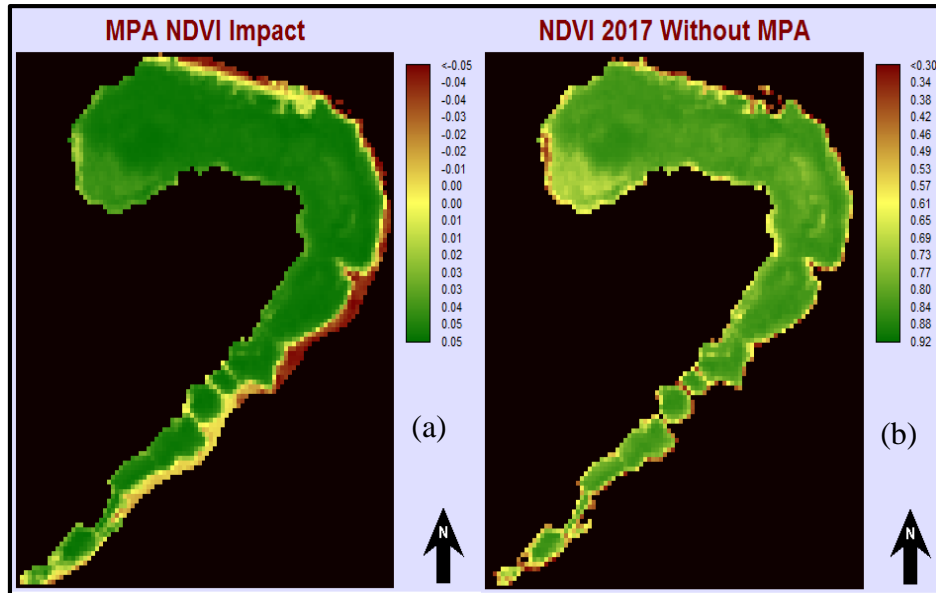


Figure 3-6: The NDVI Impact (a), and NDVI 2017 without MPA (b)

The Hotspot analysis (Figure 3-7) resulted in three different images as shown in picture above, where the blue (dark) colour illustrate the spatial distribution of low values (cold spot) based on its NDVI values, while the red (bright) colour, represent the high values (hotspot) in three confidence level 99%, 95%, and 90% (Nallan *et al.* 2015).

In 2003 the hotspot and cold-spot distributed evenly along the mangrove forest area within three different confidence level, while in 2010 the hotspot clustered in the middle of mangrove forest, which associated with the fall of NDVI in 2010. Hotspot analysis in 2017 shows the domination of high value across the region and strengthens statistics information where massive positive conversion of NDVI

occurred in that year compared to the previous periods in 2010 and 2003.

Based on several images resulted from remote sensing approach, the mangrove forest condition in Nusa Penida MPA changed substantially, which influenced by the MPA implementation in 2010. The mangrove forest health, which associated with biomass vegetation in 2003 slightly decreased in 2010, and increase considerably in 2017. The condition of mangrove forest in 2003, 2010, and 2017 are significantly different based on paired t-test result ( $p\text{-value} < 0.01$ ) using confidence interval 99%, where the mean difference in 2003-2010 and 2010-2017 are 0.009 and 0.057 respectively.

Table 3-3: Classification accuracy using Cohen’s Kappa methods

No	Years	Accuracy (%)	Kappa Coefficient
1	2003	88.40	0.70
2	2010	88.00	0.71
3	2017	89.73	0.73
4	Average	88.71	0.71

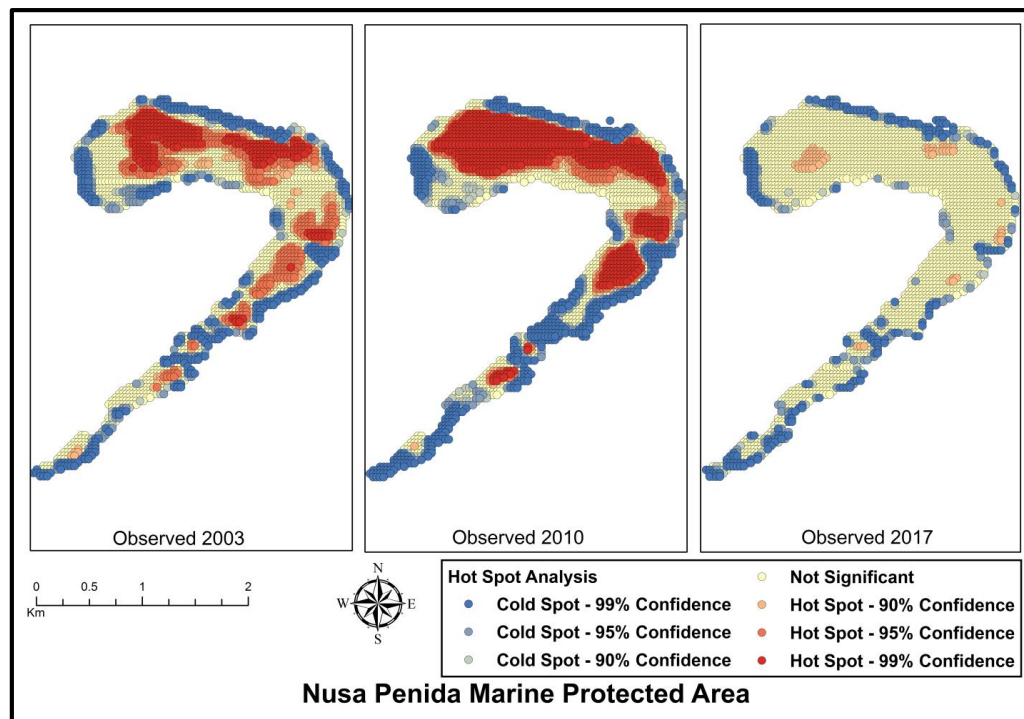


Figure 3-7: Hotspot Analysis in Nusa Penida MPA

Mostly positive change in 2010 occurred landwards (west direction), while negative change considered as mangrove degradation happened in the middle of mangrove forest towards the sea. This might happened due to tidal, wave combined with sea level rise in the region, and its location directly adjacent to Lombok Straits in the west, which famous by its strong current (Lubis and Yuningsih 2016) and internal wave (Rachmayani *et al.* 2010).

The condition of mangrove forest in 2017 experienced an upgrade evenly across the region supported by statistical analysis, hotspot analysis, and image visualization. Mangrove forest change in 2017 dominated by a small positive value in almost all mangrove area, especially in the middle (both landwards and seawards), which indicates growth during the MPA implementation. Statistics table and information through histogram strengthen the evidence. The similar condition in 2010, where mangrove forest in the coastal region suffered from nuisance derived from tidal, wave and

sea level rise combination (Lovelock *et al.* 2017).

Image regression before and after the MPA implementation shows strong positive correlation explained by  $R^2 = 0.78$ , which conclude the contribution of MPA to the region where the condition before the implementation dominated by negative to slightly no change, while after the MPA implementation it is slowly turned into positive change.

#### 4 CONCLUSION

The output of this study is relevant to environmental and conservation management in Nusa Penida MPA, primarily to mangrove forest management. The mangrove forest health decreased in quality from 2003 to 2010 before the MPA designation and increased significantly from 2010 to 2017 after the MPA designation. The MPA implementation play key role in managing, conserving and protecting the existing ecosystem with its spatial planning, zoning system, and strict regulation, but other driver

natural and unnatural reasons also contributed to the changes.

Field observation needed for ground truthing to support the accuracy assessment, land use and land use change classification for better, and comprehensive analysis in the MPA implementation. Lastly, it is vital to put attention on the MPA management and implementation in Nusa Penida MPA as a role model on spatial planning included how to address several issues within stakeholder for better natural resource management in the future.

### ACKNOWLEDGEMENT

The authors would like to thank everyone who involved in the preparation of this paper for their support including inputs, corrections, and suggestions. Highly appreciation is given to USGS for the satellite imagery free data access. Last but not least, Andreas A. Hutahaeen from the Coordinating Ministry of Maritime Affairs, and the Marine and Coastal Data Laboratory and team, especially Joko Subandriyo who supported this research.

### REFERENCES

Advanced Land Observing Satellite Data, (2017), Alos Data. <http://www.alos-restec.jp/en/staticpages/index.php/abotalos>.

Alongi D., Murdiyarso D., Fourqurean J., Kauffman J., Hutahaeen A., Crooks S., Lovelock C., Howard J., Herr D., Fortes M, (2016), Indonesia's Blue Carbon: a Globally Significant and Vulnerable Sink for Seagrass and Mangrove Carbon. *Wetlands Ecology and Management*, 24, 3-13.

Alongi DM, (2002), Present State and Future of the World's Mangrove Forests. *Environmental Conservation*, 29, 331-349.

Alongi DM, (2008), Mangrove Forests: Resilience, Protection From Tsunamis, and Responses to Global Climate

Change. *Estuarine, Coastal and Shelf Science*, 76, 1-13.

Bhosale NP, Manza RR, (2013), Analysis of Effect of Noise Removal Filters on Noisy Remote Sensing Images. *International Journal of Scientific & Engineering Research (IJSER)*, 4, 1151.

Cannicci S., Burrows D., Fratini S., Smith T. J., Offenbergh J., Dahdouh-Guebas F, (2008), Faunal Impact on Vegetation Structure and Ecosystem Function in Mangrove Forests: A Review. *Aquatic Botany*, 89, 186-200.

Cohen J., (1960), A Coefficient of Agreement for Nominal Scales. *Educational and Psychological Measurement*, 20, 37-46.

Dirhamsyah, (2016), Setbacks in the Development of Marine Protected Areas in Indonesia. *Australian Journal of Maritime & Ocean Affairs*, 8, 87-100.

Donato DC, Kauffman JB, Murdiyarso D., Kurnianto S., Stidham M., Kanninen M., (2011), Mangroves Among the Most Carbon-rich Forests in the Tropics. *Nature Geoscience*, 4, 293-297.

Dudley N., (2008), Guidelines for Applying Protected Area Management Categories, IUCN.

Foga S., Scaramuzza PL, Guo S., Zhu Z., Dilley RD, Beckmann T., Schmidt GL, Dwyer JL, Hughes MJ, Laue B., (2017), Cloud Detection Algorithm Comparison and Validation for Operational Landsat Data Products. *Remote Sensing of Environment*, 194, 379-390.

Gedan KB, Kirwan ML, Wolanski E., Barbier, EB, Silliman BR, (2011), The Present and Future Role of Coastal Wetland Vegetation in Protecting Shorelines: Answering Recent Challenges to the Paradigm. *Climatic Change*, 106, 7-29.

Giri C., Ochieng E., Tieszen LL, Zhu Z., Singh A., Loveland T., Masek J., Duke N., (2011), Status and Distribution of Mangrove Forests of the World Using Earth Observation Satellite Data. *Global Ecology and Biogeography*, 20, 154-159.

Gordon AL, Susanto RD, Ffield A., (1999), Throughflow Within Makassar Strait. *Geophysical Research Letters*, 26, 3325-3328.

- Gorelick N., Hancher M., Dixon M., Ilyushchenko S., Thau D., Moore R., (2017), Google Earth Engine: Planetary-scale Geospatial Analysis for Everyone. *Remote Sensing of Environment*.
- Hansen MC, Potapov PV, Moore R., Hancher M., Turubanova S., Tyukavina A., Thau D., Stehman S., Goetz S., Loveland T., (2013), High-Resolution Global Maps of 21st-Century Forest Cover Change. *Science*, 342, 850-853.
- Irons JR, Dwyer JL, Barsi JA, (2012), The Next Landsat Satellite: The Landsat Data Continuity Mission. *Remote Sensing of Environment*, 122, 11-21.
- Jensen JR, (2015), *Introductory Digital Image Processing: A Remote Sensing Perspective*, Prentice Hall Press.
- Kathiresan K., Rajendran N., (2005), Coastal Mangrove Forests Mitigated Tsunami. *Estuarine, Coastal and Shelf science*, 65, 601-606.
- Kissinger G., Herold M., De Sy V., (2012), *Drivers of Deforestation and Forest Degradation: A Synthesis Report for REDD+ Policymakers*. Vancouver, Canada: Lexeme Consulting.
- Kusumaningtyas MA, Daulat A., Suryono DD, Ati RNA, Kepel TL, Rustam A., Rahayu YP, Sudirman N., Hutahaean AA, (2014), Blue Carbon Stock of Mangrove Ecosystem in Nusa Penida, Bali. 12th Biennial Conference of Pan Ocean Remote Sensing Conference (PORSEC 2014).
- Lovelock CE, Feller IC, Reef R., Hickey S., Ball MC, (2017), Mangrove Dieback During Fluctuating Sea Levels. *Scientific Reports*, 7, 1680.
- Margono BA, Potapov PV, Turubanova S., Stolle F., Hansen MC, (2014), Primary Forest Cover Loss in Indonesia Over 2000-2012. *Nature Climate Change*, 4, 730-735.
- Mather PM, Koch M., (2011), *Computer Processing of Remotely-sensed Images: An Introduction*, John Wiley & Sons.
- Murdiyarmo D., Purbopuspito J., Kauffman J B, Warren MW, Sasmito SD, Donato DC, Manuri S., Krisnawati H., Taberima S., Kurnianto S., (2015), The Potential of Indonesian Mangrove Forests for Global Climate Change Mitigation. *Nature Climate Change*, 5, 1089-1092.
- Murray SP, Arief D., (1988), Throughflow into the Indian Ocean Through the Lombok Strait, January 1985–January 1986. *Nature*, 333, 444-447.
- Nallan SA, Armstrong LJ, Tripathy AK, Teluguntla P., (2015), *Hotspot Analysis Using NDVI Data for Impact Assessment of Watershed Development. Technologies for Sustainable Development (ICTSD)*, 2015 International Conference on, 2015. IEEE, 1-5.
- Nurhidayah L., Alam S., (2017), MPAs and Fisheries in the Context of Food Security and Sustainable Livelihoods in Indonesia: Case study of MPAs in Karimunjawa and Mayalibit Papua, Indonesia. In: Westlund, L., Charles, A., Garcia, S. M., Sanders, J. (eds.) *Marine Protected Areas: Interactions with Fishery Livelihoods and Food Security*. Rome: the Food and Agriculture Organization of the United Nations and International Union for Conservation of Nature.
- Rachmayani R., Ningsih NS, Hardi S., Brodjonegoro IS, (2010), Dinamika Penjalaran Gelombang Internal di Selat Lombok. *Indonesian Journal of Marine Sciences*, 13, 1-12.
- Ronnback P., Crona B., Ingwall L., (2007), The Return of Ecosystem Goods and Services in Replanted Mangrove Forests: Perspectives from Local Communities in Kenya. *Environmental Conservation*, 34, 313-324.
- Spalding M., (2010), *World Atlas of Mangroves*, Routledge.
- Toh KKV, Ibrahim H., Mahyuddin MN, (2008), Salt and Pepper Noise Detection and Reduction Using Fuzzy Switching Median Filter. *IEEE Transactions on Consumer Electronics*, 54.
- Walters BB, Ronnback P, Kovacs JM, Crona B., Hussain SA, Badola R., Primavera JH, Barbier E., Dahdouh-Guebas F.. (2008), *Ethnobiology, Socio-economics and Management of Mangrove Forests: A Review*. *Aquatic Botany*, 89, 220-236.



- Wang Z., Zhang D., (1999), Progressive Switching Median Filter for the Removal of Impulse Noise From Highly Corrupted Images. *IEEE Transactions on Circuits and Systems II: Analog and Digital Signal Processing*, 46, 78-80.
- Weeks R., Alino PM, Atkinson S., Bekdia P., Binson A., Campos WL, Djohani R., Green AL, Hamilton R., Horigue V., (2014), Developing Marine Protected Area Networks in the Coral Triangle: Good Practices for Expanding the Coral Triangle Marine Protected Area System. *Coastal Management*, 42, 183-205.
- Weier J., Herring D, (2000), Measuring Vegetation (NDVI & EVI). *Earth Observatory, National Aeronautics and Space Administration*
- Widagti N., Triyulianti I., Manessa MDM, (2011), Changes In Density Of Mangrove Forest In Nusa Lembongan, Bali. *Proceeding Of The 2nd Cresos International Symposium On South East Asia Environmental Problems And Satellite Remote Sensing Denpasar, Bali-Indonesia*, 2011. 171-176.
- Wulder MA, Masek JG, Cohen WB, Loveland TR, Woodcock CE, (2012), Opening the Archive: How Free Data has Enabled the Science and Monitoring Promise of Landsat. *Remote Sensing of Environment*, 122, 2-10.



# DETECTING THE LAVA FLOW DEPOSITS FROM 2018 ANAK KRAKATAU ERUPTION USING DATA FUSION LANDSAT-8 OPTIC AND SENTINEL-1 SAR

Suwarsono<sup>1\*</sup>, Indah Prasasti<sup>1</sup>, Jalu Tejo Nugroho<sup>1</sup>, Jansen Sitorus<sup>1</sup>, and Djoko Triyono<sup>2</sup>

<sup>1</sup>Remote Sensing Application Center,

Indonesian National Institute of Aeronautics and Space (LAPAN)

<sup>2</sup>Department of Physics, Faculty of Mathematic and Natural Sciences,  
Universitas Indonesia

\*E-mail: suwarsono@lapan.go.id

Received: 4 December 2018; Revised: 24 December 2018; Approved: 27 December 2018

**Abstract.** The increasing volcanic activity of Anak Krakatau volcano has raised concerns about a major disaster in the area around the Sunda Strait. The objective of the research is to fuse Landsat-8 OLI (Operational Land Imager) and Sentinel-1 TOPS (Terrain Observation with Progressive Scans), an integration of SAR and optic remote sensing data, in observing the lava flow deposits resulted from Anak Krakatau eruption during the middle 2018 eruption. RGBI and the Brovey transformation were conducted to merge (fuse) the optical and SAR data. The results showed that optical and SAR data fusion sharpened the appearance of volcano morphology and lava flow deposits. The regions are often constrained by cloud cover and volcanic ash, which occurs at the time of the volcanic eruption. The RGBI-VV and Brovey RGB-VV methods provide better display quality results in revealing the morphology of volcanic cone and lava deposits. The entire slopes of Anak Krakatau Volcano, with a radius of about 1 km from the crater is an area prone to incandescent lava and pyroclastic falls. The direction of the lava flow has the potential to spread in all directions. The fusion method of optical Landsat-8 and Sentinel-1 SAR data can be used continuously in monitoring the activity of Anak Krakatau volcano and other volcanoes in Indonesia both in cloudy and clear weather conditions.

Keywords: *lava flow, Anak Krakatau, data fusion, Landsat-8, Sentinel-1 SAR*

## 1 INTRODUCTION

Anak Krakatau Volcano, which is located on The Sunda Strait, administratively located in the South Lampung Regency, is one of the 129 Indonesian active volcanoes. Anak Krakatau volcano itself, since its emergence in 1929 until now, has erupted at least 80 times. In other words, the eruption of which has occurred every year in the form of explosive or effusive eruptions. The time of the volcano is between 1 - 8 years but the eruption can occur 1 - 6 times a year (Sutawidjaja 2006).

The eruption of Krakatau on 27 August 1883, was one of the most powerful eruptions in history. The eruption destroyed most of the volcanic island of Krakatoa in the strait separating the land of Sumatra and Java. Then, there was an eruption from 1927 to 1929 and produced a new volcano known as Anak Krakatau. Until now, this volcano continues to experience growth (Agustan *et al.* 2012).

The eruption from October 2007 till August 2008 was characterized by Strombolian activity. During this eruption, a new crater was formed on

the southwestern flank of the volcano just below the main crater, producing ash plumes as well as lava flows. (Agustan *et al.* 2012).

Based on the records from the Center for Volcanology and Geological Disaster Mitigation (<http://www.vsi.esdm.go.id/index.php/gunungapi/aktivitas-gunungapi>), the last eruption in 2018 to date occurred on June 25-26, July 16, August 3, August 17, August 23, October 3 and 6, and November 16 and 26. The eruption on July 23, 2018 and September 23, in addition to removing volcanic ash, produced incandescent lava melt, down the slope, leads South and South East to reach the sea.

Many studies on this volcano mainly discuss about the famous Krakatau eruption on 1883 and how it caused tsunamis (Rampino and Self 1982; Francis 1985; Dörries 2003); the growth of Anak Krakatau and Anak Krakatau (Sutawidjaja 1997, 2006; Deplus *et al.* 1995; Ibs-von Seht 2008), and the ground deformation of Anak Krakatau (Agustan *et al.* 2012). However, the studies on distribution of lava flow from recent eruption are still limited.

The objective of the research is to observe the lava flow deposits resulted from Anak Krakatau eruption during middle 2018 eruption. The fusion of Landsat-8 OLI (Operational Land Imager) and Sentinel-1 TOPS (Terrain Observation with Progressive Scans), as the integration of SAR and optic remote sensing data, was used to identify of the lava flow deposits.

Landsat-8 satellite, the newest satellite of Landsat satellite series, is operated by the National Aeronautics and Space Administration (NASA) and the Department of the Interior United States of Geological Survey (USGS).

Landsat-8 has the advantages to its predecessors.

Tabel 1-1: OLI spectral and spatial specification (Iron *et al.*, 2012)

Bands	Band with (μm)	GSD (m)
1	0.433 – 0.453	30
2	0.450 – 0.515	30
3	0.525 – 0.600	30
4	0.630 – 0.680	30
5	0.845 – 0.885	30
6	1.560 – 1.660	30
7	2.100 – 2.300	30
8	0.500 – 0.680	15
9	1.360 – 1.390	30

Table 1-2: TIRS spectral bands and spatial resolution (Irons *et al.* 2012)

Bands	Center wavelength (μm)	Minimum lower band edge (μm)
10	10.9	10.6
11	12.0	11.5

Landsat-8 carries an Operational Land Imager (OLI), consists of nine spectral channels with a spatial resolution of 30 m (15 m for the panchromatic channel), and the Thermal Infrared Sensor (TIRS) which will measure land surface temperature in two thermal bands with a 100 m spatial resolution (Irons *et al.* 2012) (Table 1-1 and Table 1-2).

The Sentinel-1 is a C-band (5.36 GHz) SAR data product of European Space Agency (ESA). The product has been acquired in four different modes namely Stripmap (SM), Interferometric Wide swath (IW), Extra-Wide swath (EW) and Wave (WV). The instrument was designed with one transmitter and two receiver chain. It supports operation in a single and dual polarization (Periasamy 2018). The data has been acquired with Ground Swath width of 250 km and Azimuth pixel spacing of 14.1 m. The satellite has Orbital Repeat Cycle of 12 days (Martinez *et al.* 2016).

In many applications, the quality of remote sensing image data is a very important aspect. In many situations, the data from one type of sensor is not enough to provide an accurate analysis of observed objects. The basic purpose of data fusion is to get more quality information compared to what we will get from a single sensor. Therefore, the fusion of multi-sensor data has been an intense field of research in recent years (Reulke *et al.* 2013). Optical and radar images have two different aspects of analyzing satellite imagery. Optical images such Landsat-8 OLI have the advantages in terms of providing more semantic information obtained from multispectral data. The disadvantage is that the presence of clouds will be a barrier to analyzing objects under the cover. Meanwhile, radar images, such as Sentinel-1 SAR, have the advantages in terms of not being affected by clouds or recording time (day or night). By combining both types of data, it is expected to improve image quality for the analysis of objects to be observed.

So, by combining the two types of data (Landsat-8 and Sentinel-1 SAR), it is expected that images with better quality will be obtained for the interpretation of lava flow deposits.

## 2 MATERIALS AND METHODOLOGY

### 2.1 LOCATION AND DATA

The research location is Krakatau volcano complex. The Krakatau complex consists of four islands which are Sertung, Panjang, Rakata, and Anak Krakatau. Sertung, Panjang, and Rakata Island are the remnants of the caldera collapse due to the 1883 Krakatau eruption. Anak Krakatau emerged in 1929, was about 46 years after the paroxysmal eruption. This volcano is a stratovolcano and was built by alternating layers of lava and pyroclastic deposits that had been erupted since the 1930s. Since its emergence at sea level in 1929 until now, the growth of Anak Krakatau Volcano is very fast. The height of the Anak Krakatau volcano peak from 1930 to 2005, for 75 years, reached 315 m. The estimated acceleration of growth is an average of four meters per year (Sutawidjaja 1997; 2006).

The Krakatau complex is covered by Landsat-8 satellite coverage for path/row 123/064. Administratively, the research sites are included in the areas of the Lampung Selatan Regency, Lampung Province. Figure 2-1 shows the location of the research.

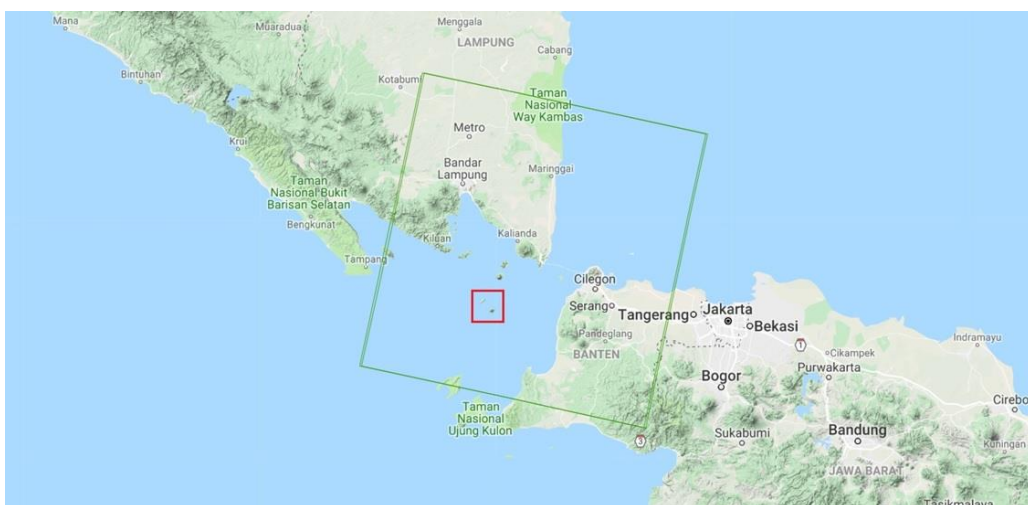


Figure 2-1: Location of the study Anak Krakatau Volcano (red rectangle), coverage of Landsat-8 for path/row 123/064 (green rectangle). Map source: <http://landsat-catalog.lapan.go.id/>.

The optical data used were Landsat-8, path / row 123/064. The time of data acquisition was 1 October 2018. Landsat-8 data were obtained from The Remote Sensing Technology and Data Center of Indonesian National Institute of Aeronautics and Space (LAPAN), through the <http://landsat-catalog.lapan.go.id/>. The data format is GeoTIFF. The level of Landsat-8 is level one terrain-corrected product (L1T). The data that available to users is the radiometrically and geometrically corrected image (Zanter 2015). The L1 Single Look Complex (SLC) products of Sentinel-1 TOPS were obtained from Alaska Satellite Facility through <https://www.asf.alaska.edu/>. The Sentinel-1 TOPS IW mode is the main mode of operations for the systematic monitoring of large land and coastal areas (Torres et al. 2012).

Table 2-1: Sentinel 1 Interferometric wide Swath Mode SLC Product Parameters (Martinez et al. 2016).

Mode id.	IW1	IW2	IW3
Incidence angles	32.9°	38.3°	43.1°
Slant range resolution	2.7 m	3.1 m	3.5 m
Range Bandwidth	56.5 MHz	48.3 MHz	42.79 MHz
Azimuth resolution	22.5 m	22.7 m	22.6 m
Processing Bandwidth	327 Hz	313 Hz	314 Hz
Doppler Centroid span ( $\Delta f_{bc}$ )	5.2 kHz	4.4 kHz	4.6 kHz
Slant range pixel spacing		2.3 m	
Range sampling frequency		64.35 MHz	
Azimuth pixel spacing		14.1 m	
Azimuth sampling frequency		486.49 Hz	
Azimuth steering angle		$\pm 0.6^\circ$	
Burst length ( $T_{focused}$ )		2.75s / $\approx 20$ km	
Ground Swath width		250 km	
Slice length		170 km	
Orbital Repeat Cycle		12 days	
Orbit height		698 – 726 km	
Wavelength		5.547 cm	
Polarization		Single (HH or VV) or Dual (HH+HV or VV+VH)	

Table 2-1 show the Sentinel 1 Interferometric Wide Swath Mode, SLC product parameters. The SAR data used were Sentinel-1 TOPS, beam mode Interferometric Wide swath (IW), Single Look Complex (SLC) products, flight

direction Descending, polarization VV and VH, path/frame 47/614. The acquisition of the data was on 17 September 2018. The acquisition date is selected as it is close to Landsat-8 data acquisition time.

## 2.2 METHODS

### 2.2.1 DATA CALIBRATION

Landsat-8 OLI data were converted to Top of Atmosphere (TOA) spectral radiance. Then, OLI data were converted to TOA reflectance. The following equation is used to convert DN values to TOA reflectance for OLI data as follows (Zanter 2015):

$$\rho\lambda' = M_\rho Q_{cal} + A_\rho \tag{2-1}$$

in which  $\rho\lambda'$  is TOA planetary reflectance (without correction for solar angle).  $M_\rho$  is Band-specific multiplicative rescaling factor,  $A_\rho$  is band-specific additive rescaling factor, and  $Q_{cal}$  is quantized and calibrated standard product pixel values (DN). Sun angle correction of TOA reflectance can be calculated by using the following equation (Zanter 2015):

$$\rho\lambda = \frac{\rho\lambda'}{\cos(\theta_{sz})} = \frac{\rho\lambda'}{\sin(\theta_{se})} \tag{2-2}$$

in which  $\rho\lambda$  is TOA planetary reflectance,  $\theta_{SE}$  is local sun elevation angle.  $\theta_{SZ}$  is local solar zenith angle,  $\theta_{SZ} = 90^\circ - \theta_{SE}$ .

TOA reflectance does not correct the atmospheric effects. Thus DOS1 (Dark Object Subtraction 1) was implemented for converting Landsat images from TOA reflectance to surface reflectance (Chavez 1996). The DOS1 method is very simple because it doesn't require any information about atmospheric conditions, but the results are not as accurate as the Landsat Surface Reflectance High Level Data

Products. DOS1 method was conducted for atmospheric correction.

Sentinel-1 TOPS IW consists of VH and VV polarization. The Level-1 GRD (Grid) product was derived from internal Side Looking Complex (SLC). The Radiometric Calibration was performed for Amplitude imageries of VV and VH using calibration parameter  $A_\sigma$  to transform the radar backscattering into Radar Cross Section ( $\sigma^\circ$ ) (Equation 2-3) (Periasamy 2018).

$$\sigma^\circ = DN^2 / A\sigma^2 \quad (2-3)$$

in which DN represents Digital Number in the SAR Imagery. The results of the procedure (Eq. 2-3) are in  $\sigma_{VV}^\circ$  and  $\sigma_{VH}^\circ$  which are the conversion products from slant range to ground range.

The speckle reduction was performed by using Refined Lee filter to remove the noise and to smoothen the imagery. Then the Range Doppler Correction is performed to the speckle removed imagery to position the data geographically. Sigma naught ( $\sigma^\circ$ ) is the radar reflectivity per unit area in ground range. Sigma naught related to power returned to the antenna from the ground. Sigma naught values are directly related to the ground. The SRTM90 DEM produced from the U.S. Geological Survey (USGS) was used in this calibration processes.

### 2.2.2 DATA FUSION OF OPTICAL AND SAR POLARIMETRIC

To observe the eruption activities, volcano morphology, and lava flow deposits resulted from the eruption, both Landsat-8 optical and Sentinel-1 TOPS SAR were used. RGBI transformation was conducted to merge (fuse) the optical and SAR data. RGBI transformation is a simple method for data fusion. In this step, for RGBI transformation, band SWIR<sub>s</sub> (band 6), NIR (band 5), and RED (band 4) of

Landsat-8 were input as Red, Green and Blue channel respectively. The combination band 6, 5 and 4 of Landsat-8 is useful for lava deposits identification. From the band combination, the lava deposit object looks reddish, the vegetation looks greenish and the water appears black or bluish. Then the sigma naught backscatter  $\sigma_{VV}^\circ$  and  $\sigma_{VH}^\circ$  of Sentinel-1 TOPS were input as intensity channel.

The Brovey transformation was also conducted for data fusion. The Brovey transformation can be used to merge images with different spatial and spectral characteristics (Jensen 2005). This transformation changes the reflectance value for each multispectral channel (R, G, and B), into new values (RP, GP, and BP). P is the co-registered band of higher spatial resolution images. The equation of Brovey Transformation used is as follows:

$$RP = R \cdot P / (R+G+B) \quad (2-4)$$

$$GP = G \cdot P / (R+G+B) \quad (2-5)$$

$$BP = B \cdot P / (R+G+B) \quad (2-6)$$

In this step, for Brovey transformation, band 6, 5, and 4 of Landsat-8 were input as Red, Green and Blue channel respectively. Then the sigma naught backscatter  $\sigma_{VV}^\circ$  and  $\sigma_{VH}^\circ$  of Sentinel-1 TOPS were input as P.

The images fusion of Landsat-8 optic and Sentinel-1 SAR, both from RGBI and Brovey were compared with the images fusion of Landsat-8, band 6,5,4 and panchromatic band (band 8), with the same methods.

## 3 RESULTS AND DISCUSSION

Optical and SAR data fusion are able to sharpen the appearance of volcano morphology and lava flow deposits. Especially in the region, it is



often constrained by cloud cover and volcanic ash, which occurs when the volcanic eruption.

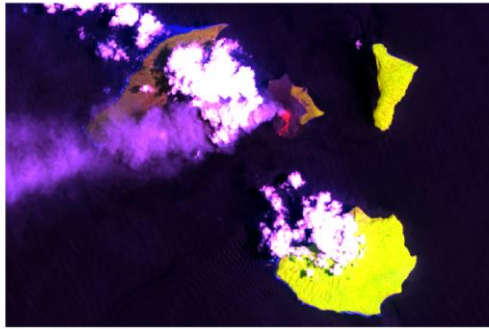
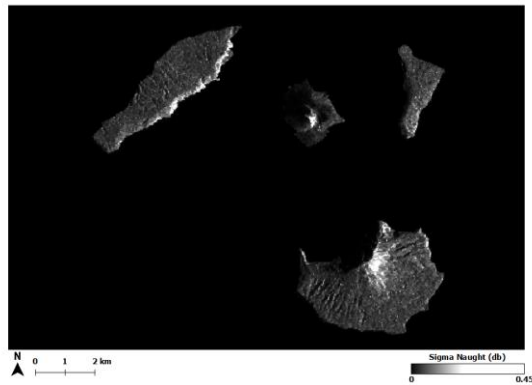
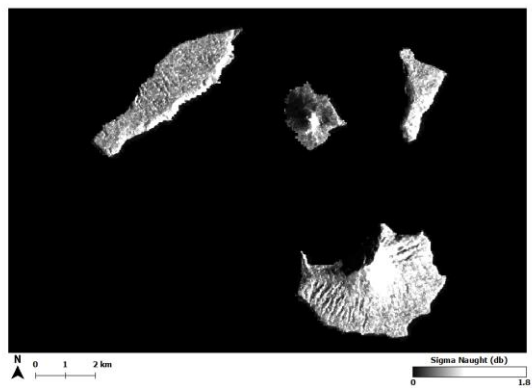


Figure 3-1: The eruption of Anak Krakatau Volcano, was captured and showed visually from Landsat-8 on 1 October 2018, composite false color RGB 654 (without pansharpen).



VH



VV

Figure 3-2: The sigma naught backscatter images derived Sentinel-1 TOPS acquisition date 17 September 2018 with VH and VV polarization.

The data fusion of Landsat-8 optical and Sentinel-1 TOPS SAR were used to observe the eruption activities and lava flow deposits resulted from the eruption. The morphology of Krakatau Complex, volcanic ash, pyroclastics, and lava flow deposits were analyzed based on the fusion images.

The eruption of Anak Krakatau Volcano, was captured and showed visually from Landsat-8 on 1 October 2018, composite false color RGB 654 (without pansharpen) (Fig. 3-1). Fig 3-2 showed the sigma naught backscatter images derived Sentinel-1 TOPS acquisition date 17 September 2018 with VH and VV polarization.

The fusion of Landsat-8 and Sentinel-1 are four fusion data sets, each of which is RGB-Intensity and RGB Brovey transformation for sigma naught backscatter VV ( $\sigma_{VV}^{\circ}$ ) and VH ( $\sigma_{VH}^{\circ}$ ). Figure 3-3 shows the results of the fusion of Landsat-8 and Sentinel-1 data on the Krakatau complex, just when the eruption occurred on October 1, 2018. Then, the Landsat-8 and Sentinel-1A fusion were compared with the images fusion of Landsat-8, band 6,5,4 and panchromatic band (band 8), with the same methods.

Based on the results of data fusion (Fig 3-3), it can be seen that the fusion of Landsat-8 and Sentinel-1 data using the RGBI-VV and Brovey RGB-VV methods provide the best results in accentuating lava deposits. These results have met the rules and objectives of data fusion, that are obtaining information of greater quality (Wald 1999), to form a unified picture (Khaleghi et al. 2013), and provide more reliable and accurate information (Luo et al. 2002).

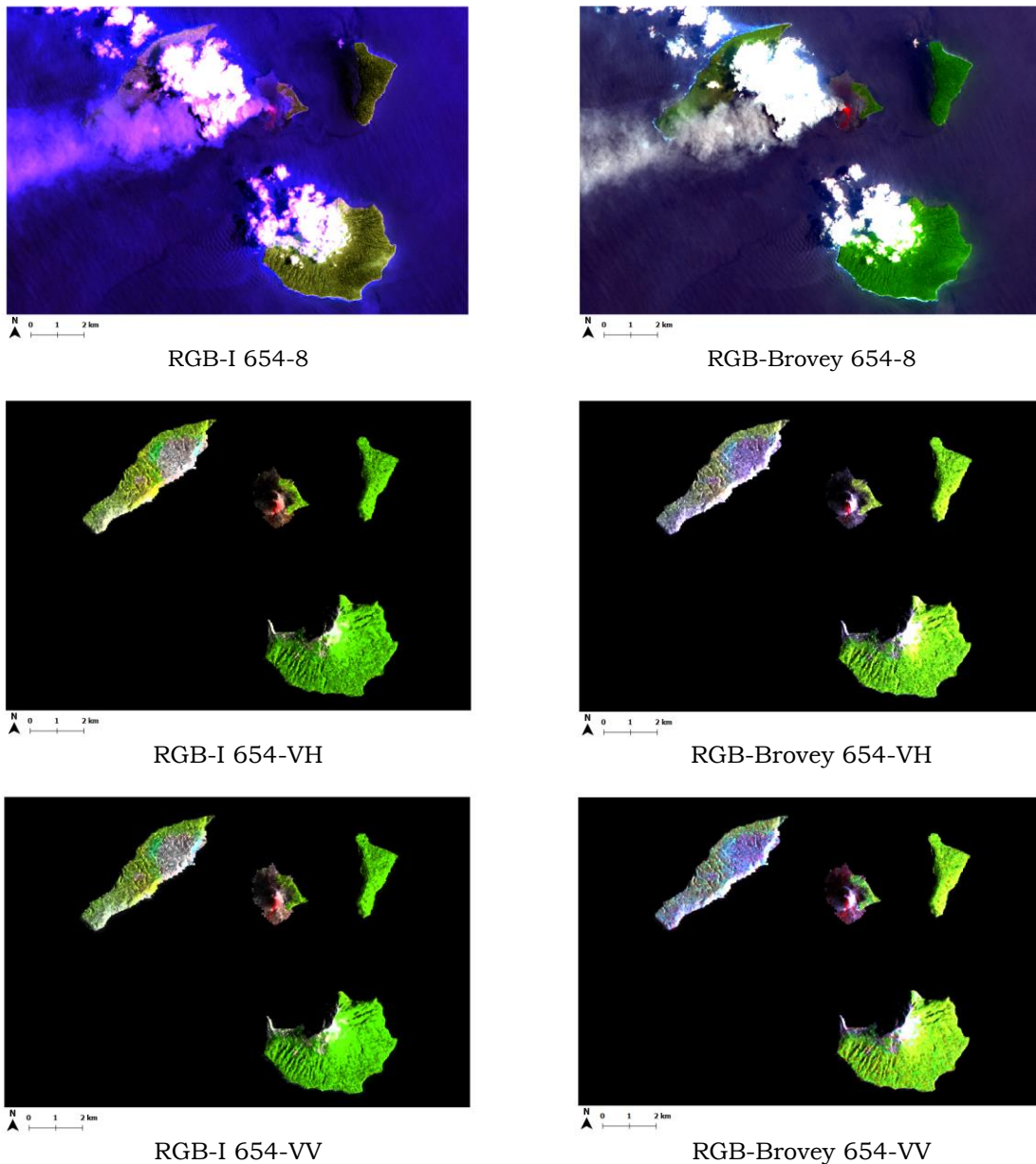


Figure 3-3: The results of fusion of Landsat-8 and Sentinel-1 data on the Krakatau complex with several methods. Red colors indicate the object of lava deposits.

Based on visual interpretation, it can be seen the presence of incandescent lava (appearing red), which flows down the southern slope. Previous lava deposits, appear to be dark brown, which predominantly spread towards the North, West and South slopes. The small portion of lava deposits are also exist on eastern slope. Based on observations of these images, it can be seen that the entire slopes of Anak Krakatau Volcano, with a radius of about 1 km from the crater, is an area prone to incandescent lava and pyroclastic falls. The direction of the

lava flow has the potential to spread in all directions.

#### 4 CONCLUSION

Optical Landsat-8 and Sentinel-1 SAR data fusion are able to sharpen the appearance of volcano morphology and lava flow deposits. Especially in the region, it is often constrained by cloud cover and volcanic ash, which occurs when the volcanic eruption. The RGBI-VV and Brovey RGB-VV methods provide better display quality results in revealing the morphology of volcanic cone and lava deposits. The entire

slopes of Anak Krakatau Volcano, with a radius of about 1 km from the crater, is an area prone to incandescent lava and pyroclastic falls. The direction of the lava flow has the potential to spread in all directions. It is hoped that the fusion of optical Landsat-8 and Sentinel-1 SAR data can be used continuously in monitoring the activity of Anak Krakatau volcano and other volcanoes in Indonesia both in cloudy and clear weather conditions.

### ACKNOWLEDGEMENTS

This paper is a part of the research activities entitled 'Development of Optical, SAR, LiDAR and / or GPS Data Fusion'. This research was funded by the Program of National Innovation System Research Incentive (INSINAS) in 2018, Ministry of Research Technology and the Higher Education Republic of Indonesia. Thank Mr. Suhermanto as the Group Leader in this activity and Dr. Mahdi Kartasasmita. Thank for the collegas from Remote Sensing Application Center of LAPAN, Remote Sensing Technology dan Data Center of LAPAN and Faculty of Mathematics and Natural Sciences who have provided suggestions for the discussion and suggestion. Thank also Dr. Hanik Humaida, Mr. Gede Suantika and Mr. Windi Cahya from Center for Volcanology and Geological Disaster Mitigation for discussion, collaboration, field surveys, and sharing information to support this research.

Sentinel-1 TOPS was provided by Alaska Satellite Facility. Landsat 8 OLI was provided by Remote Sensing Technology and Data Center, LAPAN. SRTM90 DEM was provided by the U.S. Geological Survey (USGS).

### REFERENCES

- Agustan, Kimata F., Pamitro YE, *et al.*, (2012), Understanding the 2007–2008 eruption of Anak Krakatau Volcano by combining remote sensing technique and seismic data. *International Journal of Applied Earth Observation and Geoinformation* 14:73-82.
- Chavez Jr. PR, (1996), Image-based atmospheric corrections - revisited and improved. *Photogrammetric Engineering & Remote Sensing* 62(9):1025-1036.
- Deplus C., Bonvalot S., Dahrin D., *et al.*, (1995), Inner structure of the Krakatau volcanic complex (Indonesia) from gravity and bathymetry data. *Journal of Volcanology and Geothermal Research* 64(1-2):23-52.
- Dörries M., (2003), Global science: the eruption of Krakatau. *Endeavour* 27(3), 113–116.
- Francis PW, (1985), The origin of the 1883 Krakatau tsunamis. *Journal of Volcanology and Geothermal Research* 25(3-4): 349–363.
- Ibs-von Seht M., (2008), Detection and identification of seismic signals recorded at Krakatau volcano (Indonesia) using artificial neural networks. *Journal of Volcanology and Geothermal Research* 176(4): 448–456.
- Irons JR, Dwyer JL, and Barsi JA, (2012), The next Landsat satellite: The Landsat Data Continuity Mission. *Remote Sensing of Environment* 122:11-21.
- Jensen JR, (2005), *Introductory digital image processing, a remote sensing perspective*. Pearson Prentice Hall. New Jersey.
- Khaleghi B., Khamis A., Karray FO, *et al.*, (2013), Multisensor data fusion: A review of the state-of-the-art. *Inform. Fusion* (14)1:28–44.
- Luo RC, Yih CC, and Lan Su K., (2002), Multisensor fusion and integration: Approaches, applications, and future research directions. *IEEE Sensors J.* 2(2):107–119.
- Martinez NY, Iraola PP, Gonzales FR, *et al.*, (2016), Interferometric processing of Sentinel-1 TOPS Data. *IEEE*

- Transactions on Geoscience and Remote Sensing 54(4):2220-2233.
- Periasamy S., (2018), Significance of dual polarimetric synthetic aperture radar in biomass retrieval: An attempt on Sentinel-1. *Remote Sensing of Environment* 217: 537-549.
- Rampino MR, and Self S., (1982), Historic eruptions of Tambora (1815), Krakatau (1883), and Agung (1963), their stratospheric aerosols, and climatic impact. *Quaternary Research* 18 (2): 127-143.
- Reulke R., Giaquinto,G., Giovenco *et al.*, (2013), Optics and radar image fusion based on image quality assessment. 2013 Seventh International Conference on Sensing Technology, IEEE: 690-696.
- Sutawidjaja IS, (1997), The activities of Anak Krakatau volcano during the years of 1992-1996. *Annals of the Disaster Prevention Research Institute* 40: 13-22.
- Sutawidjaja IS, (2006), Pertumbuhan Gunung Api Anak Krakatau setelah letusan katastrofis 1883. *Jurnal Geologi Indonesia* 1(3): 143-153.
- Torres R., Snoeij P., Geudtner D., *et al.*, (2012), GMES Sentinel-1 mission, *Remote Sensing of Environment* 120: 9-24.
- Wald L., (1999), Some terms of reference in data fusion. *IEEE Transactions on Geoscience and Remote Sensing* 37(3): 1190-1193.
- Zanter K. (Ed.), (2015), *Landsat 8 (L8) data users handbook, Version 1*. Sioux Falls, South Dakota: Department of the Interior, U.S. Geological Survey.



# GEOMETRIC ASPECTS EVALUATION OF GNSS CONTROL NETWORK FOR DEFORMATION MONITORING IN THE JATIGEDE DAM REGION

Made Ditha Ary Sanjaya<sup>1\*</sup>, T. Aris Sunantyo<sup>2</sup>, and Nurrohmat Widjajanti<sup>3</sup>

<sup>1</sup> Postgraduate Student at Geomatic Engineering, Engineering Faculty  
Universitas Gadjah Mada, Indonesia

<sup>2,3</sup>Lecturer at Geodetic Engineering Department, Engineering Faculty  
Universitas Gadjah Mada, Indonesia

\*E-mail: ditha.ary.sanjaya@gmail.com

Received: 2 February 2018; Revised: 14 March 2018; Approved: 6 December 2018

**Abstract.** Many factors led to dam construction failure so that deformation monitoring activities is needed in the area of the dam. Deformation monitoring is performed in order to detect a displacement at the control points of the dam. Jatigede Dam deformation monitoring system has been installed and started to operate, but there has been no evaluation of the geometry quality of control networks treated with IGS points for GNSS networks processing. Therefore, this study aims to evaluate the geometric quality of GNSS control networks on deformation monitoring of Jatigede Dam area. This research data includes the GNSS measurements of five CORS Jatigede Dam stations (R01, GG01, GCP04, GCP06, and GCP08) at doy 233 with network configuration scenarios of 12 IGS points on two quadrants (*jat1*), three quadrants (*jat2*), and four quadrants (*jat3* and *jat4*). GNSS networks processing was done by GAMIT to obtain baseline vectors, followed by network processing using parameter method of least squares adjustment. Networks processing with least squares adjustment aims to determine the most optimal by precision and reliability criterion. Results of this study indicate that network configuration with 12 IGS stations in the two quadrants provides the most accurate coordinates of CORS dam stations. Standard deviations value of CORS station given by *jat1* configuration are in the range of 2.7 up to 4.1 cm in X-Z components, whereas standard deviations in the Y component are in the range 5.8 up to 6.9 cm. An optimization assessment based on network strength, precision, and reliability factors shows optimum configuration by *jat1*.

Keywords: *Jatigede dam, control network, IGS, GNSS*

## 1 INTRODUCTION

Jatigede Dam is built on Baribis Thrust which is an intensive and complex tectonic geological structure that causes the level of the dam vulnerability to movement and landslide is increasing (Zakaria, *et al.*, 2011).

Based on the Center for Volcanology and Geological Hazard Mitigation in 2006, Baribis Fault is one of the active faults that potentially produce devastating earthquakes and is in the zone VII of Indonesia's area earthquake prone (Zakaria, *et al.*, 2011).

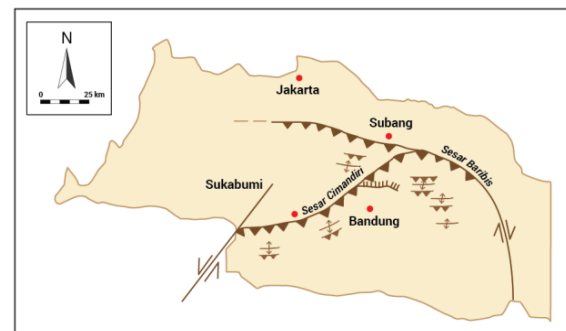


Figure 1-1: Regional Baribis-Cimandiri thrust in West Java (Haryanto, 2001).

One of the efforts to maintain safety of dam construction is to monitor the geometric aspects of the dam

deformation. Deformation monitoring is an effective method for analyzing deformation characteristics that occurred in the dam area, and also capable to provide warning systems when there are abnormal symptoms of dams (Cetin, et al., 2000).

Dam deformation monitoring is conducted by using integration of several interrelated disciplines. Geodetic science can contribute in position data recording techniques which used to create an integrated detection system and movement monitoring that occur to dam using permanently installed multi sensors in dam areas. Geodetic sensors implemented are Global Navigation Satellite System (GNSS) and Robotic Total Station (RTS) that work in accordance with their respective functions. Furthermore, the sensor's measurement data are integrated into a system so it could be accessed for practical and scientific purposes (Sunantyo, et al., 2012).

According to Kuang (1991), one of the major aspects of deformation monitoring is geodetic observation network optimization. Optimal means that the control network condition have satisfied the precision quality standards. Control network optimization could be assessed by monitoring observational data of deformation and controlled by IGS point observation data in some IGS distribution scenarios in the quadrant (Nursetiyadi, 2015). Selection of GPS networks with a good strength of figure and satisfied the reliability criteria are required to achieve optimal position accuracy (Lestari and Yulaikhah, 2013). To obtain good GNSS network geometry, constraining to IGS active stations is needed (Panuntun, 2012; Artini, 2014; and Nursetiyadi, 2015). GNSS network processing is necessary to select an equally distributed IGS stations by data quality, data availability, and good

network configuration to obtain precise and consistent station coordinate (Ma'ruf and Rahman, 2008).

Determination of the optimal network monitoring should be done before the installation of monitoring sensors deformation, but the assessment of network optimization remains to be done after the installation of the equipment. Quality assessment of GNSS network is necessary due to the importance of Jatigede Dam. An assessment of geometrical aspect qualities on Jatigede dam monitoring network was done by processing the observation data of GNSS stations and involving the observation data of IGS stations. The quality assessment of GNSS and IGS control network configuration scenarios were conducted by precision and reliability aspects of the network.

## 2 MATERIALS AND METHODOLOGY

### 2.1 Data and Tools

Data used in this study were GNSS measurements of five CORS Jatigede Dam stations (R01, GG01, GCP04, GCP06, and GCP08) at *day* 233 with a network configuration scenario of 12 IGS points on two quadrants (*jat1*), three quadrants (*jat2*), and four quadrants (*jat3* and *jat4*). Other data involved in this study is the observation of 18 IGS points for each configuration on 20 August 2016 (*day* 233).

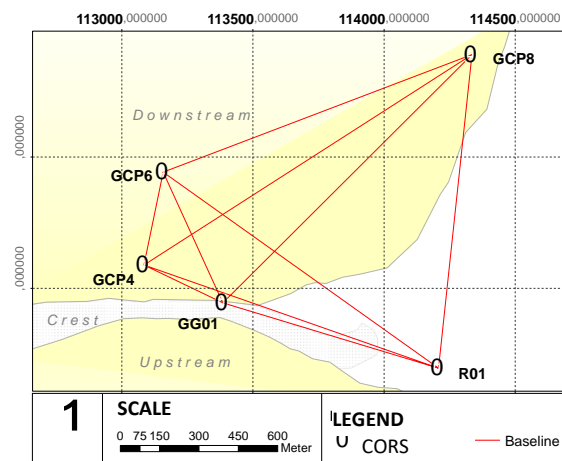


Figure 2-1: Jatigede Dam GNSS control network.



**2.2 Methods**

Evaluation of control network was carried out on the scenario of GNSS network configurations in the Jatigede Dam Area by involving IGS stations. GNSS networks were processed by the principle of least squares adjustment to obtain the coordinate values of CORS station coordinates, as well as variance-covariance of parameters and observations to compute the precision and reliability of network.

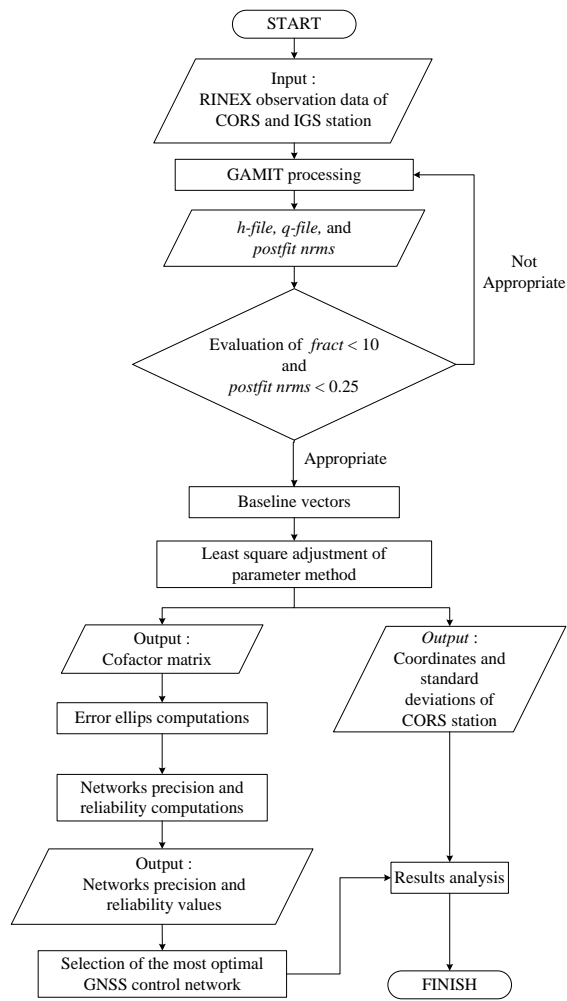
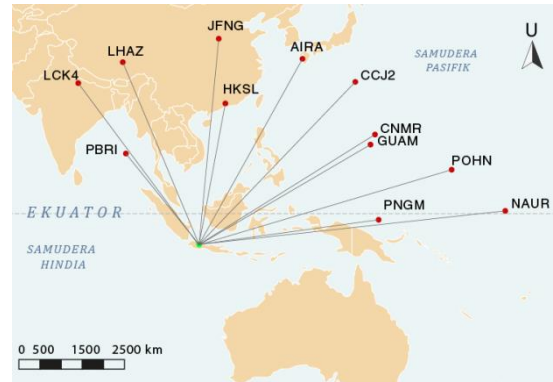
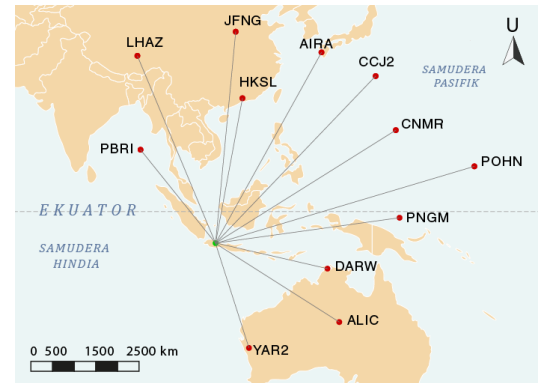


Figure 2-2: Research workflow.

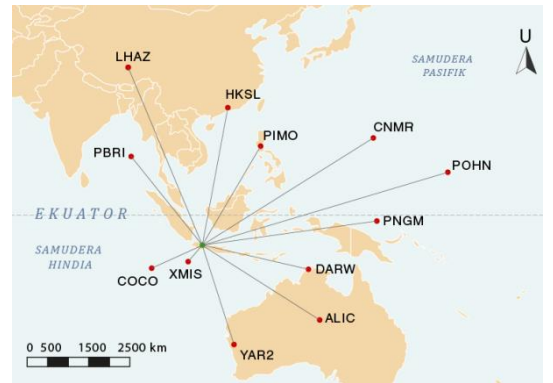
Figure 2-2 shows that GNSS network processing initiated by IGS network establishment to four network configurations consists of 12 IGS points on each network. Network configuration was designed on horizontal projection plane with the division of the quadrant as in Figure 2-3.



(a)



(b)



(c)



(d)

Figure 2-3: Network configuration *jat1* (a), *jat2* (b), *jat3* (c), and *jat4* (d)

Network configurations in Figure 2-3 are *jat1*, *jat2*, *jat3*, and *jat4*. *Jat1* network was established based on IGS position in two quadrants at the north of dam area. *Jat2* network was designed



based on IGS position in three quadrants. *Jat3* and *jat4* networks was designed based on IGS position in four quadrants.

GNSS configuration networks was followed by quality checking of CORS station observation data with TEQC. TEQC has main functions to translate, edit, and check observation data quality. Data that has been checked with TEQC is prepared for data processing with GAMIT. GAMIT processed uses least squares adjustment to determined estimate position of GNSS station, orbit and rotation parameters, and phase ambiguity (Lestari, 2006). This process produced network baselines vectors and the quality parameter of *postfit nrms* and *fract*.

Baseline vectors that has been generated from GAMIT processing were used in the least squares adjustment parameter method of the control network to obtain coordinate values and precision of each station in dam area. Least squares adjustment parameter method was used to determining information or measurements of the parameter from geodetic observation data. Processing with least squares adjustment was done by determining amount of measurements (baseline), amount of parameters, and weight of the measurements.

Least squares adjustment computation was initiated by determining amounts of measurement (baseline) and amount of parameters of *jat1*, *jat2*, *jat3*, and *jat4*. The amount of measurements generated from each configuration is 210 baselines ( $\Delta X_1, \Delta Y_1, \Delta Z_1, \Delta X_2, \Delta Y_2, \Delta Z_2, \dots, \Delta X_{70}, \Delta Y_{70}, \Delta Z_{70}$ ). Formation of weight matrix was performed based on the standard deviation value of the baseline measurement between the CORS dam control station and IGS points. The adjustment process yields the desired parameter value ("X" matrix), residual value (matrix "V"), corrected measurement value ("Lb" matrix).

Equation of measurement is computed by using mathematical relationship between parameter of measurement (approached coordinate) and observed value (baseline vector) such as (2-1) up to (2-3):

$$\Delta_{Xij} + v_1 = X_j - X_i \quad (2-1)$$

$$\Delta_{Yij} + v_1 = Y_j - Y_i \quad (2-2)$$

$$\Delta_{Zij} + v_1 = Z_j - Z_i \quad (2-3)$$

$\Delta_{Xij}$ ,  $\Delta_{Yij}$ , and  $\Delta_{Zij}$  are baseline vector of point *i* to *j*,  $v_1$  are residual value, and  $X_n, Y_n$ , and  $Z_n$  are coordinate values. The output is the coordinate value and precision of each control station in the dam area.

Quality of GNSS network configuration can be seen on 2D precision represented by absolute error ellipse. Absolute error ellipse computation was computed using standard deviation values of CORS coordinates using equations (2-4) and (2-5).

$$\sigma_{max}^2 = \frac{1}{2} \left[ \sigma_x^2 + \sigma_y^2 + \sqrt{(\sigma_x^2 - \sigma_y^2)^2 + 4\sigma_{xy}^2} \right] \quad (2-4)$$

$$\sigma_{min}^2 = \frac{1}{2} \left[ \sigma_x^2 + \sigma_y^2 - \sqrt{(\sigma_x^2 - \sigma_y^2)^2 + 4\sigma_{xy}^2} \right] \quad (2-5)$$

$\sigma_{max}$  is semi major axis,  $\sigma_{min}$  is semi minor axis, and  $\sigma_x^2, \sigma_y^2$  are variance of eigen value from variance-covariance of random vector matrix.

Network configurations quality also can be represented in network strength factor by considering the correlation between baseline vector component of GNSS network. Computation network strength factor in equation (2-6) was completed by the variance-covariance of parameters matrix that shows the influence of the configuration strength of network as deformation monitoring objective.

$$\text{Network strength factor} = \frac{\text{trace}(A^T C_L^{-1} A)^{-1}}{u} \quad (2-6)$$

$Trace(A^T C_L^{-1} A)^{-1}$  is summation of diagonal components of  $(A^T C_L^{-1} A)^{-1}$  matrix, and  $u$  is ammount of parameters.

GNSS network precision and reliability were computed based on variance-covariance matrix of coordinates that had been generated from least squares adjustment. Precision criterion is performed by analysis of scalar function optimization criteria of A-optimality, D-optimality, and E-optimality. Computation of GNSS network optimization criteria of precision and reliability is completed by scalar function of network accuracy that are A-optimality, D-optimality, and E-optimality of eigen values for each configuration (Grafarend, 1974) are shown in equation (2-7) to (2-9).

**A-optimality**

$$trace(\sum xx) = \lambda_1 + \lambda_2 + \dots + \lambda_n = \min \quad (2-7)$$

**D-optimality**

$$Det(\sum xx) = \lambda_1 \times \lambda_2 \times \dots \times \lambda_n = \min \quad (2-8)$$

**E-optimality**

$$\lambda_{maks} = \min \quad (2-9)$$

$\lambda_1, \lambda_2, \dots, \lambda_n$  are eigen value of matrix  $\sum xx$ , and  $\lambda_{maks}$  are maximum eigen value from  $\sum xx$  matrix.

Network reliability analysis is completed by computations of individual redundancy value, internal reliability and external reliability. In accordance to Yalcinkaya and Teke (2006), the reliability of the control network is computed by equation (2-10) to (2-12).

**Individual redundancy**

$$Z = r_j = (Q_{VV})_j P_j \quad (2-10)$$

$Q_{VV}$  is cofactor matrix of the residuals,  $P$  is weight matrix of the observations, and  $r_j$  is individual redundancy value.

**Internal reliability**

$$Z = |\Delta_{0j}| = m_0 \sqrt{\frac{w_0}{p_j r_j}} \quad (2-11)$$

$m_0$  is standard deviation of unit weight,  $w_0$  is lower bound for the non-centrality parameter in dependency of the significance level ( $\alpha_0$ ) and the required minimum power of the test ( $1-\beta_0$ ), and  $\Delta_{0j}$  is internal reliability criterion.

**External reliability**

$$Z = \delta_{0j}^2 = \frac{1-r_j}{r_j} w_0 \quad (2-12)$$

$\delta_{0j}^2$  is external reliability criterion.

**3 RESULTS AND DISCUSSION**

**3.1 GAMIT Processing Result**

GAMIT processing resulted based on quality parameters of the process. There are *postfit nrms* and *fract* values. *Fract* values are shown in Figure 3-1 and *postfit nrms* values are shown in Figure 3-2.

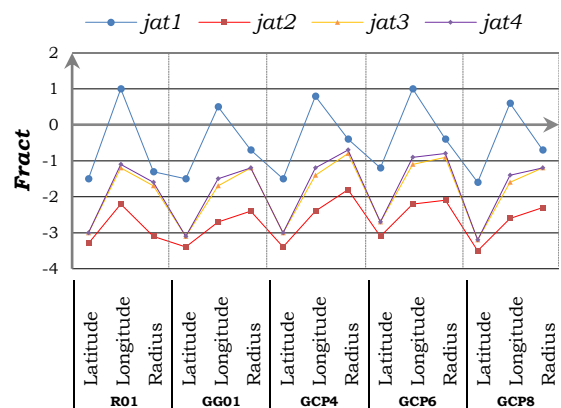


Figure 3-1: Visualization of *fract* values for each CORS stations.

Figure 3-1 shows *fract* values visualization for five stations in four IGS network configurations. *Fract* values were accepted if the value was less than 10. Figure 3-1 also explains variation of *fract* values were similar on each CORS. *Jat3* and *jat4* network configurations show relatively identical graph considering both networks were designed in four quadrants. *Jat3* and *jat4* configurations produce nearest value to zero in longitude and radius components of *fract*.

Table 3-1: Example of baseline vectors and their standard deviations.

No.	Baseline	$\Delta X$ (m)	$\Delta Y$ (m)	$\Delta Z$ (m)	$\sigma_{\Delta X}$ (cm)	$\sigma_{\Delta Y}$ (cm)	$\sigma_{\Delta Z}$ (cm)
1.	GCP4 to GCP6	-87.62512	34.02835	349.32539	0.722	1.753	0.467
2.	GCP4 to GCP8	-1233.52942	-248.05762	790.88403	0.747	1.813	0.483
3.	GCP4 to GG01	-290.80514	-77.19233	-146.75211	0.787	1.848	0.484
4.	GCP4 to R01	-1069.1076	-345.08832	-395.18543	0.755	1.800	0.479
5.	GCP6 to GCP8	-1145.9043	-282.08597	441.55864	0.58	1.413	0.374

Fract values indicated the absence of gross error. Fract also indicated that apriori coordinate values were appropriate and given constraints were correct.

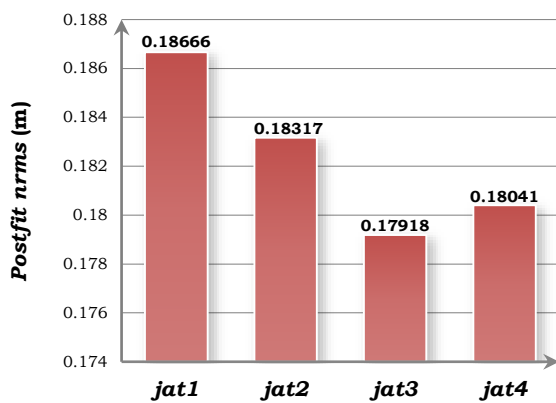


Figure 3-2: Postfit nrms values for each network configuration.

Figure 3-2 visualizes postfit nrms values for entire configurations of control networks. Postfit nrms values are acceptable if the value was less than 0.25 (Herring, et al., 2006). The overall postfit nrms value are smaller than 0.25 that indicate the absence of cycle slips effects that have not been omitted. The smallest postfit nrms values are in jat3 network that consist of IGS points deployment on four quadrants, while the highest postfit nrms value was in the jat1 network that consist of IGS points deployment on two quadrants.

GAMIT processing resulted by baseline vector values between GNSS stations and their standard deviations. Generated baselines were used for least squares adjustment, whereas their standard deviations were used as weight of measurements. Some baseline vectors and their standard deviation values of each baseline were shown in Table 3-1. Table 3-1 shows the baseline vectors results of network processing by GAMIT and their standard deviations. Standard deviation value of baseline vectors is in fraction of millimeter up to a centimeter.

### 3.2 Least Squares Adjustment Result

Least squares adjustment computation generated CORS coordinates estimation and their standard deviations. Standard deviations of CORS coordinates are shown in Figure 3-3.

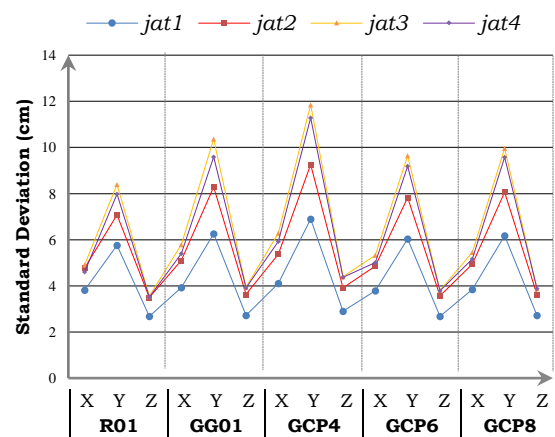


Figure 3-3: Visualization of standard deviations of CORS coordinates.

Based on standard deviations in Figure 3-3, *jat1* is network with highest coordinate precision compared to network configurations with IGS positions in four quadrants (*jat3* and *jat4* configuration). *Jat3* network shows widest range of standard deviations precision of 3.552 cm up to 11.86 cm, while *jat1* network has the smallest standard deviation range of 2.681 cm up to 6.903 cm. The Y component on the graph has a relatively high standard deviation values. Highest standard deviation that shown in Y component shows lowest precision among other components. X and Z components on each CORS had high precision with standard deviation value below 8 cm in each configuration. *Jat1* network shows highest coordinate precision compared to network configurations with IGS positions in four quadrants (*jat3* and *jat4*).

**3.3 Absolute Error Ellipse of GNSS Network Result**

Error ellipse was computed to represent 2D precision of each network configurations. Error ellipse results are presented in Table 3-2. Table 3-2 shows position precision of point represented by  $\sigma_{min}$  and  $\sigma_{max}$  values on the X and Y axes on networks. Value of  $\sigma_{min}$  and  $\sigma_{max}$  ellipse error have precision in centimeter fraction. Based on Table 3-2, *jat1* configuration was the network with smallest ellipse error among other configurations. Ellipse error values of

each configurations are shown in centimeter fraction. Based on network purpose of detecting deformation in very small size, ellipse error values were still quite large. Network with a smaller ellipse error was needed as another strategy to obtain optimal deformation monitoring network.

**3.4 Network Strength Factor Computation Result**

Network strength factor is determined by the variance-covariance matrix. If the value of the network power factor is small, then the network is said to have good quality and vice-versa. The network strength factor results is shown in Table 3-3.

Tabel 3-3: Network strength factor of GNSS network configuration.

No.	Network Configuration	Network Strength Factor
1.	<i>jat1</i>	1.29 x 10 <sup>-7</sup>
2.	<i>jat2</i>	2.68 x 10 <sup>-7</sup>
3.	<i>jat3</i>	1.50 x 10 <sup>-7</sup>
4.	<i>jat4</i>	2.86 x 10 <sup>-7</sup>

Based on Table 3-3, it can be seen that configuration with IGS points in the four quadrants has a high dependence on the geometry of treated IGS network to CORS coordinates precision. Long distances between Dam GNSS control network and IGS locations are the factors that network geometry of IGS points in a particular quadrant determine the value of network strength factor. This makes *jat1* configuration with IGS points in the two quadrants is the best configuration.

Tabel 3-2: Ellipse error of GNSS network.

GNSS Station	<i>jat1</i>		<i>jat2</i>		<i>jat3</i>		<i>jat4</i>	
	$\sigma_{max}$ (cm)	$\sigma_{min}$ (cm)	$\sigma_{max}$ (cm)	$\sigma_{min}$ (cm)	$\sigma_{max}$ (cm)	$\sigma_{min}$ (cm)	$\sigma_{max}$ (cm)	$\sigma_{min}$ (cm)
R01	5.768	3.823	7.082	4.770	8.395	4.921	7.985	4.609
GG01	6.254	3.927	8.286	5.113	10.36	5.783	9.593	5.401
GCP4	6.903	4.109	9.264	5.375	11.86	6.286	11.29	5.926
GCP6	6.036	3.793	7.826	4.856	9.643	5.328	9.192	5.007
GCP8	6.182	3.842	8.066	4.936	9.96	5.458	9.57	5.162

*Jat1* configuration is the best network in terms of dependence on IGS geometry because of the minimum network strength factor value that is  $1.29 \times 10^{-7}$ .

### 3.5 Precision and Reliability of GNSS Network

Analysis results of scalar function. This research used analysis results of scalar function optimization from criterion of precisions of A-optimality, D-optimality, and E-optimality. The minimum value on each computed precision criteria shows the best GNSS network quality among configurations. Values of network precision computation were shown in Table 3-4.

Tabel 3-4: Network configuration precision value.

Precision Function	<i>jat1</i>	<i>jat2</i>	<i>jat3</i>	<i>jat4</i>
A-optimality	$3.08 \times 10^{-2}$	$5.23 \times 10^{-2}$	$7.43 \times 10^{-2}$	$6.73 \times 10^{-2}$
D-optimality	$9.19 \times 10^{-44}$	$8.39 \times 10^{-40}$	$1.01 \times 10^{-37}$	$2.84 \times 10^{-38}$
E-optimality	$6.42 \times 10^{-3}$	$9.99 \times 10^{-3}$	$1.52 \times 10^{-2}$	$1.38 \times 10^{-2}$

Table 3-4 represents the optimization criteria of the network from homogeneity and isotropy aspect of the configuration. The minimum A-optimality value was in *jat1* configuration with value of  $3.08 \times 10^{-2}$ , and maximum value was in *jat3* configuration with value of  $7.43 \times 10^{-2}$ . The A-optimality value indicated the homogeneity of a configuration so that *jat1* network was the best in terms of baseline homogeneity. The *jat1* network has relatively long baselines compared to *jat3* or *jat4* networks that has heterogeneous baseline length although *jat3* or *jat4* were established with IGS points deployment on four quadrants. Minimum value of D-optimality was found in *jat1* configuration with value of  $9.19 \times 10^{-44}$ , while the maximum value was in the *jat3* configuration with a value of  $1.01 \times 10^{-37}$ . E-optimality criteria of *jat1* configuration shows lowest value of

$9.69 \times 10^{-3}$ , whereas the *jat3* configuration has the highest value of  $1.52 \times 10^{-2}$ . The minimum D-optimality value represents the isotropic configuration, that showed the network physical character in all directions.

Individual redundancy value indicated an unreliable measure of gross errors in network processing (Kuang, 1991). Individual redundancy value was derived from the diagonal element of residual cofactor matrix that has been generated by least squares adjustment. Individual redundancy for network baselines on average between the CORS on each configuration visualized in Figure 3-4.

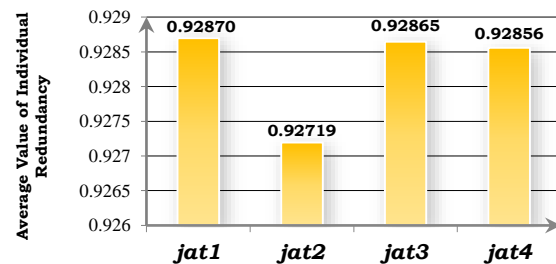


Figure 3-4: Average individual redundancy.

Figure 3-4 shows individual redundancy values of network configuration. Network have satisfied the criterion of critical value that was greater than 0.4. *Jat1* configuration has the highest average individual redundancy compared to *jat2*, *jat3*, and *jat4* networks. Figure 3-4 shows that *jat1* network was the most optimal network considering the individual redundancy aspect. This result implied that *jat1* network has the best ability to detecting small gross errors in network processing.

Internal reliability of control network illustrates the quality that refers to the minimum limit of gross errors that can be detected on numerous observations for the given probability value of error (Kuang, 1991). Internal reliability has critical value of less than  $6\sigma_j$  that expressed by Marginally Detectable Error (MDE). Internal

reliability computation of GNSS network baselines visualized in Figure 3-5.

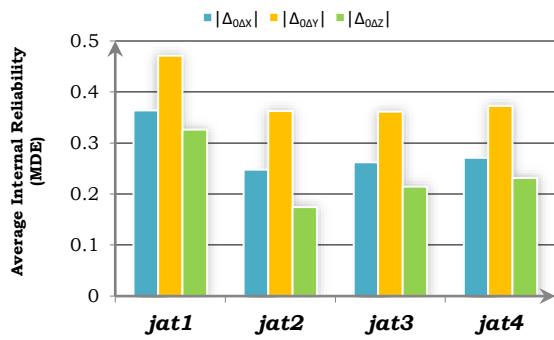


Figure 3-5: Average internal reliability value.

Figure 3-5, shows average values of networks internal reliability of each baseline components. Maximum reliability value is shown in Y ( $|\Delta_{0\Delta Y}|$ ) component, while the minimum reliability value is shown in component Z ( $|\Delta_{0\Delta Z}|$ ). Configuration with maximum internal reliability value indicates low sensitivity to gross error. The maximum value of internal reliability shows less reliable observation, while the minimum reliability value indicates high sensitivity to gross errors. Visualization of internal reliability shows that most reliable network configuration is *jat1* network.

External reliability of networks referred to results of individual redundancy computation. In this study, the expected external reliability value was above the critical value of less than 6. This value was expressed in Bias to Noise Ratio (BNR). Results of external reliability computation on GNSS network baselines are visualized in Figure 3-6.

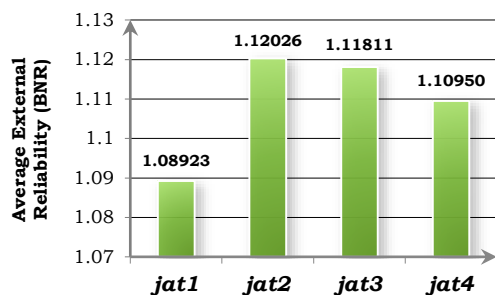


Figure 3-6: Average external reliability value.

Based on Figure 3-6, it can be seen the average value of external reliability of each baseline components on each GNSS networks. Computation of average external reliability on entire components shows that *jat1* network produced the lowest average value compared to the configuration of *jat2*, *jat3*, and *jat4*. The graph shows that the *jat1* network has the smallest effect that has been caused by the presence of an undetectable random error on GNSS observations in network processing.

#### 4 CONCLUSION

GNSS network configurations with IGS positions in two quadrants (*jat1*) is the highest precision network based on estimated coordinates. Utilization of IGS stations in network processing was able to generate precision on X and Z components in the range of 2.7 up to 4.1 cm, while on the Y component the precision is in the range 5.8 up to 6.9 cm.

Optimization assessment of GNSS network configurations shows that Jatigede CORS network is precise and reliable for deformation monitoring by network processing with deployment of IGS station data in *jat1* configuration. Configuration of 12 IGS stations in two quadrants (*jat1*) produced the best network based on network strength, precision, and reliability. *jat1* configuration is able to generate minimum value on network strength factor and external reliability while providing maximum value on individual redundancy values. This result shows that network processing of network that established by IGS stations deployment on two quadrants is more optimal than network processing of network that established by IGS stations deployment on of three and four quadrants (*jat3* and *jat4*).

## ACKNOWLEDGEMENTS

The authors would like to "Satuan Kerja Non Vertikal Tertentu" of Jatigede Dam dan Leica Geosystems Indonesia for helping this research. The authors thank all the parties who helped provide advices and assistances during the implementation of research.

## REFERENCES

- Artini, SR, (2014), GNSS CORS GMU1 Stations Positioning with Global and Regional GPS Control Point Combinations, PILAR Jurnal Teknik Sipil, 10(1), Yogyakarta.
- Cetin, H., Laman, M., and Ertunc, A., (2000), Settlement and Slaking Problems in the World's Fourth Largest Rock-Fill Dam, the Ataturk Dam in Turkey, *Engineering Geology*, 56, pp. 225-242.
- Grafarend, EW, (1974), Optimization of Geodetic Networks, *Bolletino di Geodesia a Science Affini*, pp. 351-406.
- Haryanto, I., (2004), Tectonic Baribis-Cimandiri Fault, *Annual Proceedings IAGI* 33.
- Herring, TA, King, RW, and McClusky, SC, 2006, Introduction to GAMIT/GLOBK, Department of Earth, Atmospheric, and Planetary Science, Massachusetts Institute of Technology.
- Kuang, S., (1991), Optimization and Design of Deformation Monitoring Schemes, Dissertation, Department of Surveying Engineering Technical Report No.157, University of New Brunswick, Fredericton, New Brunswick, Canada, pp. 179.
- Lestari, D., and Yulaikhah., (2013), Optimization of Horizontal Control Network Based on the Requirements of the Criteria Matrix for Geodynamic Studies in Opak River Faults, Research DPP of Vocational Schools, Gadjah Mada University.
- Lestari, D., (2006), GPS Study for Resolving the Stability of Borobudur Temple Site, Thesis, School of Surveying and Spatial Information System, University of New South Wales.
- Ma'ruf, B., and Rahman, M. A., (2009), Analysis of Baseline-per-baseline Baseline Processing and Session-per-sessions Techniques on GPS Network Adjustment, National Seminar on Data Revitalization Yogyakarta.
- Nursetiyadi, R., (2015), The Effect of IGS Network Geometric to The Accuracy of Sangihe's Islands Geodinamic Monitoring Points at Epoch, Undergraduate Thesis, Geodetic Engineering Department, Universitas Gadjah Mada, Yogyakarta
- Panuntun, H., (2012), Determination of Offshore Platforms' Coordinates using Regional And Global Reference Points, Thesis, Geomatic Engineering Study Program, Universitas Gadjah Mada, Yogyakarta.
- Sunantyo, TA, Suryolelolo, KB, Djawahir, F., Swastana, A., Darmawan, A., and Adityo, S., (2012), Design and Installation for Dam Monitoring using Multi Sensors : a Case Study at Sermo Dam, Yogyakarta, Indonesia, FIG Working Week, pp. 6-10.
- Yalçinkaya and Teke, 2012, Strategy for Designing Geodetic GPS Networks with High Reliability and Accuracy, Hal 2-3.
- Zakaria, Z., Ismawan, and Haryanto, I., (2011), Identification and Mitigation in the Earthquake Prone Zone in West Java. *Bulletin of Scientific Contribution*, 9(1), pp. 35-41.



# PRELIMINARY STUDY OF HORIZONTAL AND VERTICAL WIND PROFILE OF QUASI-LINEAR CONVECTIVE UTILIZING WEATHER RADAR OVER WESTERN JAVA REGION, INDONESIA

Abdullah Ali<sup>1</sup>, Rirls Adriyanto, and Miming Saepudin

Remote Sensing Data Management Division, Center for Public Weather Services  
Indonesia Agency for Meteorology, Climatology and Geophysics (BMKG)

<sup>1</sup>E-mail: alibinakhsan@gmail.com

Received: 1 December 2018; Revised: 2 January 2019; Approved: 4 January 2019

**Abstract.** One of the weather phenomena that potentially cause extreme weather conditions is the linear-shaped mesoscale convective systems, including squall lines. The phenomenon that can be categorized as a *squall line* is a convective cloud pair with the linear pattern of more than 100 km length and 6 hours lifetime. The new theory explained that the cloud system with the same morphology as squall line without longevity threshold. Such a cloud system is so-called *Quasi-Linear Convective System* (QLCS), which strongly influenced by the ambient dynamic processes, include horizontal and vertical wind profiles. This research is intended as a preliminary study for horizontal and vertical wind profiles of QLCS developed over the Western Java region utilizing Doppler weather radar. The following parameters were analyzed in this research, include direction pattern and spatial-temporal significance of wind speed, divergence profile, vertical wind shear (VWS) direction, and intensity profiles, and vertical velocity profile. The subjective and objective analysis was applied to explain the characteristics and effects of those parameters to the orientation of propagation, relative direction, and speed of the cloud system's movement, and the lifetime of the system. Analysis results showed that the movement of the system was affected by wind direction and velocity patterns. The divergence profile combined with the vertical velocity profile represents the inflow which can supply water vapor for QLCS convective cloud cluster. Vertical wind shear that effect QLCS system is only its direction relative to the QLCS propagation, while the intensity didn't have a significant effect.

Keywords: *horizontal and vertical wind profile, QLCS, doppler weather radar, Western Java Region, Indonesia*

## 1 INTRODUCTION

The line-shaped convective system often associated with a significant weather event, both wind field and rainfall. Terms of squall line often used is referenced to Maddox (1980) definitions, linear type of convective system that persist more than 6 hours. Referring to that definition, the tropical convective system may not meet those lifetime criteria even has a line-shaped. A new terminology described by Lombardo and Colle (2010) concerning the line-shaped convective system by taking only on the

size, and the length-width ratio of the convective cloud, as Quasi-Linear Convective System (QLCS). A convective cloud of QLCS defined by weather radar reflectivity as 30 dBZ or more and 50 dBZ embedded. Minimum length is 50 km with 5:1 ratio of length and width of a convective cloud. Since it's still a line-shaped convective system, physical behaviour that triggers its formation and a decaying process can be referred to the squall line (Lombardo 2012).

Since dynamical process (horizontal and vertical wind profile) play more



prominent role in QLCS formation and evolution than its thermodynamic process (Lericos *et al.* 2007), it becomes important to do a research about horizontal and vertical wind profile occurring in QLCS, moreover, it often persists just in a short period of time. In the previous research of the convective line system, Houze (2004) explain that a divergence pattern captured in the stratiform cloud, and in an opposite, convergence patterns occur over the leading edge. Another aspect that plays important roles in QLCS evolution is vertical wind shear that lead to the new cell formation along the line due to cold pool behaviour (Thorpe *et al.* 1982; Rottuno *et al.* 1988; Parker and Johnson 2000; Weissman and Rotunno 2004; Cohen *et al.* 2007). Vertical wind shear profile at the level 0-3 km and 3-6 km gives significant effect to QLCS evolution (Lombardo and Colle 2012).

The difference between mid-latitude and tropical weather system make this investigation important. Horizontal field analysis will be done in the aspect of wind speed and direction relative to the linear system, and divergence profile. Vertical wind shear and vertical velocity are considered as important aspects to be analysed in the vertical direction. This research is expected to provide characteristic of horizontal and vertical wind profile on the occurrence of QLCS in Indonesia, so the forecaster in operational work can obtain more information about the formation and evolution of QLCS, and its characteristics can be taken into consideration in issuing early warning of damaging wind together with heavy rainfall due to QLCS.

## 2 MATERIALS AND METHODOLOGY

Doppler weather radar is used as the main tool to obtain the horizontal and vertical wind profile in analysing all QLCS occurrence. The total number of 34 QLCS events in the 2015-2016 period were

analysed without considering the seasonal factor since Indonesia has only two seasons.

QLCS observed by the Lombardo criteria in MAX product, length-width ratio measured by the distance measurement tool in every edge of its linear convective. Every evolution stage and its duration are defined by the theory of convective system as revealed by Tjasyono (2008). Universal Wind Technique (UWT) algorithm is used to analyse the wind speed and direction overlaid into reflectivity pattern and continued by the analysis for the spatial and temporal change relative to the convective line. Divergence, vertical wind-shear, and vertical velocity profile obtained from Vertical Velocity Processing (VVP) algorithm.

Horizontal divergence profile is presented in the vertical direction and analysed for its dominance in the formation, mature, and dissipating stage. This way of analysis is also done in a vertical velocity profile. Both divergence and vertical velocity are intended to find out the role of updraft in the mature stage, and how downdraft will affect the dissipating process. Vertical wind shear profile is analysed in the interval of 1-3 km correlating its value with each QLCS lifetime, and its direction to the propagation direction. In accordance to the theory revealed by Chaudari (2010), the longer convective system lifetime, the more significant vertical wind shear value. Perpendicular vertical wind shear direction to the elongated system often encountered (COMET 2013).

## 3 RESULTS AND DISCUSSION

The radial velocity data at the lowest elevation (0.5°) was processed using the UWT algorithm which was then combined with the radar dBZ data to determine the direction profile and wind speed in each QLCS segment. The lowest elevation is

used to get a lower layer wind profile that has the most direct impacts on the environment. The wind speed and direction are analysed relative to the direction of propagation of QLCS subjectively and objectively. Relative wind speed and direction analysis will be focused on the growing stage, the mature stage (when QLCS forms a linear pattern), and the decaying stage. The result of the analysis is then used to analyse the effect on the movement of the system (stationary or fast-moving).

In the growing stage, 9 cases showed a parallel (Figure 3-1a) and 13 cases with perpendicular (Figure 3-1b) wind direction pattern toward the QLCS propagation across all segment, while 8 cases with combined parallel and perpendicular wind direction patterns in different segments (Figure 3-1c). Different segment here means perpendicular direction located along the centred segment, while parallel direction occurs in both flank segment. In the mature stages, 7 cases show a parallel, 11 cases of perpendicular, and 12 cases combined parallel and perpendicular wind pattern.

A rather similar pattern develops while the convective line begins to decay, 8 cases in the pattern of parallel, 12 perpendicular, and 8 patterns combined parallel and perpendicular.

All those wind direction patterns are the patterns from the most significant wind speed that flows in each segment. A rest number that not included as parallel, perpendicular, and combined of parallel-perpendicular lies in a not significant wind flow (Figure 3-4). Based on those result, the wind speed with the perpendicular pattern is significant in the centred segment of QLCS and is relatively weaker in the flank segment either in the growing, mature, or decaying stage. It can be referred that wind direction pattern occurs at the growing stage has a significant influence on the next stage. Another result found that the wind speed and direction affect system movements. Systems with perpendicular significant wind pattern in all segments and combined parallel-perpendicular are relatively moved faster than the parallel wind patterns across the segments.

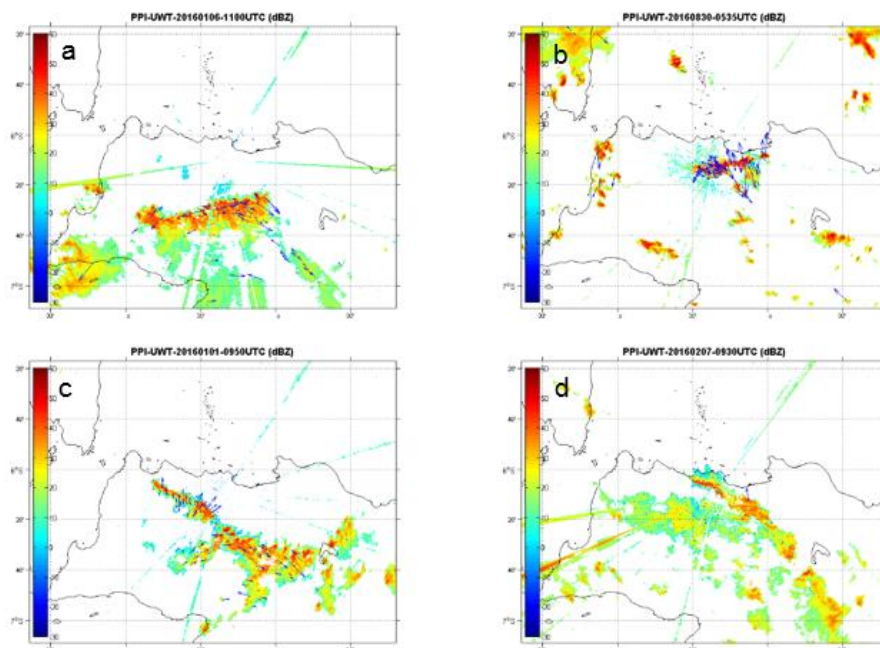


Figure 3-1: A sample of QLCS with parallel wind pattern (a), perpendicular pattern (b), combined parallel-perpendicular in centred and flank segment (c), and insignificant wind pattern along all segment (d)

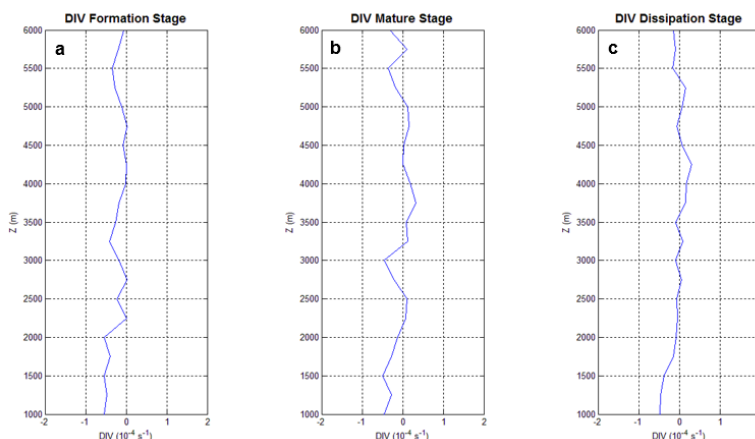


Figure 3-2: Horizontal divergence profile at 1.0-6.0 km altitude in average value for 34 cases of QLCS. (a) Growing stage, (a) Mature stage, and (c) Decaying stage (c)

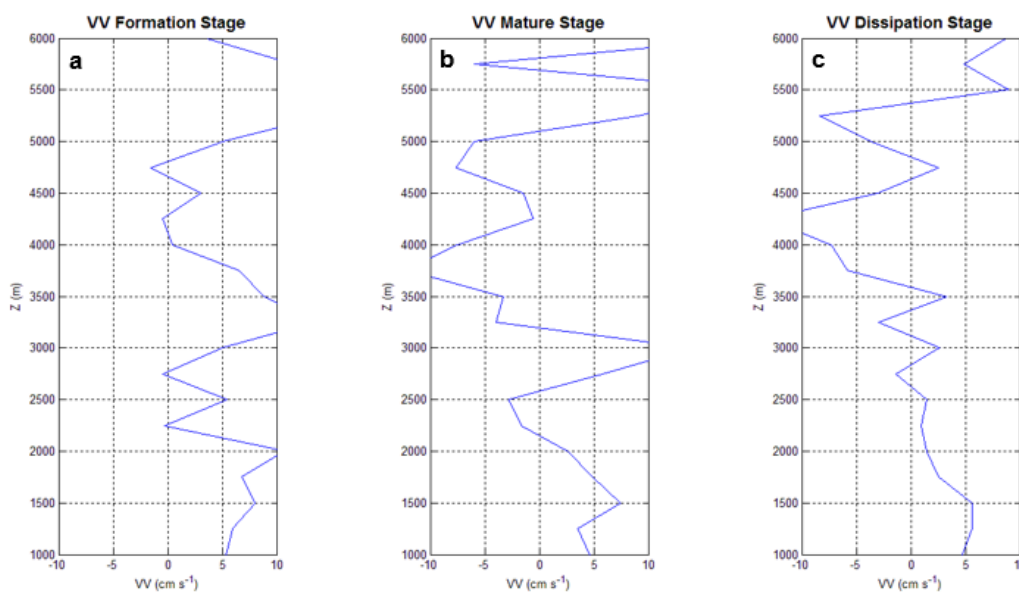


Figure 3-3: Vertical velocity profile at 1.0-6.0 km altitude in average value for 34 cases of QLCS. (a) Growing stage, (a) Mature stage, and (c) Decaying stage (c)

Based on the system movement categories by Barnes and Sieckman (1984), 5 cases were classified as fast-moving convective cloud line, 17 cases were intermediate-moving convective cloud line, and 10 cases were classified as slow-moving convective cloud line. In the case of the fast-moving convective cloud line, the wind pattern is dominated by a perpendicular pattern across segments as well as in the centred segment, whereas parallel wind patterns occur only in the flank segment and there are no cases with parallel wind patterns in all. The case of intermediate moving convective cloud line has the same wind behaviour

pattern as the fast-moving convective cloud line, but there are 3 cases with parallel wind patterns across the segment. While in the case of slow-moving convective cloud line, the wind pattern is dominated by parallel patterns across the segments and wind patterns that are not significant. But there are also 4 cases with wind patterns perpendicular across segments.

The analysis of divergence is done together with vertical velocity analysis since it has a strong relevance. Both divergence and vertical velocity are also analysed at the growing, mature, and decaying stage in a mean value of 34

cases. Data chose to be analysed lies along the level between 1.0 - 6.0 km altitudes based on the availability of data from VVP products. The average profile of divergence in the growing stage (Figure 3-2a) shows the convergent flow occurs prominently in all level, which the most significant convergent flow occurs in the 1.0 - 2.0 km layer. This convergent flow is accompanied by positive vertical velocity (updraft motion) in a layer (Figure 3-3a). This result is like the results of Gamache and Houze (1985) research which mentions that the convergent flow at GATE Squall Line occurs in the surface layer up to 700 MB. The convergent flow in the lower layers is indispensable by QLCS in forming convective cloud cells to form linear patterns.

Convergent flow is still detected in the mature stage till a height of 2.2 km, but the intensity is lower when compared to the growing phase, and in other layers, divergent pattern begins to flow (Figure 3-2b). The convergent flow in the lower layers that causing the updraft (Figure 3-3b) is still needed in the formation of new cloud cells to maintain the linear pattern.

In accordance with the theories exposed by Roger and Yau (1989) and Tjasyono (2008) concerning downdraft at the mature phase, positive divergence values are detected at 3.5 - 5.0 km altitude. This divergent flow will cause a downward current and rain begins to fall (Holton 2012).

In the average divergence profile of the decaying stage (Figure 3-2c), the condition is predominantly divergent flow from a height of 2.5 - 5.2 km, this is due to the extreme value in the data distribution of the decay phase divergence (Figure 3-4) is more dominant in the positive area. Convergent flow is still detected at the 1.0 - 2.0 km layer that leads an updraft motion (Figure 3-3c) but its intensity is lower than the growing phase and the mature phase. The whisker length in the divergence data distribution also shows a longer value in the positive area. This is consistent with convective cloud theory in the decay phase of the dominance of the decreased airflow which can be represented by positive divergent values (Roger and Yau 1989; Tjasyono 2008; Holton 2012).

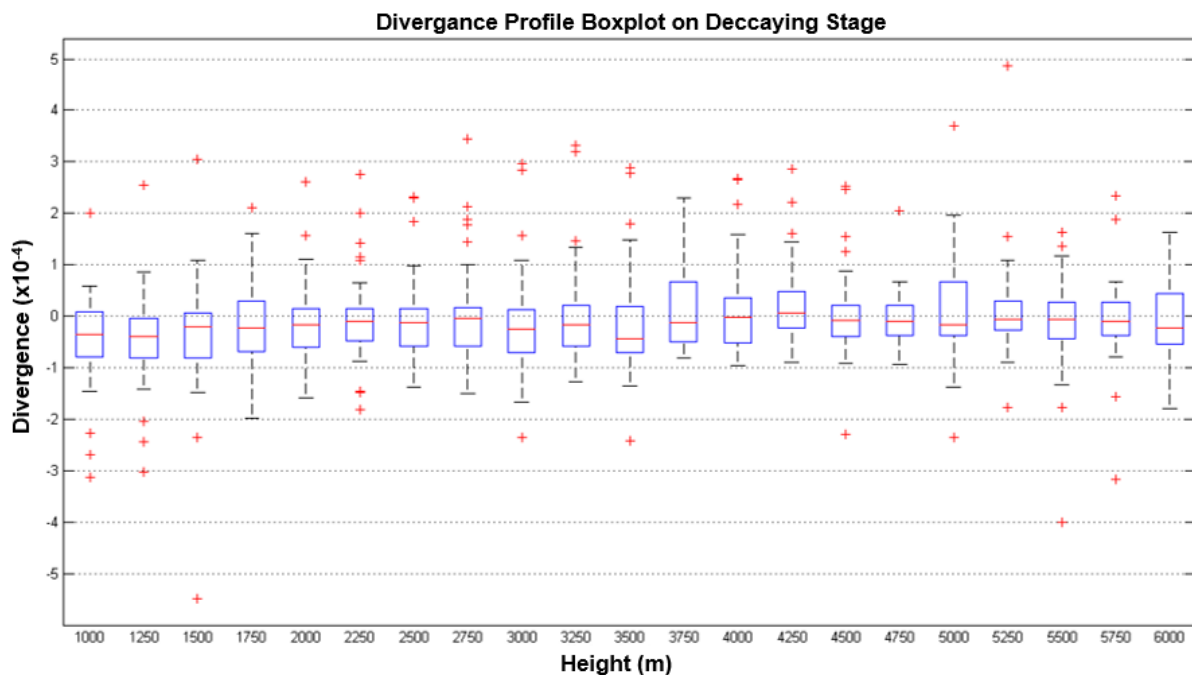


Figure 3-4: Boxplot of divergence value in each level showing data distribution. This boxplot showing a dominance value of divergent flow. An average profile showing convergent flow at 2.5-5.2 km due to some cases has really high negative value.

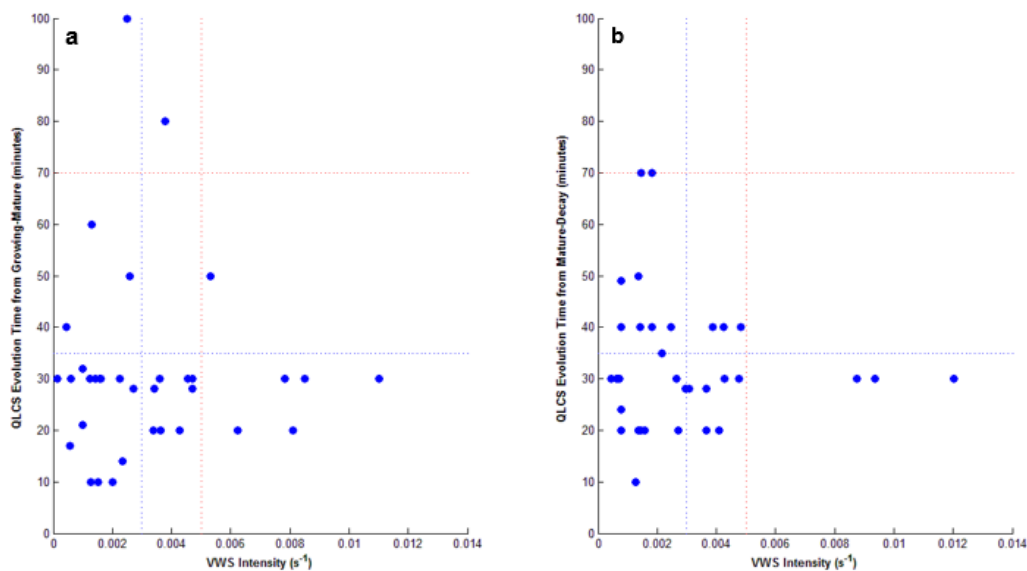


Figure 3-5: A scatter plot showing vertical wind shear value in each time interval for QLCS growing stage to mature stage (a), and QLCS mature stage to decaying stage (b).

The direction and intensity of vertical wind shear (VWS) are analysed through VVP products at an altitude of 1.0 - 3.0 km. The intensity of VWS is analysed to determine its effect on the life span of QLCS, while the direction is analysed relative to the propagation direction of QLCS to determine its tendency.

In the study of Coniglio *et al.* (2010), the intensity of VWS in the lower layers greatly affects the evolution of the system from the growing to the mature stage (when the system forms a linear pattern). Systems with strong VWS intensity will be RDMs (Rapid Developing MCSs) with the evolution of fewer than 5 hours. Conversely, systems with weak VWS intensity will become SDMs (Slowly Developing MCSs) with evolution over 7 hours. The results of that study can be analogous to the QLCS system occurring in West Java with the time of evolution is not using the threshold by Coniglio (2010) but relative to all observed events. Scatter plot to know the effect of VWS intensity on the time of evolution is shown in Figure 3-5. In the interval from growing to mature stage (Figure 3-5a), the evolution time frequency of all 34 QLCS cases that

less than 35 minutes appears dominant with 82.35% percentage, but it spreads in the weak VWS intensity category (less than  $0.003\text{ s}^{-1}$ ), moderate ( $0.003\text{ s}^{-1}$  -  $0.005\text{ s}^{-1}$ ), and strong (more than  $0.005\text{ s}^{-1}$ ). The frequency number of 41.17% were distributed at weak intensity, 23.52% in moderate intensity, and 14.70% at the strong intensity. While the evolution of more than 35 minutes only has a percentage of 17.65% with a weak intensity distribution of 11.76%, medium intensity of 2.945%, and strong intensity of 2.945%. This suggests results that are inconsistent with Coniglio's research.

In the mature stage evolution to the decay stage (Figure 3-5b), VWS intensity distribution is still concentrated in the weak category. The percentage of QLCS events with weak VWS intensity and evolution time that less than 35 minutes is 41.17%, while evolution time more than 35 minutes equal to 23.53%. In moderate intensity, 17.64% had an evolution time of fewer than 35 minutes, and 11.76% had an evolution time of more than 35 minutes. Three QLCS events (8.8%) have strong VWS intensity with evolutionary time of fewer than 35 minutes. These results also indicate that



the intensity of VWS in the mature to extinct phase also does not affect the duration of the linear pattern and is inconsistent with the results of the Lombardo and Colle research (2012) where QLCS with slowly decaying and sustaining decay patterns has a stronger VWS intensity in the lower layers.

Another aspect of VWS that can affect the QLCS system is the VWS direction. Squall lines of less than 100 km long will be propagated and move perpendicular to the average VWS direction of the lower layer (COMET 1999). In addition, in the fast-moving QLCS system, the VWS direction of the

lower layer (0-3 km) is also perpendicular to the direction of propagation (Barnes and Sieckman 1984). In this study, the direction of VWS is observed in layers of 1-3 km through a VVP product. The base height of 1 km is chosen because the data reliability level below 1 km is low for VVP products. VWS direction analysis is done at the time of growth phase, maturity phase, and dissipation phase then analysed the dominant direction of VWS relative to QLCS propagation (parallel or perpendicular), its influence on the direction of movement of QLCS, and its effect on system speed.

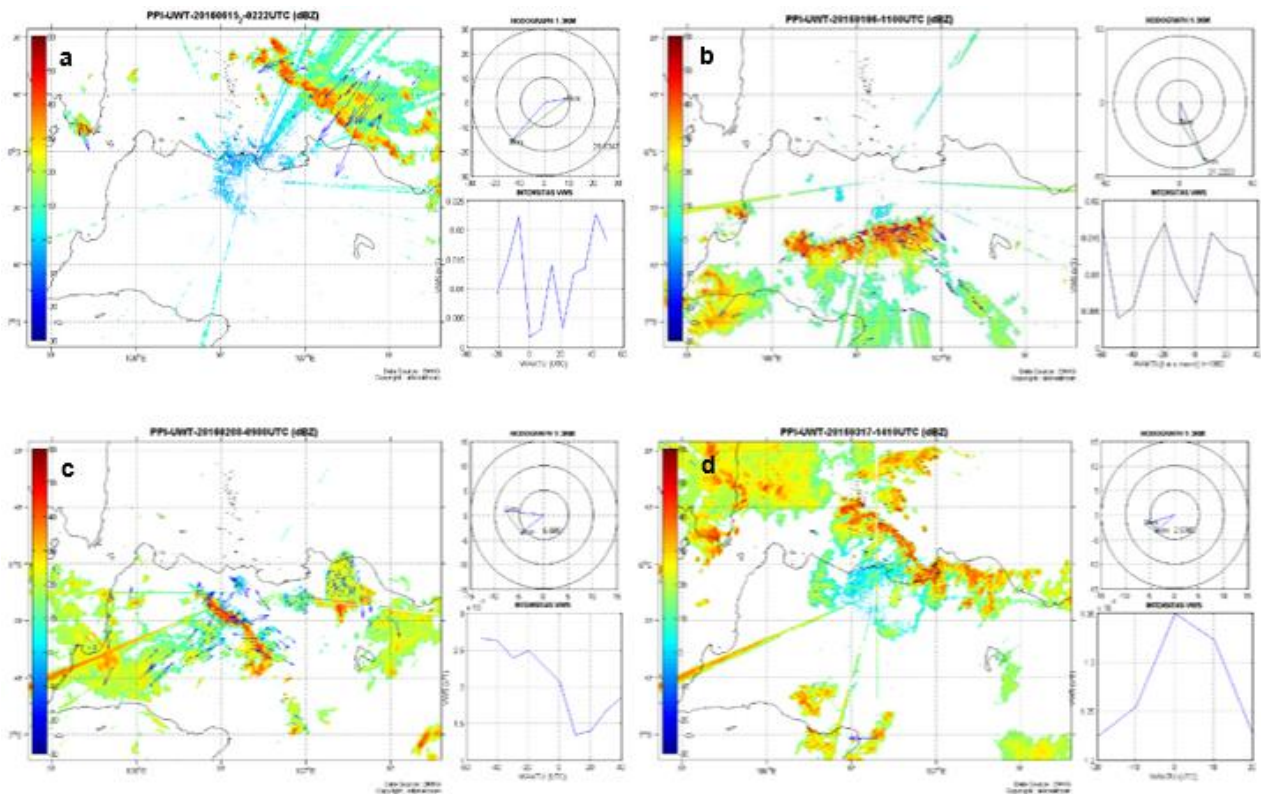


Figure 3-6: An analysis of vertical wind shear direction relative to the QLCS propagation and time series of vertical wind shear intensity. The direction of wind speed analysed by 1-3 km hodograph (upper right in each picture). The samples for the perpendicular direction of VWS relative to QLCS propagation are shown in (a) and (b), while parallel direction in (c) and (d).

Based on the comprehensive analysis, VWS direction perpendicular relative to the QLCS propagation direction (Figure 3-6a and 3-6b) occurred as many as 18 cases (52.94%) in the growing phase, 25 cases (73.52%) in the mature phase, and 21 cases (61.76%) in the decay phase. While the relative parallel direction (Figure 3-6c and 3-6d) occurred as many as 16 cases (47.06%) in the growing phase, 9 cases (26.48%) in the mature phase, and 13 cases (38.24%) in the decay phase. This shows the dominance of the VWS direction perpendicular to almost all phases.

This VWS change of direction causes precipitation in the cloud to drop in the same location as the inflow, so the system will gradually become extinct due to the absence of inrush. It is this factor that causes the VWS direction changes to be opposite to the direction of motion occurring in the mature to decaying phase.

Based on the results of the analysis of 34 QLCS events, the influence of VWS on the system movement (speed and direction) is divided into 4 categories. Category 1 is a parallel VWS direction that causes slow-moving system, while category 3 causes intermediate to fast moving. Category 2 is a parallel VWS direction that causes intermediate to fast moving system, while category 4 causes intermediate to fast moving. The percentage of each category of VWS influence on 34 QLCS events is shown in (Figure 3-7). The most dominant influence occurred in category 4 of 44%, but the variation of VWS influence in other categories is quite significant. This matter is possible because of the influence of thermodynamic factor. The movement of the squall line system (which has the same morphology as QLCS) can be affected by a combination of CAPE (Convective Available Potential Energy), CIN (Convective Inhibition), and VWS variables (COMET 1999).

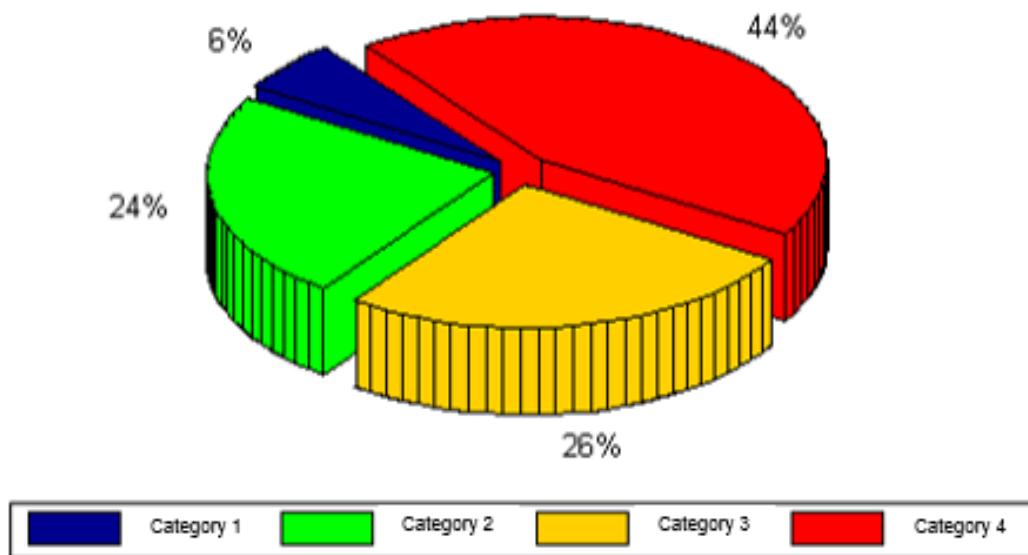


Figure 3-7: Pie chart showing the percentage of VWS direction influence to the QLCS movement divided into 4 categories. QLCS movement category based on Barnes and Sieckman (1984).

#### 4 CONCLUSION

Preliminary studies conducted to provide information that the dynamic process in QLCS that occurred in West Java is heavily influenced by vertical and horizontal wind profile. The characteristics of the wind speed and direction pattern along the centred segment are dominated by a perpendicular pattern while the flank segment is dominated by a parallel pattern of cloud propagation direction, and its pattern quite influences the direction and movement of the system. The divergence profile combined with the vertical velocity profile can represent inflow in a convective QLCS cloud, where the growing stage is marked by updraft dominance, a mature stage characterized by downdraft and updraft, as well as a decaying stage that is dominated by downdraft flow. The intensity of VWS at an altitude of 1-3 km does not affect the length of life of QLCS, whereas the direction of VWS is dominated in a direction perpendicular to the orientation of QLCS and gives a significant influence on the direction and velocity of motion.

#### ACKNOWLEDGEMENTS.

The data of this research is fully supported by BMKG Weather Radar Data Management Sub Division. The paper was improved by the helpful suggestion of Dr Aries Kristianto and Mr Eko Wardoyo. The author wishes to thank STMGK cadets who help processing data.

#### REFERENCES

- Barnes GM, Sieckman K., (1984), The Environment of Fast- and Slow-Moving Tropical Mesoscale Convective Cloud Lines, *Monthly Weather Review*, vol. 112, no. 9. pp. 1782-1794.
- Chaudhari HS, Sawaisarje GK, Ranalkar MR, Sen PN., (2010), Thunderstorms over a Tropical Indian Station, Minicoy: Role of Vertical Wind Shear, *Journal of Earth System Science*, vol. 119, Indian Academy of Sciences, India.
- Cohen AE, Coniglio MC, Corfidi SF, Corfidi SJ., (2007), Discrimination of Mesoscale Convective System Environments Using Sounding Observations. *Wea. Forecasting*, vol. 22, pp. 1045-1062.
- COMET, (1999), Mesoscale Convective System: Squall Lines and Bow Echoes, <http://www.meted.ucar.edu/convectn/mcs/>
- COMET, (2013), Principles of Convection III : Shear and Convective Storms, <http://www.meted.ucar.edu/mesoprim/shear/>
- Gamache JF, Houze RA., (1985), Further Analysis of the Composite Wind and Thermodynamic Structure of the 12 September GATE Squall Line, *Monthly Weather Review*, vol. 113, no. 8. pp. 1241-1260.
- Holton JR., (2004), Introduction to Dynamic Meteorology 4th Edition, San Diego : Elsevier
- Houze JrRA., (2004), Mesoscale Convective Systems, *Rev. Geophys*, vol. 42, pp. 1-43.
- Lericos TP, Fuelberg HE, Weisman ML, Watson AI., (2007), Numerical Simulations of The Effects of Coastlines on The Evolution Of Strong, Long-Lived Squall Lines, *Mon. Wea. Rev.*, vol. 135, pp. 1710-1731.
- Lombardo KA, Colle BA., (2010), The Spatial and Temporal Distribution of Organized Convective Structures over the Northeast and Their Ambient Conditions, *Mon. Weather Rev.*, vol. 138, no. 12, pp. 4456-4474.
- Lombardo KA, Colle BA., (2012), Ambient Conditions Associated with the Maintenance and Decay of Quasi-linear Convective Systems Crossing the Northeastern U.S. Coast, *Mon. Weather Rev.*, vol. 140, pp. 3805-3819.
- Maddox RA., (1980), Meoscale Convective Complexes, *Bulletin of the American Meteorological Society*, vol. 61, no. 11. pp. 1374-1387.



- Newman JF, Heinselman PL., (2012), Evolution of a Quasi-Linear Convective System Sampled by Phased Array Radar, *Mon. Weather Rev.*, vol. 140, pp. 3467-3480.
- Parker MD, Johnson RH., (2000), Organizational Modes of Midlatitude Mesoscale Convective Systems, *Mon. Wea. Rev.*, vol. 128, pp. 3413–3436.
- Rinehart, Ronald E., (2010), Radar for Meteorologist, Nevada : Rinehart Publication.
- Rogers RR, Yau MK., (1989), A Shourt Course in Cloud Physics. New York : Pergamon Press.
- Rotunno R., Klemp JB, Weisman ML., (1988), A Theory For Strong, Long-Lived Squall Lines, *J. Atmos. Sci.*, vol. 45, pp. 463–485.
- Thorpe AJ, Miller MJ, Moncrieff MW, (1982): Two dimensional convection in non-constant shear:A model of midlatitude squall lines. *Quart. J. Roy. Meteor. Soc.*, vol. 108, pp. 739–762.
- Tjasyono BHK., (2008a), The Characteristic of Rainfall in The Indonesia Monsson, *Proceeding of The International on Equatorial Monsoon*, Yogyakarta.
- Tjasyono BHK., (2008b), *Meteorologi Terapan*, Penerbit ITB : Bandung.
- Weisman ML, Rotunno R., (2004), A Theory for Strong Longlived Squall Lines, *J. Atmos. Sci.*, vol.61, pp. 361–382.

# PRELIMINARY DETECTION OF GEOTHERMAL MANIFESTATION POTENTIAL USING MICROWAVE SATELLITE REMOTE SENSING

Atriyon Julzarika and Udhi Catur Nugroho

Remote Sensing Applications Center

Indonesian National Institute of Aeronautics and Space (LAPAN)

E-Mail: [verbhakov@yahoo.com](mailto:verbhakov@yahoo.com) and [atriyon.julzarika@lapan.go.id](mailto:atriyon.julzarika@lapan.go.id)

Received: 29 October 2017; Revised: 4 January 2019; Approved: 4 January 2019

**Abstract.** The satellite technology has developed significantly. The sensors of remote sensing satellites are in the form of optical, Microwave, and LIDAR. These sensors can be used for energy and mineral resources applications. The example of those applications are height model and the potential of geothermal manifestation detection. This study aims to detect the potential of geothermal manifestation using remote sensing. The study area is the Northern of the Inverse Arc of Sulawesi. The method used is remote sensing approach for its preliminary detection with 4 steps as follow (a) mining land identification, (b) geological parameter extraction, (c) preparation of standardized spatial data, and (d) geothermal manifestation. Mining lands identification is using Vegetation Index Differencing method. Geological parameters include structural geology, height model, and gravity model. The integration method is used for height model. The height model integration use ALOS PALSAR data, Icesat/GLAS, SRTM, and X SAR. Structural geology use dip and strike method. Gravity model use physical geodesy approach. Preparation of standardized spatial data with re-classed and analyzed using Geographic Information System between each geological parameter, whereas physical geodesy methods are used for geothermal manifestation detection. Geothermal manifestation using physical geodesy approach in Barthelmes method. Grace and GOCE data are used for gravity model. The geothermal manifestation detected from any parameter is analyzed by using geographic information system method. The result of this study is 10 area of geothermal manifestation potential. The accuracy test of this research is 87.5 % in 1.96  $\sigma$ . This research can be done efficiently and cost-effectively in the process. The results can be used for various geological and mining applications.

Keywords: *The Northern of Inverse Arc of Sulawesi, geothermal manifestation, remote sensing, gravity model*

## 1 INTRODUCTION

Some of the survey and mapping of the potential of energy and minerals use various types of technology, one of which is remote sensing (KESDM, 1999). This remote sensing can be terrestrial, aerial, and space (satellite). The sensors that can be used in remote sensing are optics, microwaves, lasers, and sonar. Optical sensors use cameras with different types of visible, infra-red, and thermal bands.

Radar is an active microwave sensor. As the name implies, the radar

is developed as a way of using radio waves to detect the existence of an object and determine the distance (position). The process involves the transmission of short bursts or pulses of microwave power in the desired direction and recording its strength, as well as the origin of earthquakes or reflections received from objects in the field system of view. Most of the airborne sensing remote radar is performed with a system that uses an antenna mounted on the underside of the aircraft and is directed sideways.

This system is called Side Looking Radar (SLR) or Side Looking Airborne Radar (SLAR). The microwave image has a distinct advantage over the tropics, given its unclouded nature.

The microprocessor sensor has two distinct features that characterize microwave power, viewed from a remote sensing angle. In an example, microwaves can penetrate the atmosphere in varying circumstances, depending on the wavelength and reflections used and the micro-emissions from the material on the face of the earth are not directly related to the pair on the visible or thermal spectrum. The operation of this system is almost the same as the thermal radiometer (Zhou *et al.*, 2013). The theory of black body radiation is central to the conceptual understanding of passive microwave sensing, but passive microwave sensors emphasize the use of antennas rather than detection elements. Microwave signals generally consist of a number of source components that are partially transmitted, partially reflected, and partly transmitted.

Remote sensing data can be used

for preliminary surveys on potential energy and mineral resource identification applications (Youssef *et al.*, 2012). Remote sensing data will make time-efficient, cost-effective processes accelerate the analysis process in the preliminary survey (Julzarika *et al.*, 2018). In general, the process of identifying potential energy and mineral resources from remote sensing data consists of two types, namely minimal vegetation surfaces and many vegetation surfaces. On the minimal vegetation surface area, mineral resources potential can be identified with optical data, while on the area with many vegetation surfaces, mineral resources potential can be identified using microwave data, see Figure 1-1. According to EORC-JAXA (2018), remote sensing data are divided into two types of sensors, namely optical sensors and microwaves. Optical sensors consist of passive sensors (high resolution, global imaging, and spectral) and active sensors (LIDAR). The microwave sensor consists of a passive sensor (microwave radiometer) and an active sensor (SAR and Altimeter Scatterometer), see Figure 1-2.

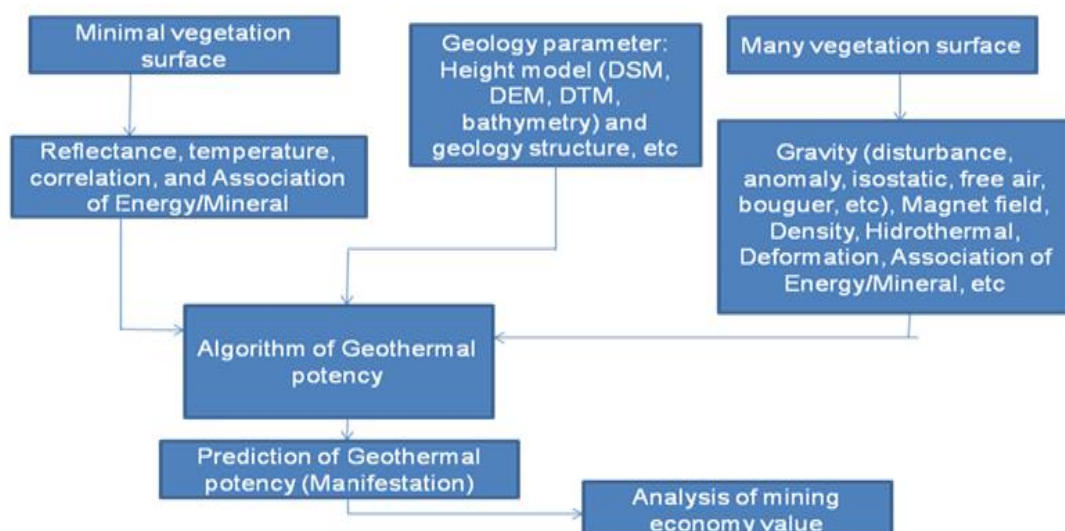


Figure 1-1: Different patterns of identification of energy mineral resources potential using remote sensing data (Julzarika and Anggraini, 2017)

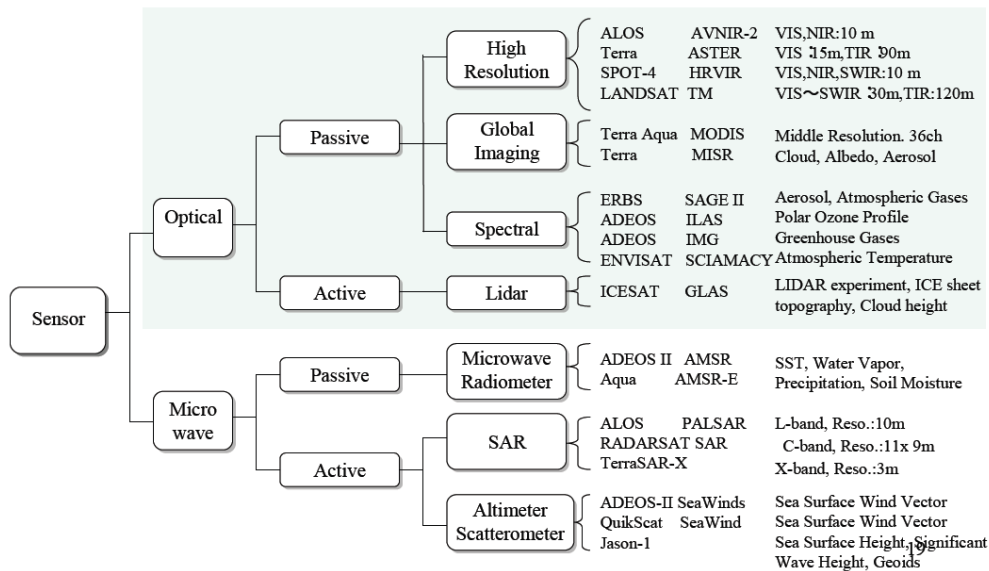


Figure 1-2: Distribution of remote sensing data types based on sensors (EORC JAXA, 2018)

Remote sensing data can also be used for height model extraction, ie. Digital Surface Model (DSM), Digital Elevation Model (DEM), and Digital Terrain Model (DTM). The method of DSM extraction commonly used is stereo. While the method of DSM extraction on microwave data is stereo SAR and Interferometry SAR (Jin *et al.*, 2014).

Geothermal is one of the potential energy that is available freely in the nature. This energy is rarely used in Indonesia. Geothermal can be used as a source of electrical energy. Remote sensing can be used for preliminary surveys to detect geothermal potential. The purpose of this paper is to detect the potential of geothermal manifestation using remote sensing.

**2 MATERIALS AND METHODOLOGY**

The research is located in the Northern of Inverse Arc of Sulawesi. This area is one of the rings of volcanoes that pass through Indonesia. This region is located near the Pacific plate, the Eurasian plate, and the Philippine Plate. The data used are data from Grace, GOCE, X SAR, SRTM, Icesat/GLAS, and field data. Height model is extracted from ALOS PALSAR,

X SAR, and Icesat/GLAS. The focus area is in yellow box, see Figure 2-1.

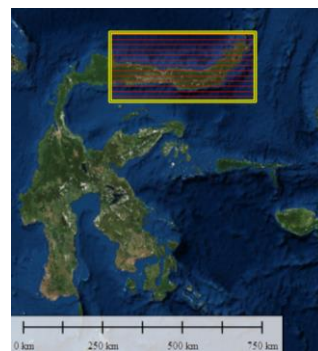


Figure 2-1: Northern of Inverse Arc Sulawesi in yellow box

The detection of this energy and mineral resources potential requires several stages: (a) mining land identification, (b) geological parameter extraction, (c) preparation of standardized spatial data with re-classed and analyzed using Geographic Information System (GIS) between each geological parameters, and (d) geothermal manifestation using physical geodesy approach in Barthelmes method, presented in Figure 2-2.

The detail stages are as follows: (a) The identification of mining land and its changes using Vegetation Index Differencing (VIDN) methods (Julzarika, 2018b). This step use Landsat data.

VIDN represents a reduction of two NDVI vegetation indexes (Nielsen, 2010; Julzarika, 2018b). VIDN values will range from -2 to 2 (Prasad & Prabhu, 2011). Negative values suggest a reduction in biomass or green vegetation and an indication of land cover change (Tjahjaningsih *et al.*, 2015). From each selected synthetic image, then a threshold is made to determine the open area of the mine (Julzarika, 2018a). The upper threshold ( $T_u$ ) and lower threshold ( $T_d$ ) values of each threshold are determined based on the sample pixel value in the ex-mining area (Liu *et al.*, 2013; Schölkopf *et al.*, 1998).

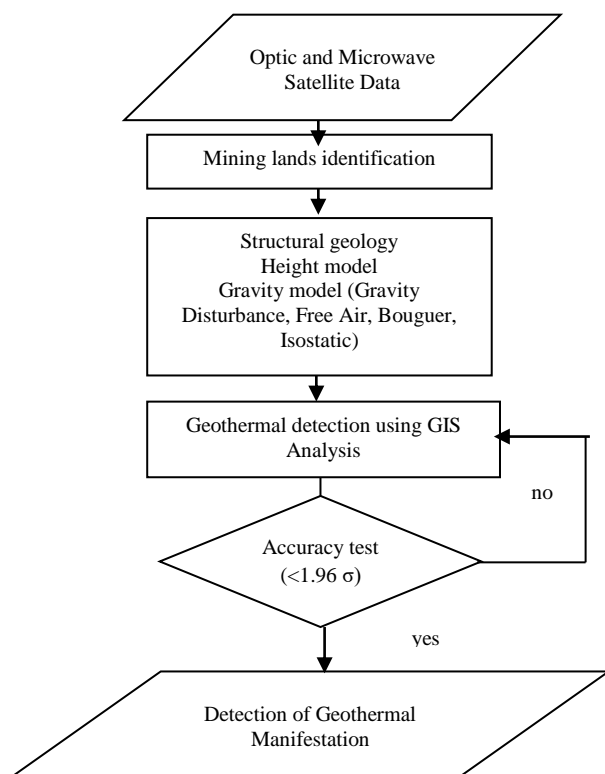


Figure 2-2: flowchart of geothermal manifestation potential

(b) Geological parameters extracted are structural geology, height model, and gravity model. The detection of these structural geology uses dip and strike methods (Rajendran *et al.*, 2013; Julzarika, *et al.*, 2013). Height model is made by using various Digital Surface Model (DSM) integration methods

(Julzarika, 2015). DSM is made from SAR data by using interferometry method.

(c) The preparation of standardized spatial data. The spatial data include raster (mining lands identification, height model, and gravity model) and vector (structural geology). Both of them must be standardized or reclassified. The raster data must have valid statistics. Calculated statistics can be used for making valid statistics.

To make standardized spatial data, the range should not overlap except at the boundary of three input raster data ranges. The range must be re-classed. Each re-classed must be set to a certain standard. The number and width of the range must be equaled for each map layers. .

For example, the mining lands re-classed, mining lands class to value 1 and non mining lands class to value 0. if ranges of height model and gravity model are specified, such as reclassifying values 0 to 100 m ; 0 to 100 miliGals (mGals) as 1 and values 100 to 300 m ; 100-200 mGals as 2, an input value less than or equal to 0 m; 0 mGals will be assigned the value 1 in the output, and an input value that is larger than 100 m, such as 100.01 m, will be assigned to 2.

After the remapping, the reclassification table has been modified. The table will not be updated if new raster are selected. The reclassification is not suitable for the new raster; a new reclassification can be reinitialized.

Structural geology is defined to identify potential reclassification results along the structural lines.

(d) Geothermal manifestation are an indication of geothermal potential. To produce the geothermal manifestation, the physical geodesy methods implemented is Barthelmes approach (Barthelmes, 2014). The gravity of the

earth is analyzed using physical geodesy approach. Barthelmes is one of the methods used in physical geodesy approach.

Gravity model include free air, gravity disturbance, Bouguer, and isostatics (Hirt *et al.*, 2012). The harmonic expansion coefficient of spherical gravitational field is the parameter for gravitational potential. Disturbing potential is obtained by reducing the gravitational potential of the reference ellipsoid (Barthelmes and Kohler, 2012). Spherical harmonic coefficients of the ellipsoid reference differ from zero to  $n = 0, 2, 4, \dots$  and  $l = 0$ , and are calculated to degrees  $n = 20$  (Bucha and Janak, 2013). The spherical harmonic coefficients of the reference ellipsoid are correctly adjusted to the values of GM and R of a given global gravity model (Barthelmes, 2013).

Gravity disturbance defined as: given the gravitational potential of topography  $Q(r, \vartheta, \lambda)$ , expressed in spherical harmonic expansion, the topographic effect is calculated by: (Barthelmes, 2014)

$$\delta g(r, \vartheta, \lambda) = -\frac{\partial T(r, \vartheta, \lambda)}{\partial r} \quad (2-1)$$

$$= \frac{GM}{r^2} \sum_{n=0}^N \sum_{l=0}^n \left(\frac{a}{r}\right)^n (n+1) (\Delta C_{nl} \cos l\lambda + \Delta S_{nl} \sin l\lambda) P_{nl}(\cos \vartheta)$$

$C_{nl}^{Topo}, S_{nl}^{Topo}$ : The coefficient of the spherical harmonic expansion model. This coefficient is from the potential gravity of the topographic mass.

The Bouguer field is defined by:

$$\delta g_{BG}(r, \vartheta, \lambda) = \delta g(r, \vartheta, \lambda) - \delta g_{topo}(r, \vartheta, \lambda) \quad (2-2)$$

For illustrations from Figure 2-3 of heat flow variations (black isolates in mW / sqm, inferred from Cataldi, 1995) include Bouguer anomalies. The highest heat current is found in the volcano, which correlates well with the positive Bouguer value and reflects the thinning crust. Low Bouguer values in the center of ground point (Po) plains do not reflect thickening of the crust, due to the low and flat topography of the center of ground point plateau, but sub-surface density variations, which can be better identified in gravity disturbance.

The Bouguer field is calculated through a global model expressed in the spherical harmonic expansion of the observed gravitational field and the gravitational field generated from topographic and bathymetric masses. (Claessens and Hirt, 2013; Hirt and Kuhn, 2012).

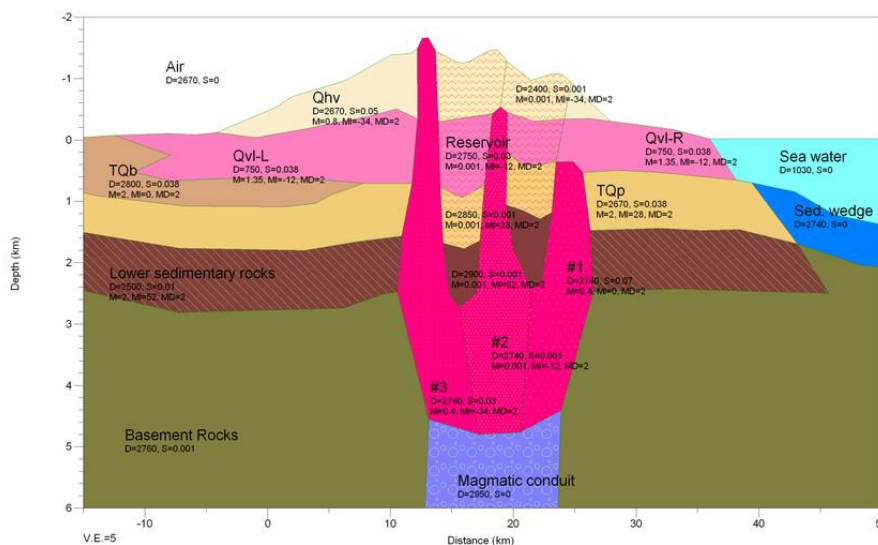


Figure 2-3: Geothermal reservoirs (Cataldi, 1995)



This geothermal manifestation on its geospatial information and geological parameters use a scale of 1: 50,000 with reference to ASPRS Accuracy Data for Digital Geospatial Data (ASPRS, 2014).

### 3 RESULT AND DISCUSSION

The results of the final research are information on geothermal manifestations in the Northern inverse arc Sulawesi. The detailed results are divided into steps 1-4. The result of the first step is the detection of mining lands using the VIDN method, see Figure 3-1.

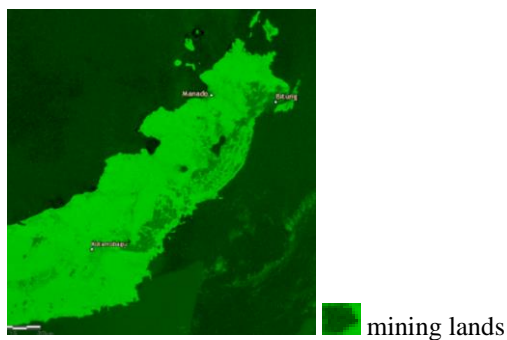


Figure 3-1: Mining lands identification

In this area, only a few mining lands are found. This is because the image used is still in medium spatial resolution. Mining land in this region is still on a small scale. This condition has no significant effect on the detection of geothermal manifestations. This

resulted in the geological parameters being more dominant in detecting geothermal manifestations. The next process is the extraction of geological parameters in step 2.

The result of the second step are Figure 3-2, 3-3, and 3-4. Earth gravity has four parameters that can be used for the extraction of energy potential and mineral resources, namely gravity disturbance, isostatic, free air, and Bouguer. Gravity disturbance is the difference between the measured gravity at a ground point and normal gravity at the same point, whereas gravity anomaly is the difference between the gravity observed in ground point, and the normal gravity in geoid, the point at which normal to the ellipsoid at ground point cuts the geoid. Isostatic can be calculated that the observed deflection can be explained if the mass of the excess mountain is matched to the same mass deficiency beneath it. Mountains are in isostatic equilibrium (isostatic equilibrium).

Free-air anomalies are calculated by correcting observations for expected variations due to spheroid and elevation above sea level. Bouguer is used to calculate the rock thickness between observation and sea level.

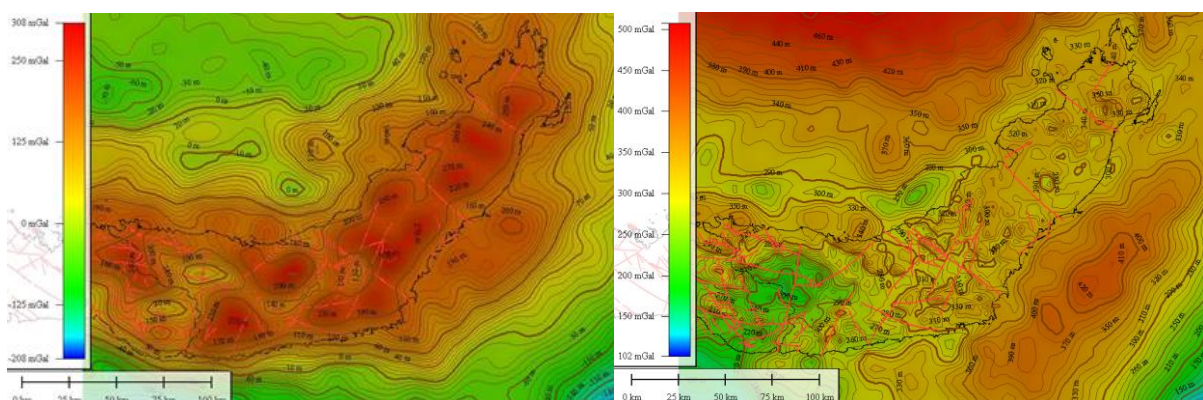


Figure 3-2: free air (left) in mgal units (yellow: high and blue values: low values) and free air are indicated by contour line, Bouguer (right)



The gravity anomalies mapped are free air and Bouguer. The free air map provides information on geological structures while the Bouguer map uses Geodesy satellite data such as GOCE with topography to show the difference in the thickness of the earth's crust. When combined these two parameters, it can be obtained a clear picture of the location of geothermal reservoirs.

The boundary between different rock types produces the permeable geometry that forms the path. An important component to exploit geothermal energy is the presence of heat in the upper layers of the earth's crust and the means to direct it to the surface.

Exploration of geothermal energy depends on access to increased surface subsurface temperatures. The crust temperature is governed by the heat fluxes of the hot coat and by the production of heat by radioactive decay in the Earth's crust. The thin crust carries a warmer coat near the surface. Therefore, increasing temperatures are found at shallow depths. A magmatic intrusion of hot gasses and hot liquid rock causes it to slowly cool down in the earth's crust. In orogens the natural radioactivity of rocks generates heat, resulting in a rise in heat and regardless of the existing coat. To bring heat to the surface, water is the transport medium. The solid rock is too compact to have the hot liquid reach the surface, so the permeable path must be found.

Heat measurements in the earth's crust are time-consuming tasks that require indirect investigation methods that can be used on a large scale, such as with remote sensing or physical geodesy from satellites. The gravitational field from Grace and GOCE satellites is a new investigation spatial tool for large-scale mapping. Bouguer maps and free water maps provide

complete information. In general, thicker crust yields a more negative Bouguer value while the thinner crust has a more positive Bouguer value. This is particularly evident in the high Bouguer values of the oceans and the negative Bouguer values for mountain ranges.

The free-air field parameter is used for geological structure mapping. This parameter can be determined its boundaries of separate rock types. The prospect of geothermal sources is very time consuming and should be focused on limited areas that have a high probability of being exploited. Gravity maps from Grace and GOCE can be integrated with hot flow values and hot flow maps. Gravity maps can be possible to become a medium of global probability classification. It is especially useful in areas where there is no local gravity and seismic data. Once a potential area has been identified, the next step is a local survey involving high resolution measurements and detailed inquiry.

Figure 3-2 illustrates the gravity values extracted from satellite data in mGals. Gravity is used to calculate the density of the energy mineral resources potential. Meanwhile, the magnetic field affects both vertical deformation and horizontal deformation occurring at locations detected in early energy mineral resources potential. Red and yellow color indicates higher value of gravity. Green color indicates medium value of gravity. Green and blue color indicates lower value of gravity. The structural geology in Figure 3-2 is symbolized by lines. The lines tip signifies the direction of the structural geology, while the line signifies the gravity disturbance field potential that occurs in the region. It uses formula (2-1).

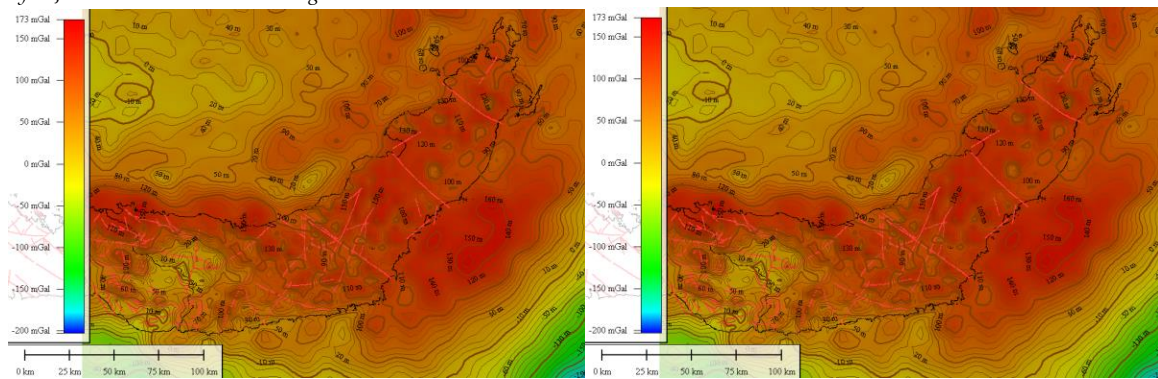


Figure 3-3: gravity disturbance (left) and isostatic (right), structural geology in red lines

Height model is required for various applications, such as for the detection of structural geology. This height model integration generates DSM so that terrain correction and height error correction is required. It aims to transform DSM into DEM and DTM as well as increase the value of its vertical accuracy. The height model integration in Figure 9 is a height integration model with a vertical accuracy of  $\pm 1.5$  m.

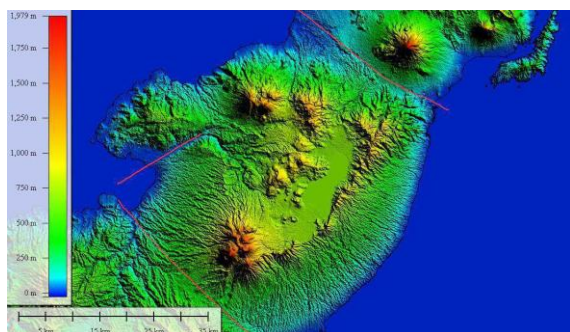


Figure 3-4: Height Model Integration (red, yellow, and green: topography with vertical accuracy 1.5 m)

The effects of topographic gravity should be calculated at the same height as gravity impairment, to the same degree and sequence and reduced. To reduce these effects, it uses the height model integration. The reduction density for topography and oceans are  $2670 \text{ kg/m}^3$  and  $1030 \text{ kg/m}^3$ , respectively. If the Bouguer grid is used for forwarding or inverting the density anomalies in the crust or mantle, care should be taken to use an 8000m

height calculation above the GRS80 ellipsoid. Overlay the value of heat flow on measurement point on the gravity disturbance map. Low gravity disturbances (low values) across the gravity point valley and correlate very well with low heat flow rates.

All parameters that have been extracted based raster and vector data are re-classed and analyzed using the GIS method. Result third step is Table 3-1.

Table 3-1: An example of re-classed data preparation for step 4 (combination of data factors)

Old Values	New Values
0 - 100 m	1
100 - 300 m	2
300 - 700 m	3
700 - 1200 m	4
1200 - 2000 m	5
NoData	Nodata

Table 3-1 is an example of a re-classed data for the preparation of standard spatial data. Each raster data includes identification of mine lands, height model, and gravity model performed by the re-classed. Then spatial analysis is carried out on geological structure data. Standardized spatial data aim to ease in spatial data analysis and use least memory of computer in processing.

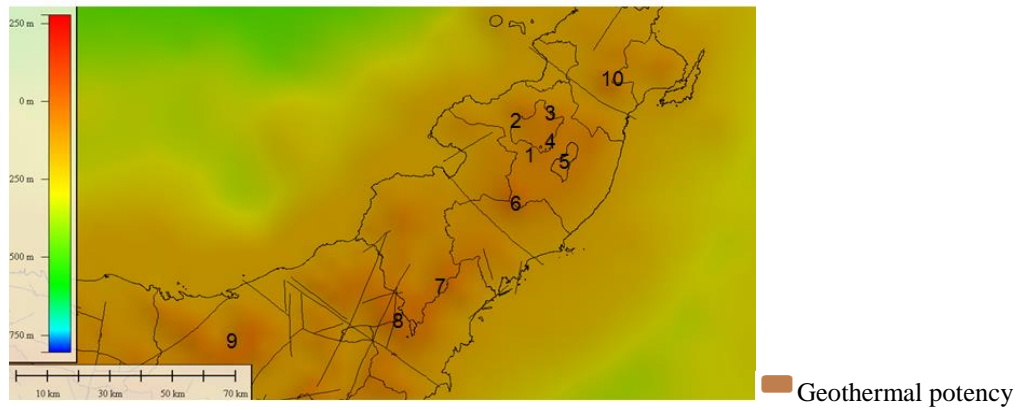










Figure 3-5: Potential of geothermal manifestation identification results using remote sensing (no 1 to 10), they are overlay into gravity disturbance imagery.

Table 3-2: Accuracy test by comparing detection results from remote sensing with the field.

ID	Photo	Result	ID	Photo	Result
ST 1		Found manifestations of hot springs	ST 6		Found manifestation of fumaroles
ST 2		Found manifestation of fumaroles	ST 7		Found manifestation of fumaroles
ST 3		Found manifestation of fumaroles	ST 8		Found manifestation of fumaroles
ST 4		Found manifestation of fumaroles	ST 9	-	Not enough time for ground validation
ST 5		Not found manifestation	ST 10	-	Not enough time for ground validation

The result of the fourth step is presented in Figure 11. Based on the results of the analysis from the result of the third step and physical geodesy method in step 4, there are 10 locations that have potential geothermal manifestations. These locations are

scattered to follow a series of volcanoes along the Sulawesi Inverse Arc. All of these locations require checking in the field whether geothermal manifestations are found or only blunders on the count of gravity anomalies. This field check uses an accuracy test.

### **Accuracy test**

The accuracy test includes 10 test points, can be seen in Table 3-2. After the field test of 10 potential points of geothermal manifestation, it resulted that there are 7 points found to be the potential manifestations of fumaroles, hot springs, and crater of the mountain. One point has not yet been found for potential geothermal manifestations. Two locations were not checked because there was not enough survey time. The accuracy of this study was 87.5% with a confidence level of  $1.96 \sigma$ . In ST 1, geothermal manifestations in the form of hot springs were found. This location is located around the state electricity company of Lahendong area. In ST 2, geothermal manifestations in the form of Fumaroles were found. The location is in the pine forest of Lahendong. The location of ST 3 is located at the top of Mount Mahawu. In the crater of the mountain, there were Fumaroles found dried up. Then on ST 4, active fumaroles were found. The location of ST 4 is at Lake Linow Lahendong. Fumaroles are spread along the west-north-east side. Lake water is also hot and contains sulfur with the appearance of green water.

The location of ST 5 is on Lake Tondano. After checking in the field, geothermal manifestations have not been found. If this location is a geothermal potential, the manifestation might be in the bottom of lake or in the lake subsurface. In ST 6, geothermal manifestations of fumaroles were found. Location ST 6 is at the Mount Soputan. The locations of ST 7 and ST 8 are on a mountain near Lake Moat, Kotamobagu. At these two locations, geothermal manifestations of fumaroles were found. The locations of ST 9 and ST 10 are around North Minahasa and Bitung. During the field survey there was not

enough time to conduct checking and validation.

## **4 CONCLUSIONS**

Remote sensing can be used to detect potential geothermal manifestations. There are four steps to detect geothermal manifestation, namely (a) mining land identification, (b) geological parameter extraction, (c) preparation of standardized spatial data, and (d) geothermal manifestation.

Detection results with remote sensing are 10 potential geothermal manifestations. After the field test, it is found that there are 7 points having the potential manifestations of fumaroles, hot springs, and crater of the mountain. There are two points are not checked due to not enough time. One point has not yet been manifested. The accuracy of this study was 87.5% with a confidence level of  $1.96 \sigma$ . This research still needs further study, namely by connecting it to geoelectric parameters, density, and geodynamics.

## **ACKNOWLEDGEMENT**

Author would like to thank LAPAN, Gadjah Mada University (UGM), PT. Pertamina Geothermal Energy (PT. PGE), DLR, USGS, Alaska University, and ESA for the success of this research in 2017. Special thanks to ESDM team of LAPAN 2017.

## **REFERENCES**

- ASPRS. (2014). ASPRS Accuracy Standard for Digital Geospatial Data. ASPRS. United States of America.
- Barthelmes, F., (2013). Definition of Functionals of the Geopotential and Their Calculation from Spherical Harmonic Models: Theory and formulas used by the calculation service of the International Centre for Global Earth Models (ICGEM); <http://icgem.gfz-potsdam.de/ICGEM/>. Scientific Technical Report STR09/02, Revised

- Edition, January 2013, Geo Forschung Zentrum Potsdam, DOI 10.2312/GFZ.b103-0902-26, URL <http://doi.org/10.2312/GFZ.b1030902-26>
- Barthelmes, F., (2014). Global Models. In: Grafarend E (ed) Encyclopedia of Geodesy, Springer International Publishing, pp 1–9, DOI 10.1007/978-3-319-02370-0 43-1, URL <http://dx.doi.org/10.1007/978-3-319-02370-0 43-1>
- Barthelmes, F., Kohler, W., (2012). International Centre for Global Earth Models (ICGEM). Journal of Geodesy, The Geodesists Handbook 2012 86(10):932–934, DOI 10.1007/s00190-0120584-1, URL <http://dx.doi.org/10.1007/s00190-012-0584-1>
- Bucha, B., & Janak, J., (2013). Code and readme of a MATLAB-based graphical user interface program for computing functionals of the geopotential. PANGAEA, <https://doi.org/10.1594/PANGAEA.808577>.
- Cataldi, R., (1995). Social acceptance: a sine qua non for geothermal development in the 21st century. Bulletin d'Hydrogiologie No 17 (1999). Centre d'Hydrogtologie, Universiti de Neuchdtel, Editions Peter Lang.
- Claessens and Hirt, (2013). Ellipsoidal topographic potential: New solutions for spectral forward gravity modeling of topography with respect to a reference ellipsoid. Journal Of Geophysical Research: Solid Earth, VOL. 118, 5991–6002, doi:10.1002/2013JB010457.
- EORC JAXA, (2018). Fundamentals of Remote Sensing. JAXA. Jepang.
- Hirt, C., & M. Kuhn, (2012). Evaluation of high-degree series expansions of the topographic potential to higher-order powers, Journal Geophysical Research (JGR) - Solid Earth, in press. doi:10.1029/2012JB009492.
- Hirt, C., M. Kuhn, W.E. Featherstone & F.Goettl, (2012). Topographic/isostatic evaluation of new-generation GOCE gravity field models, Journal of Geophysical Research - Solid Earth, B05407, doi: 10.1029/2011JB008878
- Jin, H., Mountrakis, G., & Stehman, SV, (2014). Assessing Integration of Intensity, Polarimetric Scattering, Interferometric Coherence and Spatial Texture Metrics in PALSAR-Derived Land Cover Classification. ISPRS Journal of Photogrammetry and Remote Sensing, 98, 70-84.
- Julzarika, A., (2018a). Penginderaan Jauh untuk Pendeteksian Awal Potensi Tembaga Di Sumbawa. Jurnal Riset Geologi dan Pertambangan, Vol.28, No.1, Juni 2018, 75-89. ISSN 0125-9849, e-ISSN 2354-6638 Ris.Geo.Tam Vol. 28, No.1, Juni 2018 (75-89) DOI: 10.14203/risetgeotam2018.v28.434.
- Julzarika, A., (2018b). Mining land identification in Wetar Island using remote sensing data. J. Degrade. Min. Land Manage. 6(1): 1513-1518, DOI: 10.15243/jdmlm.2018.061.1513.
- Julzarika, A., Laksono, DP, Subehi, L., Dewi, EK, Kayat, Sofiyuddin, HA, & Nugraha, MFI, (2018). Comprehensive integration system of saltwater environment on Rote Island using a multidisciplinary approach. J. Degrade. Min. Land Manage. 6(1): 1553-1567, DOI: 10.15243/jdmlm.2018.061.1553.
- Julzarika, A., & Anggraini, N., (2017). Detection of Energy and Mineral Resources Potential in Efficient and Effective using Remote Sensing. Joint Convention Geology-Geophysyc, Petroleum Engineer. Malang.
- Julzarika, A., Susanto, & Sutanto, A., (2013). Pengembangan Model Standar Pemanfaatan Data Penginderaan Jauh (Optik dan SAR) untuk Identifikasi Sumber Daya Mineral Tembaga. Laporan Penelitian Inhouse Tahun 2013. LAPAN. Jakarta.

- Julzarika, A., (2015). Integration of Height Model using SRTM C, X SAR, Aster GDEM, and ALOS Palsar. Asian Conference on Remote Sensing.
- KESDM. (1999). Kepmentamben no 1519.K/20/MPE/1999. KESDM, Jakarta.
- Liu, L., Zhou, J., Yin, F., Feng, M., & Zhang, B. (2013). The reconnaissance of mineral resources through ASTER data-based image processing, interpreting and ground inspection in the Jiafushaersu area, West Junggar, Xinjiang (China). *J. Earth Science*.
- Nielsen, A., (2010). Kernel Maximum Autocorrelation Factor and Minimum Noise Fraction Transformations. *IEEE Transactions on Image Processing* (Volume20, Issue: 3, March 2011).
- Prasad, K., & Prabhu, GK, (2011). Diag-AID: A Diagnostic Aid for Medical Image Enhancement using Colour Coding and Modified Histogram Equalisation Techniques. *International Journal of Medical Engineering and Informatics*, 3(3), 223-233.
- Rajendran, S., Nasir, S., Kusky, TM, Ghulam, A., Gabr, S., & El-Ghali, MA, (2013). Detection of Hydrothermal Mineralized Zones Associated with Listwaenites in Central Oman using ASTER Data. *Ore Geology Reviews*, 53, 470-488.
- Schölkopf, B., Smola, A., & Müller, KR, (1998). Nonlinear Component Analysis as a Kernel Eigenvalue Problem. *Neural Computation*, 10(5), 1299-1319.
- Tjahjaningsih, A., Julzarika, A., Sutanto, A., & Nugroho, UC, (2015). Pemanfaatan data penginderaan jauh untuk identifikasi tambang emas di Geumpang Aceh. Laporan penelitian inhouse 2015. LAPAN. Jakarta.
- Youssef, AM, Pradhan, B., Sabtan, AA, & El-Harbi, HM, (2012). Coupling of Remote Sensing Data Aided with Field Investigations for Geological Hazards Assessment in Jazan Area, Kingdom of Saudi Arabia. *Environmental Earth Sciences*, 65(1), 119-130.
- Zhou, J., Liu, L., Jiang, D., Zhuang, D., Mansaray LR, & Zhang B., (2013). Targeting Mineral Resources with Remote Sensing and Field Data in the Xiemisitai Area, West Junggar, Xinjiang, China. *Journal Remote Sensing*, 5(7), 3156-3171.



# THE UTILIZATION OF REMOTE SENSING DATA TO SUPPORT GREEN OPEN SPACE MAPPING IN JAKARTA, INDONESIA

Hana Listi Fitriana<sup>1</sup>, Sayidah Sulma, Nur Febrianti, Jalu Tejo Nugroho, and Nanik Suryo Haryani

Remote Sensing Application Center

Indonesian National Institute of Aeronautics and Space (LAPAN)

<sup>1</sup>E-mail: hana.listi@lapan.go.id

Received: 22 January 2018; Revised: 11 November 2018; Approved: 06 December 2018

**Abstract.** Green open space becomes critical in maintaining the balance of the environment and improving the quality of urban living for a healthy life. The use of remote sensing data for calculation of green open space has been done notably using NDVI (Normalized Difference Vegetation Index) method from Landsat 8 and SPOT data. This research aims to calculate the accuracy of the green open space classification from multispectral data of Landsat 8 and SPOT 6 using the NDVI methods. Green open space could be assessed from the value NDVI. The value of NDVI generated from Landsat 8 and SPOT 6's Red and NIR channels. The accuracy of NDVI values is then examined by comparing with Pleiades data. Pleiades data which has 50 cm panchromatic resolution and 2 m multispectral with 4 bands (B, G, R, NIR) can precisely visualize objects. So, it can be used as the reference in the calculation of the green open space based on NDVI. The results of the accuracy testing of Landsat 8 and SPOT 6 image could be used to identify the green open space by using NDVI SPOT of 6 can increase the accuracy of 5.36% from Landsat 8.

Keywords: *green open space, NDVI, Remote sensing*

## 1 INTRODUCTION

The requirement of green open space in the urban area is one of the important issues in the planning of city because green open space is closely related to the health, comfort, provision of oxygen (O<sub>2</sub>), reduction of air and water resources pollutions, reduction of carbon emissions and pollutants, to be the place where flora and fauna life, as well as in supporting the city's spatial, environmental, and sustainable development. According to Nowak (1998) Urban vegetation can directly and indirectly to affect local and regional air quality by altering the urban atmospheric environment. Along with the increasing number of urbanization and increasing population led to the increasing landuse changes which resulted in a reduced number of land cover by vegetation,

especially in urban areas, this situation causes a decrease in the quality of the urban environment (Dardak, 2016).

According to Act No. 26 of 2007 about the space management, it is stated that the proportion of green open space in the urbanized area should be at least 30% of the land area. Green open space is an area stretching/path and/or clumped, which usage is more open, in which plants grow, either grow naturally or deliberately planted. According to Chafid (2004), the green open space of the city is part of the urban space structuring that acts as a protected area. The green area of the city consists of the city landscaping, forest area green city, green city, green area of recreational sports, the green lawns. Green open space is classified based on the status of the region, not based on the form and



structure of the vegetation turns. There is relation between increasing and decreasing open green space in increasing and decreasing air quality (Effendy, 2009).

Techniques in remote sensing are applied worldwide in resources exploration and development. This major new study examines the latest advances in satellite and sensor technology, image processing and interpretation, and assesses its role in the exploration and exploitation of natural resources, particularly in the developing countries (Szekielda, 1986). To monitor land use/land cover changes in time and space remote sensing technology has been widely used since the past few decades (Javed, 2012). Remote sensing data in the form of images is capable of displaying the complete picture of the Earth's surface including associated data green open space.

Research on the utilization of remote sensing data for green open space has been widely carried out. Some of the researches which use medium resolution remote sensing data among state that Landsat 7 ETM data with a spatial resolution of 30 meters can detect green open space in DKI Jakarta. Landsat ETM 2003 can analyze land cover in the area of Bogor City with accuracy as much as 87.10% based on the overall classification and 84.81% based on kappa performance statistics data from Spatial Plan area (Haris, 2006). Landsat 8 can interpret the vast forests of Magelang city covering as much as 73.19 ha research area. By, using Landsat 8 in 2013, Febrianti and Sopian (2014) gained value of NDVI ranged from 0.2-0.73 as a cover of vegetation. From the data, it is found that the vegetation cover in Jakarta in 2013 is 9% of the entire territory.

In addition to the use of medium resolution determination of green open space, the research was also done by

using Quickbird's high resolution data. According to Hariyanto (2015) Quickbird satellite image by using object segmentation can indentify the green open space area. In the determination of the vegetation image Quickbird precision level, the interpretation of land use results obtained 91.9%, the vegetation coverage as much as 86.84%, and building density as much as 90.9% (Utami *et al.*, 2012). While the percentage of the accuracy of the classification results is quite high which can be seen from the Kappa value the accuracy for the SPOT image is 96.66% and 96.30% for the IKONOS image (Lestari, 2005). The use of ALOS AVNIR in analyzing vegetation index relates to the percentage of vegetation cover where the vegetation index values of NDVI and SAVI have the highest coefficients of determination (Sudaryanto and Melania, 2014).

One of the ways in knowing the existence of green open space is with the utilization of remotely sensed vegetation index values by using Fractional Vegetation Cover (FVC) method (Yunhao, *et al.*, 2005). Vegetation index value can provide information about the presentation of vegetation, index of plant life (Leaf Area Index), biomass plants, fAPAR (fraction of Photosynthetically Active Radiation) Occurs absorbed, the capacity of photosynthesis and estimation of absorption of carbon dioxide (CO<sub>2</sub>) (Horning, 2004; JI and Peters, 2007). Landsat-based global map, Gong *et al.* (2013) supported training data selection with MODIS Enhanced Vegetation Index (EVI) time series from 2010, aiming to improve spectral separation between cultivated bare land and natural barren lands. Vegetation index value is a value resulted from a mathematical equation. Some bands are obtained from remote sensing data. The bands are usually the red band (visible) and the NIR (Near Infra Red) band.

The utilization of satellite images with high spatial resolution satellites increases the amount of information on land cover at local to national scales (Aplin et al., 1999). The use of satellite imageries such as landsat 8 and SPOT 6 is very effective to classify areas of vegetation cover by NDVI. Landsat 8 is one of the remote sensing satellites whose data are easily obtained because Indonesia has acquired directly through LAPAN earth station in Parepare.

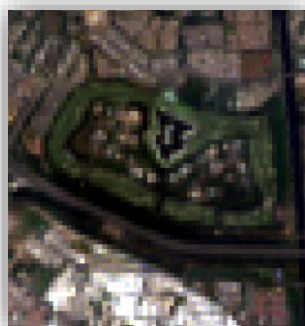
## 2 MATERIALS AND METHODOLOGY

### 2.1 Location and Data

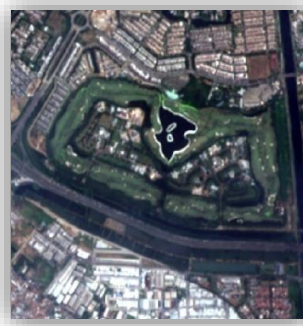
The location of the study is Jakarta at position 6°12' S and 106°48'E. Based on Statistic Indonesia (BPS) from 2009 - 2013, the area of Jakarta is 662.33 Km<sup>2</sup> including Kepulauan Seribu.

The data used in this research are the Landsat 8 data, OLI path/Row 122/64 date 25 August 2013 level 1T, SPOT 6 date 27 August 2013 and Pleiades data 12 July 2013, which have geometrically and radiometrically corrected. Landsat 8 is the multispectral data that has a wavelength of 450 µm-2300 µm. Easily obtained data will certainly make it easier for each region in calculating and evaluating green open space. SPOT 6 data is one of the high

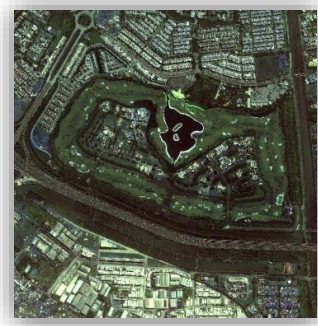
resolution satellite data that can be directly acquired from LAPAN earth station in Parepare. The research that has been done using remote sensing application data from Landsat 8 or SPOT 6 imagery needs an accuracy test by using a higher resolution image. As for the image that has a high precision is the Pleiades. The Pleiades satellite, which was made by Airbus company Defence & Space, is producing high-resolution satellite imagery. The Pleiades satellite currently entering second generation Satellite named Pleiades 1B, launched on December 2, 2012. As for the Pleiades Satellites 1A, which is the first generation of Pleiades Satellites, was launched on December 16, 2011. The Pleiades satellite satellite images data resulted in two modes which are panchromatic mode and multispectral mode. The panchromatic has a spatial resolution of 0.5 metre with 1 band, while satellite imagery in multispectral mode has a spatial resolution of 2 meters with 4 bands (VNIR – Visible Near Infra Red). As for the objective of this research is to discover the accuracy of the calculation of green open space by using Landsat 8 and 6 SPOT NDVIs, and compared to Pleiades data.



(a) Landsat 8, 25 August 2013



(b) SPOT 6, 27 August 2013



(c) Pleiades, 12 July, 2013

Figure 2-1: Comparison of spatial resolution imagery

Table 2-1: Imagery Description of Landsat 8, SPOT 6 and Pleiades

Component	Landsat 8	SPOT 6	Pleiades
Swath	185x185 Km	60 Km at nadir	20 Km at nadir
Temporal Resolution	16 day	-	-
Spatial Resolution	30 m	1.5m GSD (Panchromatic) and 6 m GSD (Multispectral)	0.5m GSD (Panchromatic) and 2m GSD (Multispectral)
Spectral Resolution	<i>Coastal/aerosol</i> (433-453 nm) Blue (450-515 nm) Green (525-600 nm) Red (630-680 nm) NIR (845-885 nm) SWIR 1 (1560-1660 nm) SWIR 2 (2100-2300 nm) Panchromatic (500-680 nm) <i>Cirrus</i> (1360-1390 nm)	Blue (444-525 nm) Green (530-590 nm) Red (625-695 nm) NIR (760-890 nm)	Panchromatic (480-830 nm) Blue (430-550 nm) Green (490-610 nm) Red (600-720 nm) NIR (750-950 nm)

Source: <http://landsat.usgs.gov>, <https://www.intelligence-airbusds.com/satellite-data/>

## 2.2 Image Data Processing

The geometric imagery often experience a shift because of the altitude of the orbit of a much smaller field of view but then the geometric distortion occurs so that the geometric correction is required. Geometric correction of the imagery is performed so that the coordinates of the image corresponds to the geographical coordinates.

Radiometric correction, which aiming to improve the value of pixels match, is supposed to consider the factors of disturbance of the atmosphere as the source of major mistakes. The effect of the atmosphere causes the reflection value of an object on the Earth's surface recorded by the sensor into its original value but not become larger due to the scattering or become smaller due to the absorption (Ji and Peters, 2007).

This research uses the vegetation index NDVI, with the following equation :

$$NDVI = \frac{\rho_{NIR} - \rho_{RED}}{\rho_{NIR} + \rho_{RED}} \quad (2-1)$$

In which:

$\rho_{NIR}$  = Reflectance Near Infrared Band

$\rho_{RED}$  = Reflectance Red Band

Landsat 8 and SPOT 6 use NDVI threshold in the classification of green open space and non green open space, while Pleiades use training sample. The green open space classification from Pleiades is classified by visually interpreting the training sample with the RGB composition of the 321. The depictions of green open space created by training samples can distinguish the vegetation and soil. Then the data were analyzed. The Pleiades was chosen based on the Area of Interest (AoI) representing the territory with green open space in the form of a park, the boundary river, the border of the road, open land as well as public and private area.

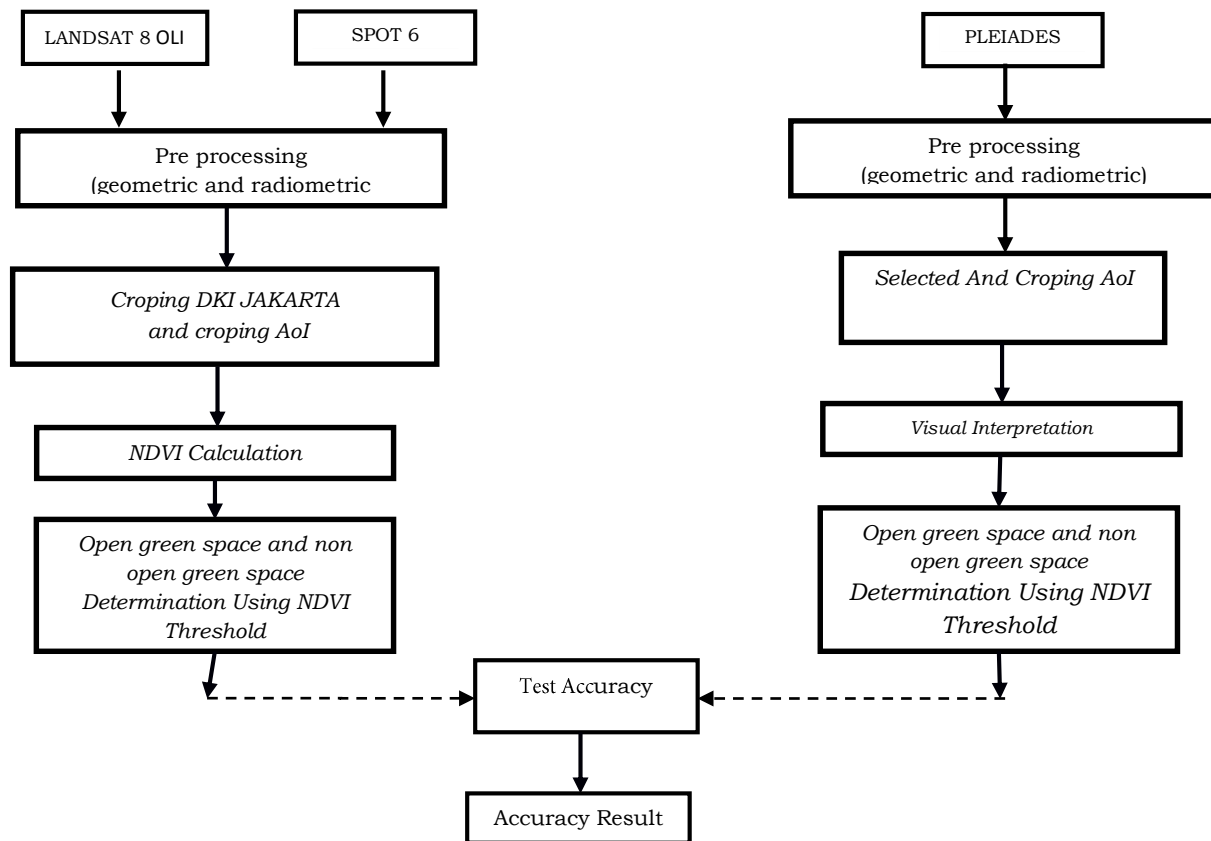


Figure 2-2: Research flow chart

### 3 RESULT AND DISCUSSION

#### 3.1 Results

In the analysis of the accuracy of the green open space calculation by Landsat 8 and SPOT 6, the Pleiades image data is used as the reference of the calculation. According to Carleer et al. (2005), the spatial resolution refinement of satellite images was attended by an increase of variability in a land cover unit. Furthermore, the spatial resolution of the sensors was improved at the expense of the spectral resolution (Herold *et al.*, 2003). Also, according to Hariyanto (2015) in a study calculating the green open space with the QuickBird data, based on the test accuracy using confusion matrix, it was determined that accuracy of interpretation results (overall accuracy) is about 90.43% and the error is about 9.57%. The panchromatics resolutions of QuickBird and the Pleiades are not much different, which are 65 cm and 50 cm. It means that Pleiades data

can be used as a reference. The three data were taken in July and August 2013. It is assumed that the conditions of the areas examined has not experienced any changes of land cover in such period of time. The classification is using visual interpretation for green open space and non green open space area. Figure 3 shows the RGB 321 Pleiades image for the sixth AOI, as well as the results of the classification of green open space and non green open space.

NDVI image of Landsat 8 and SPOT 6 for the whole area of Jakarta can be seen in Figure 2-4, in which a growing green indicates vegetation has a higher density. For the Jakarta area, the concentrations of vegetation can be seen especially in the eastern part of Jakarta.

From the results of the training samples, it is obtained that the vegetation has the NDVI value greater than 0.34 for Landsat 8 and greater than 0.33 for



SPOT 6 data. Both of the thresholds between Landsat 8 and SPOT 6 indicate the range of values that are almost identical. Such result can be caused by the conditions, the time, and the same study area, as well as the same data processing method by default in the form of value reflectans. The results of the classification of green open space and non-green open space on the 6 AOI of the Landsat 8 and SPOT 6 can be seen in Figure 2-5. In general, on Figure 2-5, it

can be seen that there is a second comparison data that shows detail. Based on Landsat 8 data, there is some areas of green open space that still cannot be detected compared to using SPOT 6 data. This can occur because of differences between the spatial resolution of the data in which the SPOT 6 has a higher spatial resolution (6 m) while Landsat 8 has a lower resolution (30 m) multispectral bands.

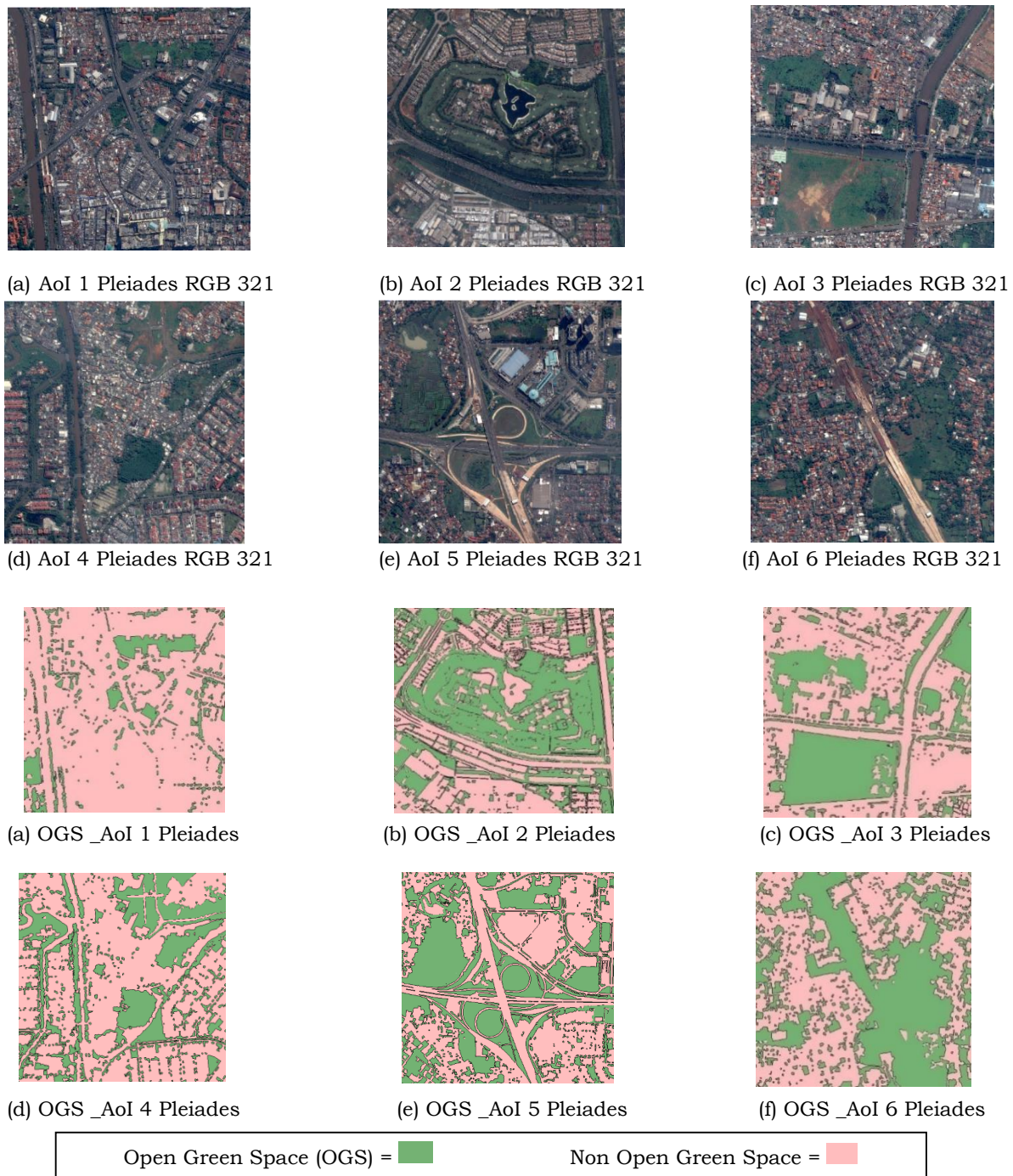


Figure 2-3: RGB 321 Pleiades Imagery and green open space classification

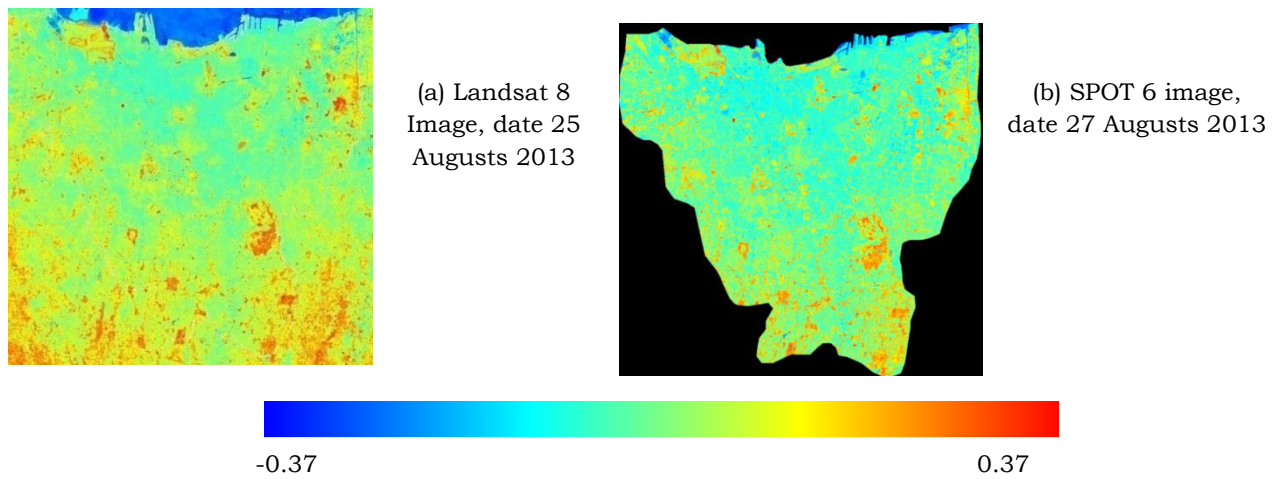
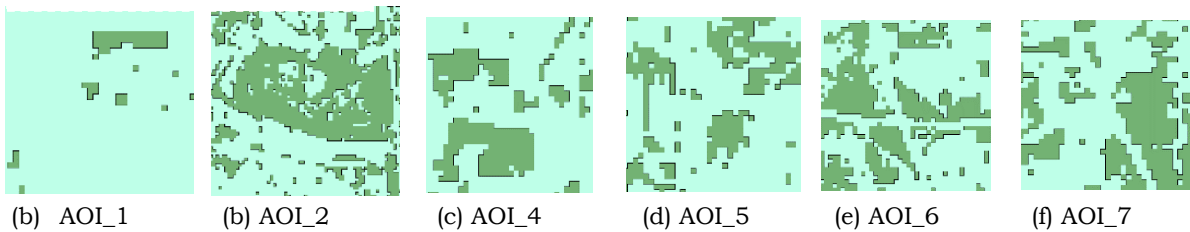


Figure 2-4: Landsat 8 and SPOT 6 NDVI

(a) Classification Landsat 8



(b) Classification SPOT 6

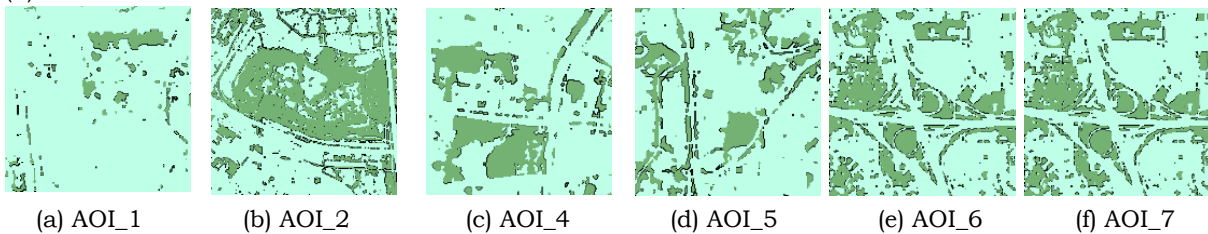


Figure 2-5: Green open space Classification based on NDVI. (a) based on Landsat 8, (b) based on SPOT 6

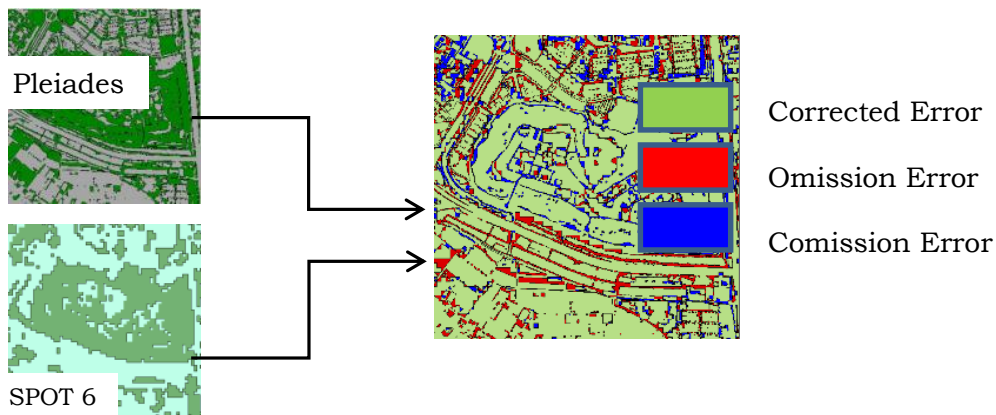


Figure 2-6: Selected Area corrected, Omission and Comission



Research on vegetation index is then used to indicate the green open space. The accuracy of the classification of green open space obtained from NDVI Landsat 8 and SPOT 6 were then tested with the Pleiades-based interpretation results.

The calculation is done using the Corrected Error, Omission Error, and Commission Error methods to overlay green open space class from NDVI of Landsat 8 or SPOT 6 with the results of the classification of green open space from the Pleiades data using the process of merging (union), later designated the area disjoint (corrected), the definitions of another class (omission) and the addition

of another class (commission) as shown in Figure 2-6.

Each AOI performed extensive calculations of corrected area, Omission and Commission area an area that can be seen in tables 2 and 3, so that the retrieved% Accuracy for Landsat 8 or SPOT 6 with the following equation:

$$\text{Accuracy(\%)} = \frac{\text{Corrected}}{\text{Corrected} + \text{Omission} + \text{Commission}} * 100\%$$

From the results of the calculation, of the difference in test results, the accuracy of Landsat 8 and SPOT 6 is only 5.36%. Meanwhile, the SPOT 6 has higher accuracy than Landsat 8.

Table 2-2: Landsat 8 accuracy test

NO.	AOI	CORR	COM	OMM	% ACCURACY
1	Aoi1	865,702	10,002	124,199	86.6
2	Aoi2	3,066,607	367,875	496,935	78.0
3	Aoi4	773,723	46,185	130,244	81.4
4	Aoi5	783,117	78,037	134,656	78.6
5	Aoi6	1,226,285	121,657	205,368	78.9
6	Aoi7	718,260	86,975	105,079	78.9
<b>% accuracy</b>					<b>80.4</b>

Source : The calculation result, 2015

Table 2-3: SPOT 6 accuracy test

NO.	AOI	CORR	COM	OMM	% ACCURACY
1	Aoi 1	890,212	5,263	104,428	89.0
2	Aoi2	3,340,361	124,742	466,262	85.0
3	Aoi4	814,807	16,268	119,077	85.8
4	Aoi5	840,743	24,541	130,526	84.4
5	Aoi6	1,319,357	30,341	222,668	83.9
6	Aoi7	788,280	28,749	93,285	86.6
<b>% accuracy</b>					<b>85.8</b>

Source : The calculation result, 2015

#### 4 CONCLUSION

Landsat 8 and SPOT 6 image could be used to identify the green open space. NDVI values obtained from Landsat 8 and SPOT 6 compare using Pleiades data. The accuracy of SPOT 6 compared better 5.36% from Landsat 8 for green open space classification by using NDVI.

#### ACKNOWLEDGEMENTS

This paper is part of research activities at remote sensing application center, Indonesian National Institute of Aeronautics and Space (LAPAN). The authors say thanks to Dr. M. Rokhis Khomarudin, the Director of Remote Sensing Application Center, Parwati Sofan, M.Si. The Head of The Environment and Disaster Mitigation Division, and Ir. Hidayat for his support on this research.

#### REFERENCES

- Aplin, P., Atkinson, P.M., Curran, P.J., (1999), Fine Spatial resolution simulated satellite sensor imagery for land cover mapping in the United Kingdom, *Remote sensing of Environment*, 68, pp. 206 - 216.
- Airbus Constellation key features, (2015), <https://www.intelligence-airbusds.com/satellite-data>. Accessed 23 Mei 2015
- Chafid, F, (2004), Peran dan Kedudukan Konservasi hutan dalam pengembangan ekowisata. Universitas Gajah Mada.
- Carleer AP., Debeir O, Wolff E., (2005,) Assessment of very high spatial resolution satellite image segmentations, *Photogrammetric Engineering and Remote Sensing*, Volume 71: 12851294.
- Dardak, AH (2006) Peran Penataan Ruang dalam Mewujudkan Kota Berkelanjutan di Indonesia. Seminar Penataan Ruang Berbasis Aspek Ekologis untuk Mewujudkan Kota Berkelanjutan, Semarang, 2 Mei 2006
- Efendy, S., (2009), *Dampak Pengurangan Ruang Terbukan Hijau (RTH) Perkotaan Terhadap Peningkatan Suhu Udara dengan Metode Penginderaan Jauh.. Journal Agromet* 23 2: 169-181.
- Febrianti, N., & Sopan, P., (2014), Ruang Terbuka Hijau Di DKI Jakarta Berdasarkan Analisis Spasial dan Spaektal Data Landsat 8. Seminar Nasional Penginderaan Jauh, Bogor, 21 April 2014
- Gong, P., Wang, J., Yu, L., Zhao, Y., Zhao, Y., Liang, L., Niu, Z., Huang, X., Fu, H., Liu, S., Li, C., Li, X., Fu, W., Liu, C., Xu, Y., Wang, X., Cheng, Q., Hu, L., Yao, W., Zhang, H., Zhu, P., Zhao, Z., Zhang, H., Zheng, Y., Ji, L., Zhang, Y., Chen, H., Yan, A., Guo, J., Yu, L., Wang, L., Liu, X., Shi, T., Zhu, M., Chen, Y., Yang, G., Tang, P., Xu, B., Giri, C., Clinton, N., Zhu, Z., Chen, J., Chen, J., (2013) Finer resolution observation and monitoring of GLC: first mapping result with Landsat TM and ETM+ data. *Int. Journal of Remote Sensing*. 34 (7), 2607-2654.
- Haris, VI., (2016), Analisis Distribusi dan Kecukupan Ruang Terbuka Hijau (RTH) Dengan Aplikasi Sistem Informasi Geografis dan Penginderaan Jauh (Studi Kasus di Kota Bogor). Skripsi Departemen Konservasi Sumberdaya Hutan dan Ekowisata Fakultas Kehutanan, Institut Teknologi Bogor.
- Herold M., Gardner M.E., Roberts D.A (2003) Spectral resolution requirements for mapping urban areas, *IEEE Transactions on Geoscience and Remote Sensing*, volume 41: 19071919.
- Horning, N., (2004), *Global Land Vegetation; An Electronic Textbook*. NASA Goddard Space Flight Center Earth Sciences Directorate Scientific and Educational Endeavors (SEE). Maryland-USA.
- Javed, A., & Imran K., (2012,) Land Use/Land Cover Change Due To Miningactivities In Singrauli Industrial Belt, Madhya Pradesh Using Remote Sensing And Gis. *Journal of Environmental Research And*

- Development Vol. 6 No. 3A, Jan-March 2012.
- Ji, L., A.J. Peters (2007) Performance Evaluation of Spectral Vegetation Indices Using a Statistical Sensitivity Function. Remote Sensing of Environmental, 106, 59-65.
- Landsat Mission, (2015), <https://www.usgs.gov/land-resources/nli/landsat>. Accessed 23 Mei 2015.
- Lestari, RAE &, I Nengah SJ., (2005), Penggunaan Teknologi Penginderaan Jauh Satelit dan SIG untuk Menentukan Luas Hutan Kota: (Studi Kasus di Kota Bogor, Jawa Barat). Jurnal Manajemen Hutan Tropika Vol. XI No. 2 : 55-69.
- Nowak, DJ., Patrick JM., Myriam I., Daniel. C., Jack CS., and Chirs JL., (1998), Modeling the Effect of Urban Vegetation on Air Pollution Modelling and Its Application XII,. Part of the NATO • Challenges of Modern Society, volume 22, pp 399-407.
- Sudaryanto & Swetika RM., (2014), Penentuan Ruang Terbuka Hijau (RTH) dengan Index Vegetasi NDVI Berbasis Citra ALOS AVNIR-2 dan Sistem Informasi Geografi di Kota Yogyakarta dan Sekitarnya. Magistra No. 89 Th. XXVI September 2014. ISSN 215-9511.
- SPOT-6 Satellite Sensor, (2015), <https://www.satimagingcorp.com/satellite-sensors/spot-6>. Accessed 23 Mei 2015.
- Szekielda, KH., (1986), Satellite remote sensing for resources development edited by Karl-Heinz Szekiolda Publish by Graham & Trotman Ltd ISBN 0 86010 805 8 Volume 1 1986 - Issue 4.
- T, Hariyanto, N.S.P, Bayu and H.H. Handayani (2015) The Use of High Resolution Satellite Image for the Classification of Green Open Space Area in Banda Aceh City, West Sumatra Indonesia. International Journal earth sciences and engineering. ISSN 0974-5904, Volume 08, No. 03 June 2015, P.P.256-258.
- Utami, SA., and Suharyadi S., Iswari NH., (2012), Penentuan Lokasi RTH Daerah Perukaan di Sebagai Kota Bekasi Menggunakan Aplikasi PJ dan SIG. Jurnal Bumi Indonesia. Vol. 1 Nomor 3.
- Yunhoa, C., S. Peijun, L. Xiaobing, C.Jin and L. Jing, (2006), A Combined Approach for Estimating Vegetation Cover in Urban/Suburban Environments From Remotely Sensed Data. Computers & Geosciences, 32, 1299-1309.

## AUTHORS INDEX

### A

Abdullah Ali 177 [15,2]  
 Ali Syahputra Nasution 113 [15,2]  
 Any Zubaidah 15 [15,1]  
 Ari Murdimanto 25 [15,1]  
 Arif Hidayat 113 [15,2]  
 Atik Nurwanda 103 [15,2]  
 Atriyon Julzarika 187 [15,2]  
 August Daulat 141 [15,2]  
 Ayom Widipaminto 113 [15,2]

### B

Bambang Sukresno 25 [15,1]

### D

Dede Dirgahayu 81 [15,1]  
 Denny Wijaya Kusuma 25 [15,1]  
 Destri Yanti Hutapea 63 [15,1]  
 Dinarika Jatisworo 25 [15,1]  
 Dipo Yudhatama 93 [15,1]  
 Djoko Triyono 157 [15,2]  
 Dony Kushardono 71 [15,1]

### E

Ety Parwati 51 [15,1]

### F

Fairus Mulia 37 [15,1]  
 Faisal Ashaari 81 [15,1]  
 Fajar Yulianto 131 [15,2]

### H

Hana Listi Fitriana 15 [15,1],  
 199 [15,2]  
 Hidayat Gunawan 113 [15,2]  
 Hitoshi Yokoyama 103 [15,2]

### I

I Nengah Surati Jaya 37 [15,1]  
 Indah Prasasti 15 [15,1]  
 157 [15,2]

### J

Jalu Tejo Nugroho 71 [15,1]  
 157,199 [15,2]  
 Jansen Sitorus 157 [15,2]

### K

Kuncoro Teguh Setiawan 51 [15,1]

### M

Made Ditha Ary Sanjaya 167 [15,2]  
 Miming Saepudin 177 [15,2]  
 Muchammad Soleh 113 [15,2]  
 Muhamad Iqbal Januadi Putra 1 [15,1]  
 Muhammad Kamal 81 [15,1]  
 Muhammad Rokhis Khomarudin 131 [15,2]  
 Mukhoriyah 93 [15,1]

### N

Nanik Suryo Haryani 199 [15,2]  
 Nobumitsu Tsunematsu 103 [15,2]  
 Nur Febrianti 199 [15,2]  
 Nurrohmat Widjajanti 167 [15,2]

### O

Octaviani Hutapea 63 [15,1]  
 Orbita Roswintiarti 51 [15,1]

### R

Riris Adriyanto 177 [15,2]  
 Rizki Hanintyo 25 [15,1]

### S

Samsul Arifin 93 [15,1]  
 Sartono Marpaung 51 [15,1]  
 Sayidah Sulma 15 [15,1]  
 131,199 [15,2]  
 Sendi Yusandi 37 [15,1]  
 Sobirin 1 [15,1]  
 Suwarsono 15 [15,1]  
 131,157 [15,2]  
 Syahrial Nur Amri 141 [15,2]

### T

T. Aris Sunantyo 167 [15,2]  
 Teguh Prayogo 51 [15,1]  
 Tsuyoshi Honjo 103 [15,2]

### U

Udhi Catur Nugroho 187 [15,2]

### W

Widodo Setiyo Pranowo 141 [15,2]

### Z

Zylshal 71 [15,1]

## KEYWORDS INDEX

<b>A</b>		Horizontal and vertical wind profile	177,178 [15,2]
Accuracy evaluation	103,105,106,107,109,111 , [15,2]		
Anak Krakatau	157,158,159,162,163,164 ,165 [15,2]	<b>I</b>	
Analysis	93,94,95,96,97,98,99,100 ,101 [15,1]	IGS	167,168,169,170,17 1,172,173,174,175, 176 [15,2]
Antenna	113,114,115,116,117,118 ,119,120,121,122,123, 124,125,126,127,128,129 [15,2]	Indonesia	178,186 [15,2]
Apatite-ilmenite	1,2,3,4,5,6,7,8,9,10,11,12 [15,1]	Inundated area	131,133,134,135,13 6,137,139 [15,2]
<b>B</b>		<b>J</b>	
Bandung basin	131,139 [15,2]	Jatigede dam	167,168,169,176 [15,2]
Biomass	37,38,39,41,42,43,44,45, 46,47,48,49 [15,1]	<b>L</b>	
Buoy data	25,26,27,28,29,30,32,33 [15,1]	Land cover	71,72,73,74,75,77, 78,79 [15,1]
<b>C</b>		Land surface temperature	103,111,112 [15,2]
The center of Tokyo	103,104 [15,2]	Landsat 8	1,2,3,4,5,11,12,13, 14 [15,1]
Control network	167,168,169,170,171,172 ,173,174,175,176 [15,2]		131,133,134,135,13 6,137,139,157,158, 159,160, 161,162,164, [15,2]
Coordinate points.	51,52,53,54,55,56,57,59, 60 [15,1]	LAPAN-A3 micro satellite	71 [15,1]
<b>D</b>		Lava flow	157,158,159,161,16 2,163,164,165 [15,2]
Data fusion	157,159,161,162,163,164 ,165 [15,2]	Least significant bit	63,64,68,69 [15,1]
Development	93,94,96,97,98,99,100, 101 [15,1]	<b>M</b>	
Direct Receiving System (DRS)	113 [15,2]	Mangrove changes	141 [15,2]
Doppler weather radar	177,178 [15,2]	Mangrove forests	37,38,40,41, 49 [15,1]
<b>F</b>		MNDWI	131,132,134,135,13 7,139 [15,2]
FCD	81,82,84,85,86,87,88,89, 91 [15,1]	Model	37,38,40,41,42,43,4 4,45,46,47,48, 49 [15,1]
Flood-prone area	131,132,134,135,138,139 [15,2]	MUR SST	25,26,27,30,31,32, 33 [15,1]
Fuzzy logic	1,2,3,4,8,11 [15,1]	<b>N</b>	
<b>G</b>		Nusa Penida MPA	141,142,143,151,15 2,153 [15,2]
Georeferencing	103,104,105,106,107,109 ,110 [15,2]	NDVI	37,40,41,42,43,44,4 5,47,48 [15,1]
Geothermal manifestation	187,189,190,191,192,194 ,195,196,197 [15,2]		141,142,144,145,14 6,147,148,149,150, 151, 154,155,199,200,20 1,202,203,205,206, 207,208 [15,2]
Gravity model	187,190,191,194,197 [15,2]	The Northern of Inverse Arc of Sulawesi	187,189 [15,2]
Green open space	199,200,201,202,203,204 ,205,206,207,208 [15,2]	<b>O</b>	
GNSS	167,168,169,170,171,172 ,173,174,175,176 [15,2]	Orthogonal	103,104,110,111 [15,2]
<b>H</b>			
Hotspot	15,16,17,18,19,20,22,23 [15,1]		
Himawari-8	15,16,18,19,20,23,24,25, 26,27,28,29,30,31, 32,34,51,52,53,54,55,56, 57,59,60 [15,1]		

Optic	113,114,115,117,121,122 ,127,128 [15,2]	Score	37,41,45 [15,1]
<b>P</b>		Sea surface temperature (SST)	25,27,29,31,33, 35 [15,1]
Pattern	93,94,96,97,99,100, 101 [15,1]	Security	81,83,84,85,87, 89 [15,1]
pixel-based classification	71,74 [15,1]	Sentinel-1 SAR	157,159,161,163, 164 [15,2]
Potential fishing zones	51,52,53,57,58,60,61 [15,1]	Single band Spatial	41,45,63,69 [15,1] 93,94,95,97,100, 101 [15,1]
<b>Q</b>		Spectral	15,16,18,19,20,21,2 3,93,94,96,97,99, 100,101 [15,1]
QLCS	177,178,179,180,182,183 ,184,185 [15,2]	Structure from motion	103,104,111,112 [15,2]
<b>R</b>		Steganography	63,64,67,68,69 [15,1]
Rare earth elements	1,2,6,13 [15,1]	<b>T</b>	
Remote Sensing	93,94,95,96,97,98,99,100 ,101 [15,1] 141,142,143,144,145,146 ,147,148,149,150, 151,152,153,154,155,187 ,188,189,190,191,192, 193,194,195,196,197,198 ,199,200,201,202, 203,204,205,206,207,208 [15,2]	Tree canopy density	81,82,83,84,86,87, 88,89,90,91 [15,1]
<b>S</b>		<b>V</b>	
S-NPP VIIRS	51,52,53,54,55,56,57,58, 59,60,61 [15,1]	Validation	25,27,28,33,34, 35 [15,1]
SAR	113,114,115,116,117,118 ,119,121,122,123, 124,126,127,128 [15,2]	Vegetation indices	81,83,85 [15,1]
Satellite	51,52,53,54,56,57, 58 [15,1]	VHRSI	113,114,115,117, 124,126,127 [15,2]
		<b>W</b>	
		Western Java Region	177 [15,2]



# INTERNATIONAL JOURNAL OF REMOTE SENSING AND EARTH SCIENCES

## Instruction for Authors

### Scope

**International Journal of Remote Sensing and Earth Sciences (IJReSES) publishes research results on remote sensing and earth sciences, with special interest in Asian region.**

### Manuscript Submission

Manuscripts submission to the IJReSES must be original with a clear definition of the objective(s), material used (data), methods applied, results, and should not have been published or offered for publication or submitted elsewhere. The manuscript should be written in English, using single line spacing on single-sided A4 size paper with 2.5 cm left and right margins, 2.5 cm upper and lower margins. The author(s) is (are) also required to submit original version of figures embedded in the paper along with their captions. All figures should be in tiff or jpeg format with high resolution (300 or 600 dpi). Submit your paper in Word to IJReSES secretariat via: [jurnal.lapan.go.id](http://jurnal.lapan.go.id).

### Manuscript Preparation

- Title should be concise and informative and not exceeding 15 words.
- The author name(s) and affiliation(s) should be written in the footnotes at the bottom of the title page.
- Abstract should contain a summary of the paper including brief introduction, the objective(s), method, and principal conclusions. Abstract should not exceed 250 words. Keywords are between 3 to 5 words and must be relevant to the subject. Do not use any sub-headings.
- Materials and methods used should clearly and concisely describe the experiment with sufficient details for independent repetition.
- Results should be presented with optimum clarity and without unnecessary detail. Results should also be presented in figures or tables but not duplicated in both format. Tables should be typed with same font size as the text and given consecutive Arabic number.
- Discussion should explain the significant findings and other important aspects of the research. Do not repeat material and methodology.
- Citation should be written in the text by the author's last name and year in one or two forms: Field *et al.* (1996) or (Field *et al.*, 1996). For references with more than two authors, list the first author plus *et al.*
- Conclusion should be concise and answer the objective(s).
- Acknowledgment, if any, should be kept at minimum (less than 40 words)
- References should be in alphabetical order. It should be written as follows:  
Field, C.B., M.J. Behrenfeld, J.T. Randerson, and P. Falkowski, 1998, Primary production of the biosphere: integrating terrestrial and oceanic components. *Science*, 281(5374):237-240.
- Acronym or uncommon abbreviations must be given in full at the first text mentioned. New abbreviation should be coined only for unwieldy names and should not be used at all unless the names occur frequently.
- Latin name and family of the species should be given besides its common name at the first mention in the manuscript, and the common name only for subsequent mentions.
- International Standard unit system (kg, m, s, etc) should be used for all manuscripts.

**International Journal of  
Remote Sensing and Earth Sciences**

December 2018

Published by:



**Indonesian National Institute of Aeronautics and Space (LAPAN)**

**Secretariat:**

**Indonesian National Institute of Aeronautics and Space (LAPAN)**

Jl. Kalisari No. 8, Pekayon, Pasar Rebo, Jakarta 13710, INDONESIA

Telp. (021) 8710065, Fax. (021) 8722733

[www.Jurnal.lapan.go.id](http://www.Jurnal.lapan.go.id)

**INTERNATIONAL JOURNAL OF  
REMOTE SENSING AND EARTH SCIENCES  
Vol. 15 No. 2 December 2018  
P-ISSN 0216-6739; E- ISSN 2549-516X  
Accreditation No. 30/E/KPT/2018**

**Contents**

Editorial Committee Preface .....	ii
Editorial Committee Members .....	iii
<b>ACCURACY EVALUATION OF STRUCTURE FROM MOTION THERMAL MOSAICING IN THE CENTER OF TOKYO</b>	
Atik Nurwanda, Tsuyoshi Honjo, Nobumitsu Tsunematsu, Hitoshi Yokoyama.....	103
<b>ANALYSIS OF ANTENNA SPECIFICATION FOR VERY HIGH RESOLUTION SATELLITE DATA ACQUISITION THROUGH DIRECT RECEIVING SYSTEM (DRS)</b>	
Muchammad Soleh, Ali Syahputra Nasution, Arif Hidayat, Hidayat Gunawan, Ayom Widipaminto.....	113
<b>OBSERVING THE INUNDATED AREA USING LANDSAT-8 MULTITEMPORAL IMAGES AND DETERMINATION OF FLOOD-PRONE AREA IN BANDUNG BASIN</b>	
Fajar Yulianto, Suwarsono, Sayidah Sulma, Muhammad Rokhis Khomarudin .....	131
<b>MANGROVE FOREST CHANGE IN NUSA PENIDA MARINE PROTECTED AREA, BALI - INDONESIA USING LANDSAT SATELLITE IMAGERY</b>	
August Daulat, Widodo Setiyo Pranowo, Syahrial Nur Amri .....	141
<b>DETECTING THE LAVA FLOW DEPOSITS FROM 2018 ANAK KRAKATAU ERUPTION USING DATA FUSION LANDSAT-8 OPTIC AND SENTINEL-1 SAR</b>	
Suwarsono, Indah Prasasti, Jalu Tejo Nugroho, Jansen Sitorus, Djoko Triyono .....	157
<b>GEOMETRIC ASPECTS EVALUATION OF GNSS CONTROL NETWORK FOR DEFORMATION MONITORING IN THE JATIGEDE DAM REGION</b>	
Made Ditha Ary Sanjaya, T. Aris Sunantyo, Nurrohmat Widjajanti .....	167
<b>PRELIMINARY STUDY OF HORIZONTAL AND VERTICAL WIND PROFILE OF QUASI- LINEAR CONVECTIVE UTILIZING WEATHER RADAR OVER WESTERN JAVA REGION, INDONESIA</b>	
Abdullah Ali, Riris Adrianto, Miming Saepudin .....	177
<b>PRELIMINARY DETECTION OF GEOTHERMAL MANIFESTATION POTENTIAL USING MICROWAVE SATELLITE REMOTE SENSING</b>	
Atriyon Julzarika, Udhi Catur Nugroho .....	187
<b>THE UTILIZATION OF REMOTE SENSING DATA TO SUPPORT GREEN OPEN SPACE MAPPING IN JAKARTA, INDONESIA</b>	
Hana Listi Fitriana, Sayidah Sulma, Nur Febrianti, Jalu Tejo Nugroho, Nanik Suryo Haryani ..	199
Instruction for Authors .....	
Index.....	

Published by:

**Indonesian National Institute of Aeronautics and Space (LAPAN)**